



THE HONG KONG
POLYTECHNIC UNIVERSITY

香港理工大學

Pao Yue-kong Library

包玉剛圖書館

Copyright Undertaking

This thesis is protected by copyright, with all rights reserved.

By reading and using the thesis, the reader understands and agrees to the following terms:

1. The reader will abide by the rules and legal ordinances governing copyright regarding the use of the thesis.
2. The reader will use the thesis for the purpose of research or private study only and not for distribution or further reproduction or any other purpose.
3. The reader agrees to indemnify and hold the University harmless from and against any loss, damage, cost, liability or expenses arising from copyright infringement or unauthorized usage.

IMPORTANT

If you have reasons to believe that any materials in this thesis are deemed not suitable to be distributed in this form, or a copyright owner having difficulty with the material being included in our database, please contact lbsys@polyu.edu.hk providing details. The Library will look into your claim and consider taking remedial action upon receipt of the written requests.

**NUMERICAL INVESTIGATION ON
REACTING SHOCK-BUBBLE INTERACTION
USING AMR METHOD**

FAN E

PhD

The Hong Kong Polytechnic University

2021

The Hong Kong Polytechnic University

Department of Mechanical Engineering

Numerical Investigation on Reacting Shock-bubble

Interaction Using AMR Method

Fan E

A thesis submitted in partial fulfillment of the requirements for the
degree of Doctor of Philosophy

June 2021

CERTIFICATE OF ORIGINALITY

I hereby declare that this thesis is my own work and that, to the best of my knowledge and belief, it reproduces no material previously published or written, nor material that has been accepted for the award of any other degree or diploma, except where due acknowledgement has been made in the text.

_____ (Signed)
FAN E

_____ (Name of student)

Dedicated to my parents

Abstract

This thesis investigates the low and high Mach number limiting cases in the reacting shock-bubble interaction (RSBI) using a novel adaptive mesh refinement (AMR) combustion solver with comprehensive H_2/O_2 chemistry. The numerical results are compared with an experiment by Haehn et al. [88]. The Richtmyer-Meshkov instability (RMI) dominates the shock-bubble interaction, and the shock focusing in the heavy bubble induces ignition. This work helps to understand the reactive RMI phenomena and to propose new safety codes for gaseous combustion concerning complex shock systems.

A new compressible combustion solver, Fire, is built on an open-source AMR framework. Particular AMR criteria suitable for combustion simulation are proposed for high efficiency. A wide range of benchmark tests is successfully surveyed for validation. By following the initial experimental setup [88] and adopting the axisymmetric assumption, this work successfully reproduces most of the flow features observed in the experiment both qualitatively and quantitatively, including the bubble morphology evolution and the corresponding chemiluminescence images.

For the low Mach number case ($M = 1.34$), the flame is deflagration, and the fuel consumption rate is nonmonotonic because of unsteady flame propagation. The deflagration waves mildly decrease the total vorticity but promote mixing by around 37% because of the thermal effects. The mixing promotion is approximately 71% related to the diffusivity and 29% related to other mechanisms after ignition. A new shock focusing mechanism is observed due to the secondary refracted shock. During shock focusing, Mach reflection occurs and transits from the bifurcated type to the single type. This transition causes two ignitions: the first occurs in the spiral hot spot entrained by the jet vortex, and the second arises from the hot spot caused by the triple point collision. After the second ignition, the newborn flame is deflagration at the beginning but is unstable and tends to transit to detonation as a consequence of the shock-flame interactions. Nevertheless, the deflagration-to-detonation transition fails, and the stable combustion mode is deflagration.

For the high Mach number case ($M = 2.83$), in contrast, the combustion wave is detonation. The detonation wave is first ignited by early-stage shock converging which is neglected by previous numerical studies, then a second ignition occurs near the equator due to regular refraction. Non-monotonic fuel consumption rate due to re-equilibrium caused by shock reflection is reported. The detonation waves significantly influence the shock system and promote mixing by around 270%. Comparing with the low Mach number case, both deflagration and detonation affect the total vorticity mildly, but their influences on the negative vorticity are opposite.

Publications Arising from the Thesis

Journal Papers:

1. **Fan, E.**, Guan, B., Wen, C. Y., & Shen, H. (2019). Numerical study on the jet formation of simple-geometry heavy gas inhomogeneities. *Physics of Fluids*, 31(2), 026103.
2. Guan, B., Wang, D., Wang, G., **Fan, E.**, & Wen, C. Y. (2020). Numerical study of the Richtmyer–Meshkov instability of a three-dimensional minimum-surface featured SF6/air interface. *Physics of Fluids*, 32(2), 024108.

Conference Paper:

1. **E Fan**, Jiaao Hao, Ben Guan and Chih-Yung Wen (2019). Numerical Study on the Ignition and Combustion Wave Propagation of the Reactive Shock-Bubble Interactions. In *2019 32nd International Symposium on Shock waves*.

Conference Presentation:

1. **E Fan**, Jiaao Hao, Ben Guan and Chih-Yung Wen (2018). Influence of Combustion on the Shock Pattern and Interface Evolution in Shock Wave-Heavy Bubble Interaction. In *2018 8th East Asia MAE workshop*.

In preparation:

Numerical investigation on reacting shock-bubble interaction at a low Mach limit (Under Review)

Extension and validation of a novel AMR frameworks ECOGEN to combustion application

Two combustion modes depending on the incident Mach number in the reactive-shock bubble interaction

Acknowledgments

After three years and nine months, I finally finish and submit my Ph.D. thesis. During these years, the PolyU campus was once taken by the riots, and the Covid-2019 changed everyday life forever. I am living in history, and at the same time, make my microhistory.

Thanks to Prof. Wen for guiding me and constantly reminding me to focus on the physical process. As a CFD researcher, sometimes, I got lost in the fancy coding and numerical results but was reluctant to improve the model to be more physically correct. Prof. Wen has an elegant physical taste in fluid mechanics and thermo-fluids. I hope that I have adopted this taste to help my research in the future.

Thanks to the other lab members! Many of them significantly impact my research, including Dr. Guan, Dr. Hao, Dr. Jiang, Dr. Shi. Thanks to Mr. Chang and Mr. Chen! You are the best roommates and friends. Also, thanks for the help and companionship from other colleagues.

Special thanks to Dr. Zhang for heartwarming talks while I was in deep depression. More importantly, thanks for introducing your roommate, Ms. Lv, to me.

Thanks to Dr. Kevin Schmidmayer and his AMR framework ECOGEN!

Thanks to my parents for supporting me in pursuing the doctoral degree. Both of them never got into the university but valued the importance of knowledge. They are open-minded and always let me make the choices. I believe they will be proud of my achievement.

Thanks to Ms. Lv for your love and trust! You keep supporting me even though I fail to fulfill my promising of submitting the thesis several times. Thanks for your companionship and trust!

Table of Contents

Abstract.....	iii
Publications Arising from the Thesis.....	iv
Acknowledgments	v
Nomenclatures	x
Abbreviations.....	xiii
List of tables.....	xiv
List of figures.....	xv
1. Introduction.....	1
1.1 Motivation.....	1
1.1.1 Inertial confinement fusion.....	1
1.1.2 Combustion	2
1.1.3 Astrophysics	2
1.2 Overview of RSBI studies	2
1.2.1 Physics of ISBI.....	2
1.2.2 Physics of RSBI.....	3
1.3 Gaps in RSBI studies	6
1.3.1 Haehn’s RSBI experiments	7
1.3.2 Relevant numerical studies.....	9
1.3.3 Gaps.....	10
1.4 Objectives	11
1.5 Outline of this thesis	11
2. Literature Review.....	12
2.1 Non-reactive RMI.....	12

2.2	Non-reactive SBI	15
2.3	Reactive RMI and ISBI.....	18
2.4	AMR methods.....	22
3.	Numerical model.....	25
3.1	Governing equations	25
3.1.1	Thermodynamic model.....	26
3.1.2	Transport properties	27
3.1.3	Chemical model.....	28
3.2	AMR methods.....	29
3.2.1	AMR data structure in ECOGEN	29
3.2.2	Advancing procedure.....	32
3.2.3	Grid Refinement Process	35
3.3	Numerical methods other than AMR.....	36
3.3.1	Inviscid fluxes	36
3.3.2	Viscous fluxes	36
3.3.3	Axisymmetric source terms.....	37
3.3.4	Chemical source term.....	40
3.4	Solving procedure.....	40
4.	Validations of Fire solver.....	42
4.1	Applications on non-reactive flows	43
4.1.1	1-D shock propagation	43
4.1.2	1-D convection-diffusion of an inert H ₂ /O ₂ front.....	45
4.1.3	ISBI: vorticity.....	46
4.1.4	Axisymmetric ISBI study.....	46
4.1.5	Mass conservativity of REC and SEC setup.....	53

4.2	Applications on reactive flows.....	55
4.2.1	0 th -dimensional cases.....	55
4.2.2	1-D detonation initiated by a reflected shock.....	56
4.2.3	1-D detonation initiated by temperature gradient profile.....	58
4.3	2-D RSBI case.....	59
5.	RSBI: grid convergence study and AMR criterion test.....	62
5.1	Grid-convergence study for $M = 1.34$ case.....	62
5.1.1	Developments of detonation in Case 134-2 and deflagration in Case 134-4.....	65
5.2	Effects of AMR criterion for $M = 2.83$ case.....	69
5.2.1	Specific AMR criterion at ignition.....	69
5.2.2	Test on grid-convergence.....	70
6.	Two combustion modes in RSBI simulation.....	73
6.1	Deflagration wave in $M = 1.34$ case.....	73
6.1.1	Numerical results.....	73
6.1.2	Effects of combustion on vorticity and mixing.....	79
6.1.3	Mach reflection transition in the ISBI.....	81
6.1.4	Ignition and failure of DDT.....	86
6.2	Detonation wave in $M = 2.83$ case.....	89
6.2.1	Numerical results.....	89
6.2.2	Ignition and early flame propagation.....	97
6.2.3	Nonmonotonic behavior of heat release.....	98
6.3	Comparison of the lower- and high- Mach limiting cases.....	102
7.	Conclusions.....	103
	References.....	105
	Appendices.....	113

A.1 Molecular properties of some species in this thesis	113
A.2 The H ₂ combustion mechanism of Ó Conaire[60]	114
A.3 Definition of instantaneous properties in RSBI study	115
A.4 The incorrect experimental data referred in Ref.[112]	116

Nomenclatures

At	Atwood number
ρ	density
h	specific enthalpy
p	pressure
γ	polytropic index
e	specific internal energy
M	Mach number
T	temperature
R	specific gas constant
Ru	universal gas constant
Λ_y^*	normalized transverse bubble diameter
τ_H	hydrodynamically characteristic time
W_i	incident shock speed
τ_c	chemically characteristic time
$[v]$	interface speed
$a(t)$	perturbation amplitude
k	perturbation wavenumber
$\delta_D(t)$	Dirac function
$a_{\text{imp}}(t)$	perturbation amplitude in impulsive model
λ	perturbation wavelength
\mathbf{U}	conservative variable vector
\mathbf{F}, \mathbf{G}	inviscid fluxes vectors
$\mathbf{F}_v, \mathbf{G}_v$	viscous fluxes vectors
\mathbf{S}_c	chemical source term vector
\mathbf{S}_a	Source term vector from the axisymmetric assumption
E	total energy per volume
$J_{i,x}, J_{i,y}$	diffusion flux component of i_{th} species
D_i	diffusion coefficient of i_{th} species
τ_{ij}	viscous stress
$\bar{\mu}$	averaged kinetic viscosity of the mixture
μ_i	kinetic viscosity of i_{th} species
q_i, q_j	the thermal conduction flux components
$\bar{\kappa}$	averaged thermal conductivity of the mixture
κ_i	thermal conductivity of i_{th} species
MW_i	molecular weight of i_{th} species
$h_i(T)$	specific enthalpy of i_{th} species at temperature T
σ_i	molecular collision diameter of i_{th} species
σ_{ij}	averaged molecular collision diameter of i_{th} and j_{th} species
$\Omega_{\mu,i}$	collision integral for viscosity for i_{th} species
$(\epsilon/k)_i$	Lennard-Jones energy parameter for i_{th} species
$\bar{\mathbf{F}}(\mathbf{U})$	inviscid flux tensor
$\bar{\mathbf{F}}_v(\mathbf{U})$	viscous flux tensor
\mathbf{S}	source term vector
$(\Delta t)_{0,dt_0}$	time step on root level in the AMR method

$(\Delta t)_p, dt_p$	time step on p_{th} level in the AMR method
cfl	CFL number
c	local sound speed / species concentration
L	maximum refinement level
ζ	refinement indicator
ζ_{split}	splitable limit for unsplit cells
ζ_{join}	mergeable limit for split cells
L_{hydro}	hydrodynamical maximum refinement level
L_{chem}	chemical maximum refinement level
T_{et}	empirical temperature threshold for ignition/flame
dx_{min}/dx_L	minimum grid size
ϕ	the properties related to diffusion terms
ϕ'	linear interpolation of the diffusive properties on the cell interface
a'	intersection of the neighboring cell centers and cell interface
\tilde{F}	inviscid flux vector in the semi-discretized form
\tilde{F}_v	viscous flux vector in the semi-discretized form
$V=(u_x, u_y)^T$	velocity vector
$n=(n_x, n_y)^T$	unit normal vector of the cell surface
$d\Omega_{rec}$	rectangular cell volume
dS_{rec}	rectangular cell surface
Ω_{rec}	computational domain in Cartesian coordinate in REC axisymmetric implementations
$\partial\Omega_{rec}$	computational boundary in Cartesian coordinate in REC axisymmetric implementations
$S_{a,rec}$	source term vector in REC axisymmetric implementations
$d\Omega_{sec}$	sector cell volume
dS_{sec}	sector cell surface
$d\hat{\Omega}_{sec}$	generalized sector cell volume
$d\hat{S}_{sec}$	generalized sector cell surface
Ω_{sec}	computational domain in cylindrical coordinate in SEC axisymmetric implementations
$\partial\Omega_{sec}$	computational boundary in cylindrical coordinate in SEC axisymmetric implementations
$S_{a,sec}$	source term vector in SEC axisymmetric implementations
dx_1	grid size of the l_{th} level
dx_0	grid size of the 0^{th} level
L_v	vortex length
L_v^*	normalized vortex length
D_0	initial bubble diameter
W	transverse bubble diameter
W^*	normalized transverse bubble diameter
$m_b^*(t)$	global mass conservativity
$m_{b,o}$	initial bubble mass
$m_b^*(t)$	initial bubble mass
$m_{b,o,theo}$	theoretical value of the initial bubble mass
t^*	non-dimensional time
$T_{max,global}$	global maximum temperature
$P_{max,global}$	global maximum pressure
$T_{max,bubble}$	maximum temperature inside the bubble

$P_{\text{max,bubble}}$	maximum pressure inside the bubble
$V_{\text{bubble}}(t)$	bubble volume
$V_{\text{flame}}(t)$	flame volume
$m_i(t)$	instant mass of i_{th} species
$\hat{m}_i(t)$	normalized mass of i_{th} species
$dm_i(t)/dt$	mass generation rate
$n_i(t)$	instant molar number of i_{th} species
$\hat{n}_i(t)$	normalized molar number of i_{th} species
$h_r(t)$	chemical heat release
$dh_r(t)/dt$	chemical heat rate
$h_{\text{full}}(t)$	High-level combustion heat when H_2/O_2 are fully consumed
Γ	Total vorticity
ω	vorticity
χ	Total mixing rate

Abbreviations

AMR	adaptive-mesh refinement
CFD	computational fluid dynamic
CRV	counter-rotating vortex
ISBI	cold shock-bubble interaction
DDT	deflagration-to-detonation transition
EOS	equation of state
FTT	fully threaded tree
FVM	finite volume method
HLLC	Harten-Lax-van Leer Contact
ICF	inertial confinement fusion
IS	Incident shock
IDT	ignition delay time
ISBI	inert shock-bubble interaction
JISC	jet injection to a supersonic cross flow
MS	Mach stem
MSB	Mach stem bulge
MUSCL	monotone upstream-centered schemes for conservation law reconstruction
NS	Navier-Stokes
ODE	ordinary differential equations
PLIF	planar laser-induced fluorescence
Pts/R	points per radius length
RfS	reflected shock
RDW	reflected detonation wave
RMI	Richtmyer-Meshkov instability
RR	regular reflection
RSBI	reactive shock-bubble interaction
RS	refracted shock
RTI	Rayleigh-Taylor instability
SAIF	shock-accelerated inhomogeneous flow
SBI	shock-bubble interaction
SFC	space-filling curve
SFI	shock-flame interaction
SFP	shock-focusing phenomenon
SL	slip line
sIS	secondary incident shock
sRS	secondary refracted shock
TBD	transverse bubble diameter
TMR	total mixing rate
TP	triple point
TS	transmitted shock
TVD	total variation diminishing
VOF	volume of fraction
WENO	weighted essentially non-oscillatory scheme

List of tables

Table 1-1. The post-shock temperature, T_2' , and pressure, p_2' and ignition delay time $\tau_{i,1Dm}$ evaluated from 1D slab geometry, and the measured ignition delay time τ_{ie} in RSBI experiments. [88].....	6
Table 1-2. The setup in Haehn's RSBI experiments and related numerical works.....	9
Table 3-1. Memory usage comparison between classical FTT AMR and dual-tree AMR methods on two types of governing equations. For the sake of clarity, only the variables in governing equations are considered.	31
Table 3-2. The granularity for both the 2D AMR and 2D uniform grid.....	34
Table 4-1 Comparison of the other solvers in ECOGEN and the Fire solver.....	42
Table 4-2. Testing cases for validation of Fire solver.....	43
Table 4-3. The clock time of all cases in Figure 4-1. totalTime: fully clock time, amrTime: clock time of AMR process, uniform: the clock time in the uniform case with $dx = dx_4$. The simulations are performed on the author's laptop.	44
Table 4-4. Thermodynamic properties of gases in the simulation	47
Table 5-1. The initial grid setups around the bubble in the grid-convergence study of the RSBI at $M = 1.34$	62
Table 5-2. The initial grid setups around the bubble in the grid-convergence study of the RSBI at $M = 2.83$	69
Table 6-1. Lengths and angles in Figure 6-4	77
Table 6-2. Combustion in low and high Mach limit of RSBI simulations.....	102
Table A-0-1. Molecular properties of some species in this thesis	113
Table A-0-2. Definition of instantaneous properties in RSBI study.....	115

List of figures

Figure 1-1. Schematic illustration of two typical shock refraction patterns in the ISBI flow field. (a) convergent ($At > 0$) and (b) divergent ($At < 0$). Incident shock propagates from the left to the right.[80].....	3
Figure 1-2. Schematic illustration of 1D shock diagram in a gas slab with $At > 0$: (a) preshock, (b) postshock.[80]	3
Figure 1-3. Schematic illustration of SBI when $At > 0$ in Ref.[88]. (a) the initial condition for a free-falling bubble with planar shock wave emerging from above, (b) the shock refraction process. The transmitted shock wave travels slower than the diffracted waves outside the bubble, and a reflected shock wave travels upstream, (c) the shock implosion region at bubble south pole, (d) just after the shock focusing when the diffracted shock waves meet a south bubble pole.....	6
Figure 1-4. Schematic of the experimental setup.[88].....	7
Figure 1-5. Composite images that show two limiting cases of combustion in RSBI. <i>white</i> signals: Mie scattering images indicating the location of bubble interface; <i>yellow</i> or <i>red</i> signals: chemiluminescence images indicating flame during the first exposure or the second. (a) $M = 1.65$, $tM_{1*}=tC_{1*}=3.6$, $tM_{2*}=tC_{2*}=6.6$, $\Delta t_{c,1*}=\Delta t_{c,2*}=3.0$. (b) $M = 2.83$, $tM_{1*}=1.7$, $tM_{2*}=3.7$, $tC_{1*}=1.3$, $tC_{2*}=2.3$, $\Delta t_{c,1*}=\Delta t_{c,2*}=0.6$. [88].....	9
Figure 1-6. The normalized TBD Λy^* as a function of normalized time t^* . The presented data is of the reacting case and non-reacting case of (a) $M = 1.65$; (b) $M = 2.83$; (c) illustration of TBD W_{TBD} .[88].....	9
Figure 2-1. Basic configuration for the RMI problem. (a) Discontinuous interface with a single-mode perturbation. Fluids 1 and 2 have different densities and adiabatic indexes. (b) Transmitted wave (T), material interface (I), reflected wave (R), and transverse wave after the acceleration. (c) The nonlinear stage: asymmetric spike and bubble structures. From Ref.[52].....	12
Figure 2-2. The numerical setup for the 2D reactive RMI study with the sinusoidal perturbed flame surface in Khokhlov et al. [37].....	18
Figure 2-3. Schematic sketch of block-based AMR and cell-based AMR methods. From Ref.[105].....	23
Figure 3-1. A schematic picture for a 2-dimensional Cartesian dual-tree AMR example in ECOGEN with 2-level grids.	29
Figure 3-2 A 2D Cartesian dual-tree AMR grid with 2-level refinement, for clarity, only the interested cell nodes and face nodes are marked.....	32

Figure 3-3. The schematic advancing procedures in the Fire solver.....	41
Figure 4-1. The density distribution of a 1D $M = 1.20$ shock wave propagating in air. (a) The results for $L = 0 - 4$ (b) Comparison of results for $L = 4$ AMR grids and uniform grid with $dx = dx_4$	44
Figure 4-2. Solution of 1-D convection-diffusion of an inert front at $400 \mu\text{s}$. Results are predicted by Fire solver (lines) or from Billet & Abgrall [59] (symbols).	45
Figure 4-3. History of circulation Γ for the interaction of an $M = 1.22$ shock wave with a cylindrical bubble of R22. The markers are digitized from the results of a ‘smoothed’ interface in Niederhaus et al. [68]. The solid lines are results predicted by the Fire solver.	46
Figure 4-4. The initial geometry of the ISBI problem. The units are mm.	47
Figure 4-5. Grid convergence tests. (a) p and (b) ρ distribution along the bubble axis with grid resolution varies from 60 to 480 Pts/R for the viscous cases at $49 \mu\text{s}$. wi: windward interface, ts: transmitted shock, li: leeward interface.	48
Figure 4-6. Density contour (upper parts) and AMR grid (lower parts) at (a) $114 \mu\text{s}$ and (b) $514 \mu\text{s}$	49
Figure 4-7. Experimental (1 st and 3 rd columns) and numerical (2 nd and 4 th columns) schlieren images for the SF_6 $M = 1.23$ ISBI results. The experimental images are from Ref. [84], and the numerical images are predicted by the Fire solver with $L = 3$	50
Figure 4-8. Experimental and numerical schlieren images of the ISBI at the initial stage for $M = 1.20$ and $D_0 = 30$ mm with the time interval of $10 \mu\text{s}$. The experimental images are from Ref. [84], and the numerical images are predicted by the Fire solver with $L = 3$	51
Figure 4-9. The dimensionless primary vortex length L_v^* as a function of t^* . The circle and gradient markers are results digitized from Ref.[84], and the triangle and square markers represent inviscid and viscous results predicted by the Fire solver with $L = 3$, respectively.	52
Figure 4-10. The dimensionless TBD value (W^*) as a function of t^* . The solid circle and reversed triangle are digitized from Ref.[84], and the triangle and square markers represent inviscid and viscous results predicted by the Fire solver with $L = 3$, respectively.	53
Figure 4-11 The global mass history of the ISBI case in 4 different numerical experiments. The lines with square and circle markers represent viscous and inviscid cases using SEC configuration, and the ones with the triangle and reversed triangle markers represent viscous and inviscid cases using REC configuration.	54
Figure 4-12. Ignition delay time with $X(\text{H}_2:\text{O}_2:\text{Ar}) = 2:1:97$ at 33 atm. Numerical predictions: the Leeds mechanism is from Ref. [46], RJ represents the reduced Jachimowski mechanism from Ref. [19], the San Diego	

mechanism is from Ref. [106], and the Ó Conaire mechanism is from Ref. [60]. The experimental data are from Petersen et al. [28]. 56

Figure 4-13 Induction time with $X(\text{H}_2:\text{O}_2:\text{N}_2)=2:1:3.76$ at 1 atm. Experimental data are from Slack [11] and Schultz and Shepherd [131]..... 56

Figure 4-14. Solution of 1-D detonation at (a) 180 μs and (b) 230 μs . Results are from results using the Fire solver (lines) or from Paolucci et al. [102]. (symbols). 57

Figure 4-15. Adaptive mesh distributions of 1-D detonation at (a) 180 μs and (b) 230 μs 58

Figure 4-16. Numerical results of the 1D detonation test. (a) Spontaneous wave (solid lines) and pressure waves (dashed lines) trajectories, (b) Velocity of the spontaneous wave. The data of blue and red lines are from Ref.[82]. 59

Figure 4-17. Detonation initiation process by the $L = 8$ cm temperature gradient in H_2/O_2 stoichiometric mixture at $p_0 = 1$ atm. (a) the result in Ref.[82], (b) the results predicted by the Fire solver $\Delta t = 2\mu\text{s}$ 59

Figure 4-18. The computational domain of ISBI and RSBI simulations. 60

Figure 4-19. Temperature contour plots of (a) the 2D cylindrical ISBI case and (b) the RSBI case with limiting $Y_{\text{Xe}} > 0.1$. In each subfigure, the upper regions depict the results in this study, and the lower regions depict the results in Ref. [108]. 61

Figure 5-1. The initial AMR grids around the bubble in the grid-convergence study of the RSBI at $M = 1.34$. (a) Case 134-1. (b) Cases 134-2 to 134-5. The root grids in the $0.5r \times 0.5r$ area near the downstream pole are set to $dx_0 = 64 \mu\text{m}$ 63

Figure 5-2. Flow fields for the $M = 1.34$ RSBI in Cases 134-1, 134-2, and 134-4 at 125 μs . In each subfigure, the upper regions depict temperature contours, and the lower regions depict pressure contours. (a) Global views of the bubble in all 3 cases and (b) detailed views of the flame and grids for only Cases 134-2 and 134-4..... 64

Figure 5-3. One-dimensional pressure and temperature distributions along the symmetry axis from Cases 134-1 to 134-5 at 125 μs 64

Figure 5-4. Flow fields for the $M = 1.34$ RSBI in Cases 134-4 at 122 μs . (a) a global view of the bubble, (b) a detailed view of the flame, and (c) schlieren contours in the dashed purple rectangle near the SFP region. 65

Figure 5-5. One-dimensional distribution of combustion properties along the bubble axis across the upstream frame fronts for RSBI Case 134-4 at 122 μs 65

Figure 5-6. 1-dimensional distribution of pressure and temperature along the bubble axis across the upstream frame fronts in RSBI Case 134-2 from 122.0 to 123.8 μs 66

Figure 5-7. One-dimensional distribution of pressure and temperature along the bubble axis across the upstream frame fronts in RSBI Case 134-4 from 122.0 to 124.9 μs	67
Figure 5-8. The nondimensional TBD values as a function of nondimensional time in this thesis and Haehn et al.'s experiment [88].....	68
Figure 5-9. The temperature and numerical schlieren contour of RSBI Case 134-2 at 151 μs . Only cells with $T > 1000$ K are shown.....	68
Figure 5-10. Ignition performance of 0 th -dimensional ignition test. Initial condition: $X(\text{H}_2:\text{O}_2:\text{Xe}) = 2:1:3.76$, (a) $T_0 = 1000$ K, $p_0 = 1$ atm. (b) $T_0 = 1200$ K, $p_0 = 100$ atm. Q : heat release rate.	69
Figure 5-11. Temperature contour plots for Case 283-1 inside the bubble. The upper parts are results from Ref. [112], while the lower parts are results in the current AMR study.....	71
Figure 5-12. Temperature contour and AMR grids for reactive Cases 283-1 and 283-2. The AMR grids are plotted at 34 μs to show the different grids.....	72
Figure 6-1. Temperature contours for the $M = 1.34$ RSBI (upper) and ISBI (lower) with limiting $Y_{\text{Xe}} > 0.1$. RS: refracted shock, KHI: Kelvin-Helmholtz instability.....	73
Figure 6-2. Vorticity contours for the $M = 1.34$ RSBI (upper) and ISBI (lower) at the later stage.	73
Figure 6-3. For the $M = 1.34$ case, the nondimensional TBD values as a function of nondimensional time in our simulation and Haehn et al.'s experiment [88].	75
Figure 6-4. Combined images of the bubble morphology and combustion signals in the $M = 1.34$ RSBI case from 205–606 μs . (a) Our numerical results: the white solid lines represent bubble interfaces, and the yellow region is the superposition of the enhanced OH^* contour. (b) The experimental result from Ref. [86]. The dash-dotted white lines represent the symmetry axis.....	76
Figure 6-5. Instantaneous properties of the $M = 1.34$ RSBI case from 0 to 854 μs : (a) peak temperature and pressure in the global flow field and inside the bubble, (b) heat release, normalized volume of the bubble, and burnt mixture, (c) mass of some reactants, and (d) rates of heat release and mass generation.....	78
Figure 6-6. Y_{H_2} contours in the $M = 1.34$ RSBI case from 400 to 700 μs	79
Figure 6-7. The history of (a) the vorticity and (b) the mixing rate in both the $M = 1.34$ ISBI and RSBI cases. .	79
Figure 6-8. Numerical schlieren and temperature contours near the downstream pole in the ISBI case from 116.8 to 121.0 μs . BI: bubble interface, IS: incident shock, RS1, RS2: refracted shocks, RfS: reflected shock, sIS: secondary incident shock, sRS: secondary refracted shock, TS1, TS2: transmitted shocks, TPs: triple points. The lower boundary in each frame coincides with the symmetry axis.	82

Figure 6-9. Sequences of numerical schlieren contours (upper regions) and Y_{N_2} contours (lower regions) during the Mach reflection transition in the ISBI case from 121.4 to 122.6 μs . MR: Mach reflection, NS: normal shock, SL: slip line, SSI: shock-shock interaction, TP: triple point, TS: transmitted shock. For the meanings of other symbols, please refer to Figure 6-8..... 83

Figure 6-10. The formations of two hot spots in the ISBI case at 121.4 and 122.1 μs . The contour in each quadrant represents the (I) vorticity, (II) temperature, (III) pressure, and (IV) Y_{N_2} . For the meanings of other symbols, please refer to Figure 6-9..... 85

Figure 6-11. Sequences of the flow fields during the first ignition in the RSBI case from 121.0 to 122.0 μs . The contour in each quadrant represents the (I) enhanced numerical schlieren, (II) temperature, (III) vorticity, and (IV) Y_{N_2} . For the meanings of symbols, please refer to Figure 6-8 and Figure 6-9. 86

Figure 6-12. Sequences of the flow fields during the second ignition and failure of DDT in the RSBI case from 122.1 to 122.9 μs . The contours in each quadrant represent the (I) numerical schlieren, (II) temperature, (III) vorticity, and (IV) pressure. For the meanings of symbols, please refer to Figure 6-8 and Figure 6-9. 88

Figure 6-13. Temperature contours for $M = 2.83$ RSBI (upper) and ISBI (lower) with limiting $Y_{X_e} > 0.35$ (for frames other than 404 μs) or $Y_{X_e} > 0.1$ (only for 404 μs)..... 90

Figure 6-14. Vorticity contours for the RSBI (upper) and ISBI (lower). MSB: Mach stem bulge, V1 and V2: vortex..... 91

Figure 6-15. The nondimensional TBD values as a function of nondimensional time for $M = 2.83$ cases. The experimental results in Ref.[88], numerical results in Ref.[112] and numerical results in the current thesis are plotted..... 92

Figure 6-16. Combined images of the bubble morphology and combustion signals in the $M = 2.83$ RSBI case from 50–60 μs . (a) Our numerical results: the white solid lines represent initial bubble interfaces, and the yellow region is the superposition of the enhanced OH^* contour. (b) The experimental result from Ref. [88]. The dash-dotted white lines represent the symmetry axis. 94

Figure 6-17. The history of (a) the vorticity and (b) the mixing rate in both the $M = 2.83$ ISBI and RSBI cases.94

Figure 6-18. Instantaneous properties of the $M = 2.83$ RSBI case from 0 to 400 μs : (a) peak temperature and pressure in the global flow field and inside the bubble, (b) heat release, normalized volume of the bubble and burnt mixture, (c) mass of some reactants, and (d) rates of heat release and mass generation. 96

Figure 6-19. The flow field of Case 283-2 at 98 μs . (a) temperature contour supposed on numerical schlieren image, only cells with $T > 1400\text{K}$ are plotted, (b) pressure contour..... 96

Figure 6-20. Instant reactive properties of the Case 283-2 from 30 to 55 μs . (a) mass of reactant, (b) mass generation rate. 98

Figure 6-21. Instant reactive properties of Case 283-2 from 60 to 120 μs : (a) mass of reactants, (b) mass generation rate. 99

Figure 6-22. The flow field of the Case 283-2 reactive case at 86, 95, 106 μs . (a) Upper parts: temperature contour supposed on numerical schlieren image, only cells with $T > 1400\text{ K}$ are plotted, lower parts: contours of $f(d\rho_{\text{H}_2\text{O}}/dt)$. (b) Upper parts: the enhanced numerical schlieren images, lower parts: the pressure contour. MS: Mach stem, RR: regular reflection..... 100

Figure 6-23. The flow properties along the bubble axis for Case 283-2 at 86, 95, and 106 μs . (a) pressure, (b) temperature, (c) $\rho_{\text{H}_2\text{O}}$ generation rate, (d) $Y_{\text{H}_2\text{O}}$. The abscissa is the distance to the initial location of the upstream bubble pole. 101

Figure A-0-1. The comprehensive H_2 combustion mechanism of Ó Conaire[60]..... 114

Figure A-0-2. The comparison of the $M = 2.83$ RSBI experimental data in two literatures. (a) the Fig.10(b) of Haehn et al.'s experimental work[88], (b) the Fig.18 of Diegelmann et al.'s numerical work[112], (c) plot of the data digitized from (a) and (b) in the same coordinates for comparison. Vertical dashed lines with the same t^* values across these three subfigures are drawn for reference. 116

1. Introduction

The Richtmyer-Meshkov instability (RMI) occurs when a shock propagates through an inhomogeneous mixture; a classical configuration for this phenomenon is a perturbed interface that separates two different fluids accelerated by a shock. The resulting flow fields involve perturbation growth [52], vorticity deposition and transportation [39], and turbulence mixing and transition [121]. This phenomenon is named after Richtmyer because of his theoretical work on the impulsively accelerated interface [5] and Meshkov, who first experimentally validated the former's work [7]. Yet earlier, Markstein [2] found the same phenomenon in a shock-flame interaction (SFI) experiment. The Kelvin-Helmholtz instability (KHI) always accompanies RMI and acts secondarily.

The classical shock-bubble interaction (SBI) considers a canonical problem that occurs when a planar shock interacts with a spherical gaseous inhomogeneity, which leads to shock refraction and reflection, vorticity generation and transportation, and turbulence [80]. Hereafter, it will be referred to as the inert shock-bubble interaction (ISBI) to differentiate it from its reactive counterpart. The reacting shock-bubble interaction (RSBI) is a type of reacting RMI phenomenon that occurs in inertial confinement fusion (ICF), scramjet engines, and supernova explosions. RMI frequently accompanies reactions, but studies of reactive RMI are limited. In 2012, Haehn et al. [88] reported a *first-of-its-kind* RSBI experiment concerning a heavy premixed combustible gas bubble. This study was of great significance, as it demonstrated for the first time that an isolated spherical mixture could be ignited by shock focusing alone. Extensive experimental results were also reported in Ref. [85, 86]. This experiment was later studied in several numerical works [107–109, 112]. However, the agreement was partially satisfactory.

In this thesis, numerical methods are used to accurately explain the coupling between the hydrodynamic and chemical processes in the RSBI experiment by Haehn et al. [88] for the first time to the author's knowledge. To efficiently predict the combustion phenomenon, an adaptive mesh refinement (AMR) compressible combustion solver, Fire, is built to perform the simulation.

1.1 Motivation

1.1.1 Inertial confinement fusion

As a viable solution to the increasing energy demand, the application of ICF motivates the fundamental study of shock-accelerated inhomogeneous flow (SAIF) problems. One of the significant problems of successful ICF technology is the detrimental mixing between the thin shell and deuterium-tritium fuel in the pellet-ablation process. This mixing shall be forbidden as it decreases the compression efficiency and suppresses the fusion process. In application, the detrimental mixing arises from microscopic inhomogeneity on the shell capsule, which acts as the density perturbation in shock tube experiments. The imperfection of the shell capsule causes convergence shocks and shock reflections driven by Rayleigh-Taylor instability (RTI) or RMI.

1.1.2 Combustion

In a non-premixed combustion system, the mixing of fuel and oxidizer can be achieved by the RMI effect, especially in the supersonic combustion scenario. In a supersonic combustor, the combustion length is too short for well mixing and complete burning, and RMI assists in both the ignition by increasing mixing and fuel consumption rate by increasing flame surface area.

In a premixed combustion system, RMI is regarded as the origin of shock-induced turbulence, which is responsible for the deflagration-to-detonation transition (DDT) [65]. The behaviors of this shock-induced turbulence do not follow the traditional Kolmogorov's narratives, and the effect of RMI is far more important than the initial laminar flame instability.

1.1.3 Astrophysics

The RMI phenomena are observed in the dynamics of interstellar medium accelerated by shocks caused by a supernova or stellar wind [25]. The formation and morphology of interstellar clouds can be well explained by the baroclinically deposited vorticity through the RMI mechanism, which leads to turbulence exchange of mass and energy between interstellar medium with inhomogeneous temperature and composition.

1.2 Overview of RSBI studies

1.2.1 Physics of ISBI

The ISBI is observed when a shock wave travels through a cylindrical or spherical gas bubble. It is caused by the difference of acoustic impedance between the bubble gas and surrounding atmosphere gas. Due to this, shock waves refract at the bubble interface, and the shape of refracted shock is convergent (or divergent) if the bubble gas is heavier (or lighter) than the ambient gas. Figure 1-1 illustrates two typical shock refraction patterns in the ISBI flow field. These two cases can be described by the Atwood number $At = (\rho_2 - \rho_1)/(\rho_1 + \rho_2)$, which is positive

for the convergent case and negative for the divergent case. Extensive studies were reported on ISBI problems, and only the convergent case is focused in this thesis.

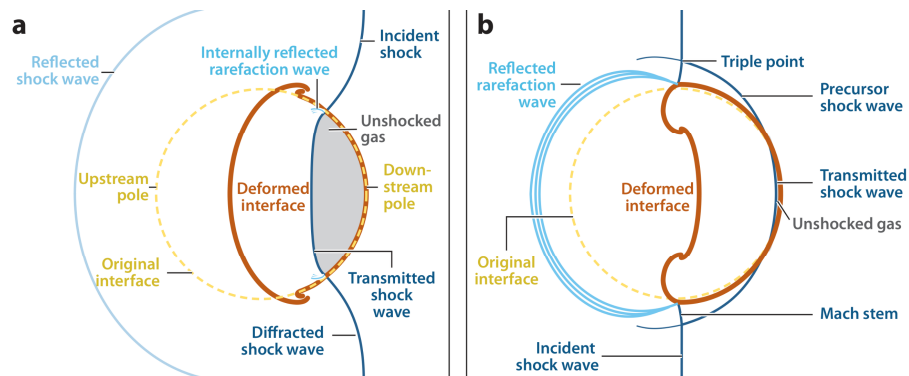


Figure 1-1. Schematic illustration of two typical shock refraction patterns in the ISBI flow field. (a) convergent ($At > 0$) and (b) divergent ($At < 0$). Incident shock propagates from the left to the right.[80]

1.2.2 Physics of RSBI

The convergent shock wave in the heavy bubble case can considerably increase the peak thermodynamic states and the possibility of ignition inside the bubble. To demonstrate this strengthening effect, first a one-dimensional shock wave diagram is analyzed, then the results are compared with those concerning shock-focusing.

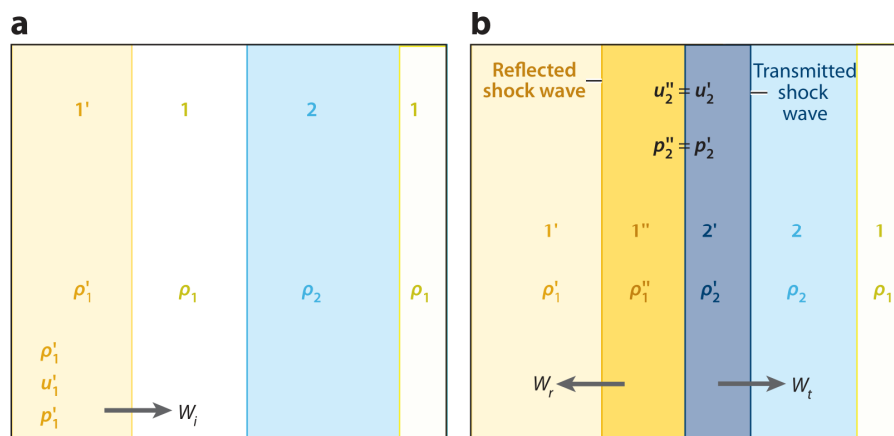


Figure 1-2. Schematic illustration of 1D shock diagram in a gas slab with $At > 0$: (a) preshock, (b) postshock.[80]

1D shock diagram when $At > 0$

Figure 1-2 illustrates a 1D shock transmission and reflection diagram of the heavy case: subfigure (a) presents the pre-shock state, and subfigure (b) presents the post-shock state. Applying conservation principle across the shock wave, one can easily relate the post-shock variables to pre-shock variables as

$$\rho_1 W_1 = \rho_1' (W_1 - u_1') \quad (1.1)$$

$$p_1 + \rho_1 W_1^2 = p'_1 + \rho'_1 (W_1 - u'_1)^2 \quad (1.2)$$

$$h_1 + \frac{W_1^2}{2} = h'_1 + \frac{(W_1 - u'_1)^2}{2} \quad (1.3)$$

where the post-shock variables are marked by prime, ρ is density, p is pressure, h is specific enthalpy, u is flow speed, and W_1 is the shock speed. For an ideal gas, the equation of state (EOS) is

$$p = \rho RT \quad (1.4)$$

For the calorically perfect gas, the EOS can be written as

$$p = \rho(\gamma - 1)e \quad (1.5)$$

where $\gamma = C_p/C_v$, e is the specific internal energy, and the enthalpy can be written as

$$h = e + p / \rho = \frac{\gamma RT}{\gamma - 1} \quad (1.6)$$

Substituting these EOS into the conservational equations, the results are the well-known Rankin-Hugoniot relation

$$\frac{p'_1}{p_1} = \frac{\frac{\gamma + 1}{\gamma - 1} \frac{\rho'_1}{\rho_1}}{\frac{\gamma + 1}{\gamma - 1} \frac{\rho'_1}{\rho_1} - 1} \quad (1.7)$$

The post-shock density ρ'_1 can be evaluated by incident Mach number $M_1 = W_1 / \sqrt{\gamma_1 R_1 T_1}$ as

$$\rho'_1 = \frac{(\gamma + 1)M_1^2}{2 + (\gamma - 1)M_1^2} \rho_1 \quad (1.8)$$

the post-shock speed u'_1 is calculated as

$$u'_1 = \left(1 - \frac{\rho_1}{\rho'_1}\right) W_1 = \left(1 - \frac{(\gamma + 1)M_1^2}{2 + (\gamma - 1)M_1^2}\right) W_1 \quad (1.9)$$

By further manipulations, the post-shock temperature T'_1 is

$$T'_1 = \left[1 - \frac{2\gamma}{\gamma + 1}(M_1^2 - 1)\right] \frac{2 + (\gamma - 1)M_1^2}{(\gamma + 1)M_1^2} \cdot T_1 \quad (1.10)$$

The situation becomes complicated if a second gas and an interface are considered. Apart from the knowns of the incident shock wave, given the initial conditions of the unshocked second gas, ρ_2, p_2, γ_2 , the goals are to find the states across the shocked interface $\rho''_1, \rho'_2, u''_1, u'_2, p''_1, p'_2$, the reflected shock speed W_r , and the transmitted shock speed W_t . Here, the variables with superscript ' represent states that get shocked once, while the '' ones represent states that get shocked twice. This is a classical problem whose solution was given by Courant & Friedrichs [35],

and here the theoretical results reported by Mikaelian [26] is presented. First, a transcendental equation of the unknown x must be solved to find the final state after shock impaction,

$$\frac{x - p_2 / p_1'}{\sqrt{x + [(\gamma_2 - 1) / (\gamma_2 + 1)] p_2 / p_1'}} = \frac{1}{\sqrt{1 + [(\gamma_1 - 1) / (\gamma_1 + 1)] p_2 / p_1'}} \quad (1.11)$$

$$= \frac{\sqrt{\frac{\gamma_2 + 1}{\gamma_2 - 1}} \sqrt{\frac{\rho_2}{\rho_1}} \left(1 - \frac{p_2}{p_1'} - (x - 1) \times \sqrt{\frac{\gamma_1 - 1 + (\gamma_1 + 1) p_2 / p_1'}{x(\gamma_1 + 1) + \gamma_1 - 1}} \right)}{\sqrt{1 + [(\gamma_1 - 1) / (\gamma_1 + 1)] p_2 / p_1'}}$$

To ensure a reflected shock wave, the solution must satisfy $x \geq 1$. Except for specific cases, Eq. (1.11) cannot be solved analytically. With x at hand, other variables follow immediately:

$$\frac{\rho_2'}{\rho_2} = \frac{(\gamma_2 + 1)x + (\gamma_2 - 1)p_2 / p_1'}{(\gamma_2 - 1)x + (\gamma_2 + 1)p_2 / p_1'} \quad (1.12)$$

$$\frac{\rho_1''}{\rho_1} = \frac{[\gamma_1 + 1 + (\gamma_1 - 1)p_2 / p_1'][(\gamma_1 + 1)x + \gamma_1 - 1]}{[\gamma_1 - 1 + (\gamma_1 + 1)p_2 / p_1'][(\gamma_1 - 1)x + \gamma_1 + 1]} \quad (1.13)$$

$$p_1' = p_1'' = xp_1' \quad (1.14)$$

$$(u_1'')^2 = (u_2')^2 = \frac{2p_2'}{\rho_2} \frac{(1 - p_2 / p_2')^2}{\gamma_2 + 1 + (\gamma_2 - 1)p_2 / p_2'} \quad (1.15)$$

$$W_t = u_1' / (1 - \rho_2 / \rho_2') \quad (1.16)$$

$$W_r = (u_1' \rho_1' / \rho_1'' - u_2) / (1 - \rho_1' / \rho_1'') \quad (1.17)$$

If chemical reactions are considered, the calorically perfect gas is no longer accurate as γ varies as temperature ranges from the standard state (around 300 K) to the flame (around 3000 K). In this case, a more accurate EOS, the thermally perfect gas, is a better choice, and the shocked states can be estimated by performing a 1D numerical study.

Strengthening effect of shock-focusing

The shock focusing phenomenon (SFP) is the process of the transmitted shock wave converging inside the heavy bubble, and here the heavy bubble acts as an optical lens. The process of SFP is presented in Figure 1-3. As the energy accumulates during SFP, the temperature and pressure near the SFP will be considerably high and capable of ignition.

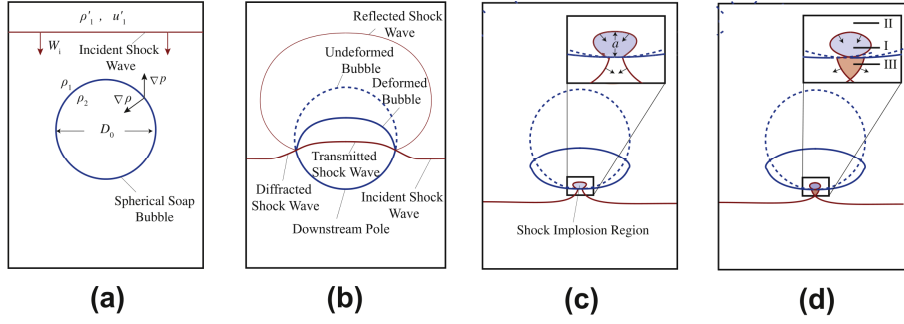


Figure 1-3. Schematic illustration of SBI when $At > 0$ in Ref.[88]. (a) the initial condition for a free-falling bubble with planar shock wave emerging from above, (b) the shock refraction process. The transmitted shock wave travels slower than the diffracted waves outside the bubble, and a reflected shock wave travels upstream, (c) the shock implosion region at bubble south pole, (d) just after the shock focusing when the diffracted shock waves meet a south bubble pole.

Table 1-1. The post-shock temperature, T_2' , and pressure, p_2' and ignition delay time $\tau_{i,1D}^m$ evaluated from 1D slab geometry, and the measured ignition delay time τ_i^e in RSBI experiments. [88]

M	T_2' (K)	p_2' (atm)	$\tau_{i,1D}^m$ (μ s)	τ_i^e (μ s)
1.34 ± 0.01	401	2.25	> 5000	300 – 400
1.65 ± 0.02	506	3.79	> 5000	270 – 330
2.01 ± 0.01	690	6.63	> 5000	70 – 90
2.83 ± 0.01	1155	13.96	11	5 – 10

In Ref.[88], the ignition delay times (IDT) evaluated from a 1D slab theory are compared with those measured from the RSBI experiments. These results are shown in Table 1-1. For the lower Mach case with $M < 2.83$, all $\tau_{i,1D}^m$ values are much larger than τ_i^e , which means that the bubble cannot even get ignited by the post-shock states of 1D slab theory. Thus, the 1D slab theory is not able to explain the ignition in RSBI experiments, and the strengthening effect of shock focusing must play an important role.

1.3 Gaps in RSBI studies

In 2012, Haehn et al. [88] was the first one to study the possibility of ignition and the later combustion by shock focusing in RSBI using experimental method. This experiment was of great interest as it demonstrated for the first time that an isolated spherical mixture could be ignited by shock focusing alone. In addition, two limiting combustion scenarios were found in this experiment. Nevertheless, as the ignition and later combustion occurred

on a microsecond scale, limited combustion details were revealed by the experiment, which made it difficult to analyze the ignition, shock-flame interaction, the coupling between hydrodynamic and chemical process, and the underlying mechanisms of these two limiting combustion phenomena. On the other hand, numerical simulations are helpful. However, to the author's knowledge, no numerical study explained the experimental results satisfactorily. As the setups in this experiment were not faithfully followed by some numerical studies, I would like to review the essences in Haehn et al.'s experiment [88] to avoid any misunderstanding.

1.3.1 Haehn's RSBI experiments

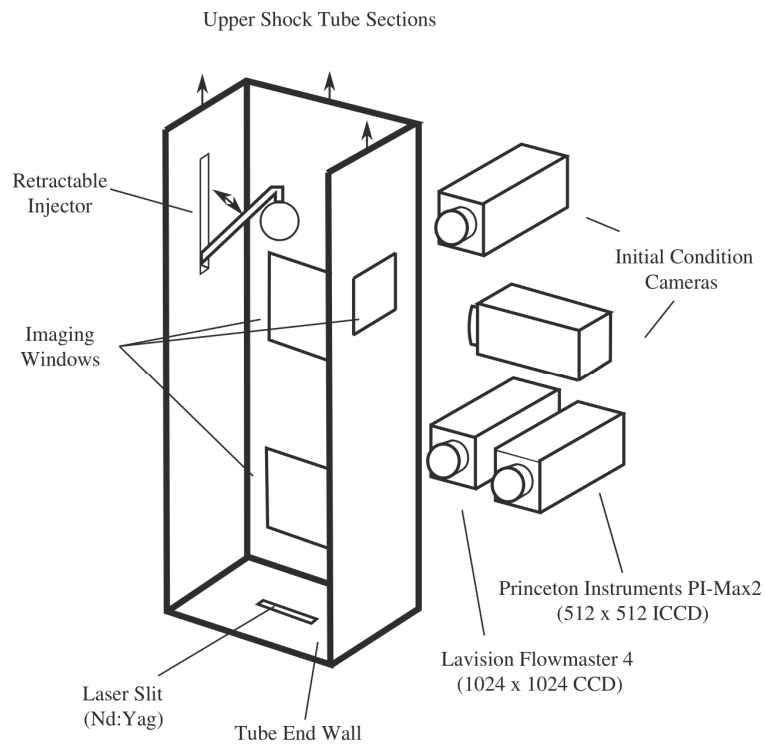


Figure 1-4. Schematic of the experimental setup.[88]

This experiment is performed in a vertical shock tube at the Wisconsin Shock Tube Laboratory. The schematic of the experimental setup is shown in Figure 1-4. The surrounding gas was pure N_2 , and the bubble mixture composition was $X(H_2:O_2:Xe) = 2:1:3.76$ for the reactive case and $X(O_2:Xe) = 51:49$ for the inert case, with the corresponding Atwood numbers close to 0.473 and 0.484, respectively. Before the shock wave emerges from above, the gas bubble is prepared by a pneumatic retractable injector. After the injector is retracted into a slot on the side wall, the heavy bubble will be released and in the state of free-falling in the surrounding nitrogen atmosphere. Later, a planar shock wave is generated above. Thus, a clean field is maintained by the time the shock interacts with the bubble. Although the incident shock strength and bubble gas composition can be well controlled, the bubble interface is subjected to possible perturbation, such as non-sphericity with eccentricity e . According to

Ranjan[63], who first studied the ISBI using this shock tube, the eccentricity of the bubble was 0.26 ± 0.03 . However, Fig.8(a) in this Ref.[88] implies a larger eccentricity value around 0.44.

Figure 1-5 presents the composite images of the recording on the midplane of the bubble with incident shock $M = 1.65$ and 2.83 , respectively. The interfacial morphology of the bubble is captured by tracing droplets from the bursting soap film using the planar Mie scattering technique, and the combustion signals are detected by recording the distribution of the OH^* using chemiluminescence. Figure 1-6 presents the temporal history of transverse bubble diameter (TBD), which is the distance of the primary vortices illustrated in Figure 1-6 (c) labeled by W_{TBD} . All time scales are normalized by the hydrodynamic scale defined as

$$\tau_{\text{H}} = D_0 / W_i \quad (1.18)$$

where D_0 is the nominal initial bubble diameter and W_i is the incident shock speed, for $M = 1.65$ and 2.83 , $\tau_{\text{H}} = 68$ and $40 \mu\text{s}$, respectively. The normalized TBD length scale Λ_{y}^* is defined as $\Lambda_{\text{y}}^* = W_{\text{TBD}} / D_0$.

Two limiting combustion phenomena depend on incident shock strength are shown in Figure 1-5. Both diagnostics are performed twice in a single shot of experiment: first, the Mie scattering image is recorded at $t_{\text{M},1}^*$ with negligible exposure (around 10 ns) compared to the hydrodynamic time scale, and the chemiluminescence is recorded at $t_{\text{C},1}^*$ with exposure duration labeled as $\Delta t_{\text{C},1}^*$. Later, the same procedures are repeated the second time. In Figure 1-5(a), which is the lower Mach number limiting case ($M = 1.34, 1.65, \text{ and } 2.01$), the flame begins at a single location near the SFP and propagates through both exposures. As the shocked bubble travels downstream, the flame propagates in the transverse direction, which results in a triangular cloud of combustion signals. For the higher Mach number limiting case ($M = 2.83$), Figure 1-5(b) presents dramatically different chemiluminescence compared with Figure 1-5(a). Instead of a triangular combustion cloud, which implies flame speed comparable with the shocked bubble speed, an oblate cloud occurs with a much faster flame speed. This indicates that the premixture is fully consumed before any coherent vortex structures develop. No red signal presents as the combustion has finished before the second exposure starts. Addition measurements of TBD history in Figure 1-6 show that, for the lower Mach limit, the TBD history is barely affected by reaction until $t^* > 10$, while for the higher Mach limit, the TBD values in reactive case increase faster and are larger than the non-reactive counterparts when $t^* > 2$.

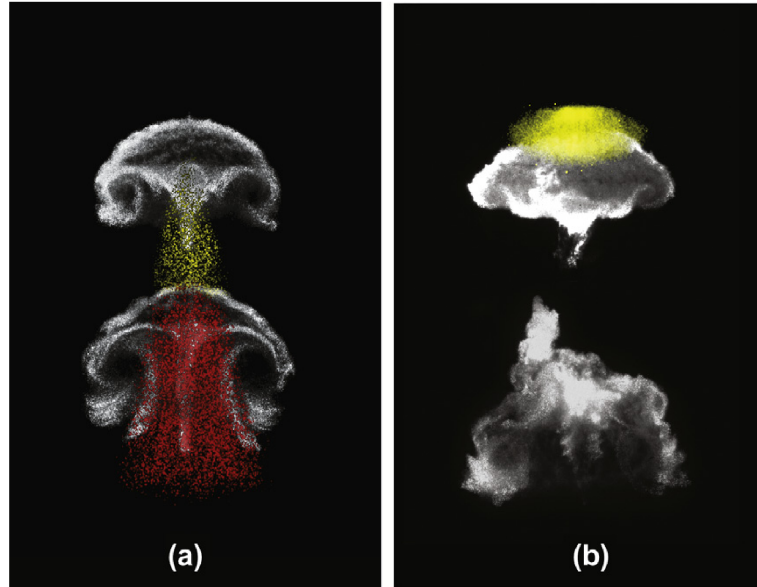


Figure 1-5. Composite images that show two limiting cases of combustion in RSBI. *white* signals: Mie scattering images indicating the location of bubble interface; *yellow* or *red* signals: chemiluminescence images indicating flame during the first exposure or the second. (a) $M = 1.65$, $t_{M,1}^* = t_{C,1}^* = 3.6$, $t_{M,2}^* = t_{C,2}^* = 6.6$, $\Delta t_{c,1}^* = \Delta t_{c,2}^* = 3.0$. (b) $M = 2.83$, $t_{M,1}^* = 1.7$, $t_{M,2}^* = 3.7$, $t_{C,1}^* = 1.3$, $t_{C,2}^* = 2.3$, $\Delta t_{c,1}^* = \Delta t_{c,2}^* = 0.6$. [88]

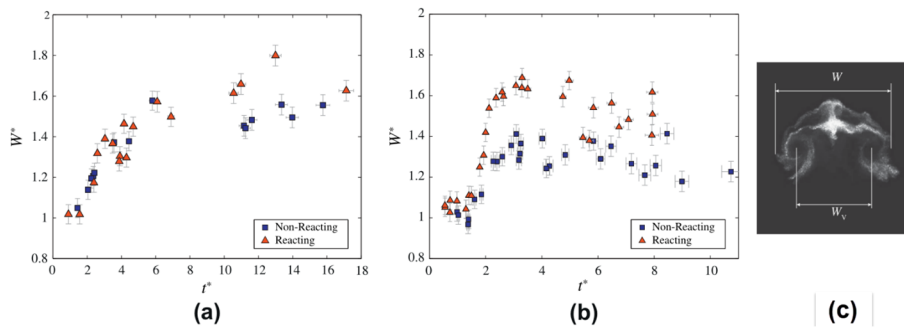


Figure 1-6. The normalized TBD Λ_y^* as a function of normalized time t^* . The presented data is of the reacting case and non-reacting case of (a) $M = 1.65$; (b) $M = 2.83$; (c) illustration of TBD W_{TBD} . [88]

The shock strength covered in this experiment ranges from 1.3 to 2.9. Apart from this journal paper, extra results can be found in the Ph.D. thesis [86] and the conference paper [85] by the same author.

1.3.2 Relevant numerical studies

Table 1-2. The setup in Haehn's RSBI experiments and related numerical works

Unshocked States	Bubble shape	Shock Mach number, M	Detonation Initiation	Grid size Δ_{\min} (μm)
------------------	--------------	------------------------	-----------------------	---

Haehn et al.'s experiment (2012)[86, 85, 88]	$T_1 = 295$ K, $p_1 = 1.00$ atm.	Nearly spherical, with eccentricity $e = 0.26-0.44$	1.34, 1.65, 2.01, 2.83	Uncertain	Not applicable
Diegelmann et al. (2016) [107]	$T_1 = 350$ K, $p_1 = 0.25, 0.50, 0.75$ atm.	2D simulation, cylindrical bubble	2.30	Yes	59
Diegelmann et al. (2016) [108]	$T_1 = 350$ K, $p_1 = 0.50$ atm.	2D simulation, cylindrical bubble	2.13, 2.19, 2.30, 2.50, 2.90	Yes	59
Diegelmann et al. (2017) [112]	$T_1 = 295$ K, $p_1 = 1.00$ atm.	3D simulation, 1/4 of the spherical bubble	2.83	Yes	125
Sidharth GS & Graham V Candler (2017) [109]	$T_1 = 295, 368.75$ K, $p_1 = 1.00, 1.25$ atm.	3D simulation, 1/4 of the spherical bubble	2.83	Yes	250

To the author's knowledge, four numerical studies [107–109, 112] were conducted to explain the experimental observations, but none of them reproduced the experimental data faithfully. Moreover, distinct deviations in initial setups exist between the experiment by Haehn et al. [88] and the four abovementioned simulations, as shown in Table 1-2. These include the incident Mach number M , the initial temperature T_1 , and the initial pressure p_1 , which affect the ignition delay time. Also, the 2D cylindrical bubbles and 3D spherical bubbles create different shock focusing strengths and, hence, different ignition mechanisms [30, 43]. Additionally, the detonation predictions in these numerical studies lacked rigorous grid-convergence proof. As numerous detonation simulations [32, 44, 49, 78, 91] have clearly indicated that inadequate grids may lead to spurious detonation waves, it is necessary to conduct a proper grid-convergence study before drawing any conclusions. Oran et al. [32] showed that the under-resolving grids produced spurious weak transverse waves and affected the detonation cell sizes and regularity. Mahmoudi and Mazaheri [78] performed systematic grid resolution studies and concluded that at least 50 cells per half reaction length were required for the physical prediction of regular cell structures. Despite the various grid convergence tests in Ref. [107–109, 112], their tests did not directly check the importance of the grid resolution on the flame structure, which may affect the final combustion configurations, according to Oran and Gamezo [65].

1.3.3 Gaps

In summary, the main gaps in RSBI studies are

1. The processes of ignition, flame propagation, shock-flame interaction, and coupling between hydrodynamic and chemical mechanisms are not well revealed in Haehn et al.'s experiment[88] for detailed analyses.

2. The combustion phenomena in the lower Mach number limiting cases, e.g., $M = 1.34$, 1.65 , and 2.01 , are not reproduced, even studied, by any numerical work following the experimental setup.
3. Although the combustion phenomena in the higher Mach number limiting case, e.g., $M = 2.83$, are studied, they were poorly reproduced by previous numerical results.
4. All detonation phenomena in the relevant numerical works are suspected of pseudo-detonation. Rigorous grid-convergence studies based on flame structures are necessary.

1.4 Objectives

In the current thesis, the RSBI problem is numerically studied by solving the compressible reactive multi-component Navier-Stokes equations. To get physically correct numerical simulation on the direct detonation or DDT phenomena, an AMR detonation solver is built on an open-source AMR framework. The comprehensive H_2/O_2 combustion mechanism is utilized as it is crucial to reproduce the experimental DDT results [107, 108, 112] in a similar scenario. The main objectives are:

- Build and validate a compressible combustion AMR solver, Fire.
- Numerically reproduce the low and high Mach number cases in Haehn et al.'s RSBI experiment [88]. Two representative cases, namely $M = 1.34$ and 2.83 , will be focused on. The shock-bubble interaction, combustion modes, shock-induced ignition, effects of combustion on the wave system, vorticity and mixing, and different contributions of combustion modes will be investigated.

1.5 Outline of this thesis

After the introduction part in this chapter,

- Chapter 2: Reviews of literature of classical RMI and ISBI works, reactive RMI and RSBI studies, and the AMR methods.
- Chapter 3: Description of the governing equations, AMR methods, and other numerical methods in this thesis.
- Chapter 4: Extensive code validation on inert/reactive, one-dimensional/two-dimensional problems.
- Chapter 5: Grid-convergence studies of the $M = 1.34$ RSBI case and demonstration of the AMR criteria based on reactant mass fraction.
- Chapter 6: Results and discussions of two combustion modes and ignitions in the RSBI simulation. The shock-bubble interaction, combustion modes, shock-induced ignition, effects of combustion on the wave systems, vorticity and mixing, and different contributions of combustion modes will be discussed.
- Chapter 7: Conclusion.

2. Literature Review

2.1 Non-reactive RMI

The RMI is found when a shock propagating through an inhomogeneous mixture, of which a classical configuration is a perturbed interface separating two different fluids accelerated by a shock, and the perturbation will be amplified. The study of RMI is fundamental and found in a variety of scientific topics. In this thesis, only the gasdynamic type RMI will be covered.

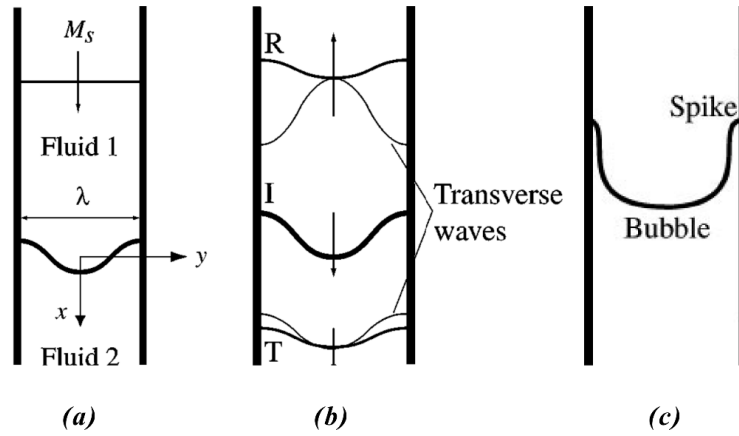


Figure 2-1. Basic configuration for the RMI problem. (a) Discontinuous interface with a single-mode perturbation. Fluids 1 and 2 have different densities and adiabatic indexes. (b) Transmitted wave (T), material interface (I), reflected wave (R), and transverse wave after the acceleration. (c) The nonlinear stage: asymmetric spike and bubble structures. From Ref.[52].

Figure 2-1 presents the basic configuration and evolution of RMI with a single-mode perturbation. Initially, in subfigure (a), Fluid 1 and Fluid 2 are divided by an interface given by $a(x, t = 0) = a_0 \cos(2\pi y / \lambda)$ and an incident planar shock wave propagates from Fluid 1 to Fluid 2. Before the interaction, these two fluids are of the same pressure and temperature but different densities and adiabatic indexes. The density pair is defined by the Atwood number $At = (\rho_2 - \rho_1) / (\rho_1 + \rho_2)$, and for the *heavy/light* case, $At < 0$, while for the *light/heavy* case, $At > 0$. In most cases, the acoustic properties and sound speeds of these fluids are also different. When the planar shock wave travels through the interface in subfigure (b), a transmitted shock wave occurs in Fluid 2, and a reflected compression wave (for $At > 0$) or rarefaction wave (for $At < 0$) occurs in Fluid 1 due to mechanical equilibrium. The interface evolution can be explained either by the baroclinic effect which is the misalignment of pressure and density gradient on the interface, or by the pressure perturbations caused by the transmitted and reflected waves

near the interface. Eventually, the perturbation will be non-linear and characterized by the asymmetric spike and bubble structures in subfigure (c).

Richtmyer [5] treated the fluids as incompressible after the transmitted shock wave travels far from the interface and used the linear theory of Taylor [1] to model the growth of amplitude $a = a(t)$ as

$$\frac{d^2}{dt^2} a(t) = kg(t)a(t)At \quad (2.1)$$

Where $k = 2\pi/\lambda$ is the wavenumber of perturbation, $g(t) = [v]\delta_D(t)$ represents the interface gains speed $[v]$ after the acceleration and δ_D is the Dirac function. Eq. (2.1) remains rigorous as long as the perturbation amplitude is small $ka \ll 1$. By integrating Eq. (2.1) once with respect to time, Richtmyer obtained the situation immediately after the acceleration as

$$\frac{d}{dt} a_{imp}(t) = k[v]a_0At \quad (2.2)$$

This equation holds long after the shock acceleration while the perturbation is still small to remain in the linear regime, and it is always referred to as the impulsive model. The growth rate in the impulsive model is constant and characterized by the interface speed $[v]$ and initial amplitude a_0 . Richtmyer also found that in Eq. (2.1), the post-shock states rather than the pre-shock states produced a better agreement with the numerical solution of Eq.

(2.2), i.e., $\frac{d}{dt} a_{imp}(t) = k[v]a'_0At'$, where the prime denoted the post-shock states. The impulsive model matches well with 2-dimensional numerical results for the light/heavy interface but shows poor performance for the heavy/light interface. Meyer & Blewett [8] pointed out better quantitative agreement could be achieved by using the averaged amplitude $(a_0+a'_0)/2$ and the postshock At' . Vandenboomgaerde [34] obtained a unified equation valid for both positive and negative Atwood number cases using the average of these two cases

$$\frac{d}{dt} a_{imp}(t) = k[v](a_0At + a'_0At')/2.$$

The impulsive model is attractive as it is simple and predicts well for small amplitude and weak shock strength. However, it loses its validity once the perturbation is no longer small. Grove [24] specified that the approximated upper bound of the validation is $t_{max} \approx 1/(k^2At'[v]a'_0)$ and $a_{max} \approx 0.1\lambda$. Out of this range, the compressibility and non-linearity must be considered. Also, it cannot describe the interface behavior when the transmitted shock lies close to the interface.

To show the weakness of the impulsive model, Mikaelian [26] designed a limiting case with gas pairs of the same density but different adiabatic indexes, i.e., $\rho_1 = \rho_2$ but $\gamma_1 \neq \gamma_2$. According to Eq. (2.2), for this interface At

= 0, thus $\frac{d}{dt}a_{imp}(t) = 0$. This is referred to as the “freeze-out” case of the RMI, for which the initial perturbation will stay the same though the fluid properties change across the interface. However, the numerical experiments show the growth rate of this case is not zero, and the results agreed well with Fraley’s analysis [16] of Eq. (2.1) considering compressibility. This emphasizes that the RMI is motivated by compressibility and wave refraction and cannot be simply treated as shock-accelerated RTI.

At the late time, the non-linear model must be used to accurately predict the asymmetric behaviors of spike and bubble which no longer lie in the small-amplitude regime. The straightforward idea is to expand the perturbation beyond first-order. The second-order analysis proves that the movement of spike and bubble is distinct from the beginning, and the velocity is given as $v_s(t) = k[v]At'a_0(1+k[v]At'a_0t)$ and $v_b(t) = k[v]At'a_0(1-k[v]At'a_0t)$ respectively.

As the early stage is mainly controlled by the compressibility while after that the nonlinearity dominates, Zhang & Sohn [29] treated these two stages separately and bridged them using asymptotic methods: a 3rd-order perturbation method produced Taylor series that could be evaluated term-by-term, and the valid range is extended by Padé approximation. Later, Zhang & Sohn [36] obtained an explicit non-linear theory applicable from early to later times based on three-dimensional RMI analysis. Mikaelian [55] reported an explicit expression of amplitude suitable for both RTI and RMI at arbitrary Atwood numbers.

The single-mode perturbation in Figure 2-1 is the simplest case for RMI. In a realistic application, the interface can be modeled as a multi-mode perturbation. The multi-mode perturbation can be decomposed into a series of harmonic perturbations, and its growth rate is the superposition of all the outcomes of the harmonic terms.

In the experiment, the RMI evolution highly depends on the initial condition. Improving techniques are developed to generate a well-defined perturbation interface [117]. They are mostly divided into two categories: discontinuous interface and diffusive interface. The nitrocellulose membrane is widely used to produce the distinct interface, but its fragments unavoidably affect the flow and suppress perturbation growth [64]. An alternative method is the gas film [62], which generates continuous gaseous interfaces. However, the diffusive gaseous layer mitigates density/pressure gradients and baroclinic torques, thus suppress the growth rate from the beginning. Nowadays, the soap film is the most promising method to form a distinct interface with the least interference. It has been used to produce numerous heavy/light bubble experiments that can be matched well by high-resolution numerical studies [17, 73, 114, 118]. Generally, the agreement is better in the heavy-bubble case than the light-bubble case.

The numerical analysis of RMI dates to the very beginning by Richtmyer [5]. In this work, he linearized the Euler equation and acquired a wave equation of pressure perturbation, which was solved by a finite difference method. It is worth noting that the computation task was performed by the MANIAC.

Modern RMI simulations are mostly performed by solving compressible Euler equations in either 2D or 3D domain. As the majority lies in the low-Mach regime, most studies adopt the calorically perfect gas as the EOS, i.e., the polytropic exponents γ_1 and γ_2 are constant. The conventional schemes for compressible flow are suitable.

Holmes et al. [40] compared the results of three different hydrodynamic codes, either of which used front tracking method, or 2nd-order scheme, high-order piecewise-parabolic method, or AMR method with the monotone upstream-centered schemes for conservation law reconstruction (MUSCL) scheme. All these three codes produce similar growth rates and match with accurate theoretical outcomes. Peng et al. [57] investigated the vorticity of a diffusive interface and found out that, at the intermediate stage the majority of the circulation growth depended on the secondary baroclinic effect.

Three-dimensional simulation of RMI is challenging but valuable for late-stage non-linear, mixing, and turbulent research. Gowardhan & Grinstein et al. [79] studied the shocked gas curtain using implicit large eddy simulation and reported that the initial condition affected the first-shock stage little, but had a dominant effect on the reshocked stage. They also found that the *root-mean-square* of the initial interface was relevant for whether the shock-driven flow lay in linear ballistic or nonlinear mode-coupling regimes.

One prototype of the three-dimensional RMI study is the shock gaseous cylinder interaction. This model helps us to understand the jet injection to a supersonic crossflow (JISC) and avoid hazards in natural gas storage [67].

2.2 Non-reactive SBI

Experimental study on SBI using conventional shock-tube is pioneering by Markstein [2] and Rudinger [3], who studied the passage of shock wave across a flame front of a nearly spherical shape. To simplify this problem, most studies were performed using nonreactive gases. During the combustion process of RSBI, the chemical flow field will be highly inhomogeneous due to the shock interactions and reflections. Rudinger & Somers [4] developed a new theory to explain the behaviors of the inhomogeneous compressed gas mixture and provides a simple theory to calculate the response of the bubble to the shock acceleration. This monumental work enlightened rich studies of the ISBI.

Hass & Sturtevant [17] studied the ISBI using both cylindrical and spherical bubbles and applied a finite-amplitude waves model to study the mechanism related to turbulence and mixing enhancement. The spherical

bubble is generated using soap film, while the cylindrical bubble is capsuled in thin nitrocellulose membranes. In this study, the authors observed that the reflected wavefronts at the windward side interface exhibited typical features in optical and acoustic scattering in the heavy-bubble scenario.

Jacobs [22] performed experiments of ISBI in a horizontal shock tube that utilized a laminar jet to generate cylindrical inhomogeneity, which avoided the disturbance of solid film remnants during the testing process. Planar laser-induced fluorescence (PLIF) technique was used to not only improve the visual quantity but also allowed for the measurement of species distribution, hence, the mixing characteristics of ISBI. Tomkins et al. [72] revisited the mixing problem of a heavy SBI using a quantitative PLIF method. Experimental results of instantaneous mixing rate, χ , were obtained for the first time based on the spatial concentration distribution. Two stages mainly characterize the mixing process: at the first stage before the emergence of secondary instability, the primary instability accelerates mixing through simple interfacial stretching in the vortex cores; at the second stage, the mixing is enhanced by the small vortices generated by the secondary instability. Results show that the mixing is mainly related to the primary instability. A stratified non-turbulent region, called the *bridge*, also played an important role through a non-turbulent process by stretching interface. The numerical study reported by Shankar et al. [81] addressed that the initial setup of interface gradient and the uncertainty induced by the acetone traces were crucial for primary vortex generation and mixing. Ranjan et al. [69] replenished this ISBI problem of light bubble case.

In a vertical shock tube, Ranjan et al.[73] performed an ISBI experiment with the incident shock wave interacting with a free-falling bubble. The gas inhomogeneity was prepared by a retractable injector which was removed after releasing the bubble. Thus, a clear field was maintained by the time shock arrived. Planar imaging techniques were used to record the bubble morphology. A wide range of Mach numbers (2.0 – 5.0) was covered in this study, and the experimental results were in good accordance with numerical counterparts.

A variety of studies on ISBI have been reported using bubbles of different shapes, such as spherical bubbles and bubbles of rectangular or triangular shapes. Wang et al.[93] developed a method of generating different polygonal bubble interfaces using the soap film technique. The angular vertexes were connected with thin pins to avoid singularity and relax surface tension. This experimental method provided clear images of the shock system and had been a strong tool to study the SBI. Zhai et al.[84] performed experimental studies of ISBI using high-speed schlieren photography with an improved temporal resolution. The morphing of the bubble was quantitatively recorded using three length scales, and good agreement was achieved between simulation and experiments.

Apart from the experiments, numerical studies help to understand the dynamic of wave systems that are difficult to be ascertained by experiments.

Picone and Boris [18] performed numerical studies using the FAST2D code against the ISBI experiments in Ref. [17], and their emphasis was on the dynamics of the long-live vortex. The compressible Euler equations were solved with flux corrected transport to evaluate the inviscid flux. Far from the wave system, the inviscid flux was reconstructed using a 2nd-order scheme. This numerical study revealed the vorticity deposition and nonlinear interaction on the bubble interface, which was hard to be concluded in either density diagram or experimental shadowgraph.

Niederhaus et al. [68] reported a substantial spherical ISBI numerical study on both positive and negative Atwood numbers with incident shock strength varied from 1.1 to 5.0. The Euler equations were closed by the EOS of calorically perfect gas and solved using an operator-splitting 2nd-order Godunov method. The volume of fraction (VOF) method was utilized to extend the single-fluid algorithm to a multi-fluid model. By normalization based on 1-dimensional gas dynamic analyses, the integral features of ISBI in a wide parameter space of At and M collapsed into a similar trend. The new circulation model was induced to best fit the data across the parameter space. The 3D simulation showed that disorder motion and turbulent features were generated by complex shock systems resulted from shock refraction, reflection, and diffraction.

Tritschler et al. [100] numerically evaluated the effect of the initial uncertainties in Tomkins et al. [72]'s membraneless experiment using the multicomponent flow solver INCA. The Navier-Stokes equations were utilized to model the flow, and the inviscid fluxes were reconstructed using weighted essentially non-oscillatory scheme (WENO-CU6) and evaluate by Lax-Friedrichs flux with entropy fix. Three main sources of uncertainties were considered, including incident shock Mach number, contamination of the bubble composition induced by tracer species, and initial deviation of the bubble shape from the ideal cylindrical shape. 125 two-dimensional well-resolved simulations were performed and the best fit to the experimental results could be achieved. This study suggested that the mixing quantities, such as total mixing rate (TMR), were highly dependent on deviations in the incident shock strength and mass fraction of the tracer species. The precise measurement of bubble gas component and incident shock strength is crucial for the accurate reproduction of the experiment.

Fan et al. [87] reported abundant ISBI results on different initial shapes at the early stage, including rectangle, ellipse, diamond, and two different triangles, in the light/heavy interface. The Euler equations were solved by 2nd-order scheme both temporally and spatially using the AMR program VAS2D. The vorticity value of different

initial bubble shapes could be well predicted by the theoretical prediction arising from the shock polar analysis in Ref. [27].

Ding et al. [114] studied the 3D effects in ISBI problems with 2D, 3D concave, and 3D convex SF₆ cylindrical bubbles both experimentally and numerically. Compared with the 2D case, either oppositely or identically signed principal curvatures on the 3D cases produced more complex pressure fields and 3D baroclinic vorticity.

2.3 Reactive RMI and ISBI

In supersonic combustion, the complex shock system is highly coupled with the flame surfaces, and reactive RMI phenomena arise from the SFI. It is believed that this instability is not only responsible for the turbulent transition but also crucial for flame propagation in turbulent flames.

Reactive RMI

In Markstein [2] and Rudinger [3]’s experiments which date back to 1957 and 1958, the incident planar shock wave interacted with a nearly spherical flame front. Since the combustion generated both pressure and density disturbance in the flow, these disturbances then interacted with shock waves, and through the baroclinic mechanism, produced strong vorticity in the flow field. Markstein [2] observed that when the shock wave accelerated the curved flame front, spike (similar to that in RMI) and inflection structures occurred, and the volumetric burning rate increased after the passage. Rudinger [3] pointed out a very fine-grained turbulent burning zone will be created by the considerably large vortex.

After Markstein [2] and Rudinger [3]’s studies, the experimental studies on reactive RMI had been stopped for a long time till recent years, even though the SFI phenomena are widely observed in supersonic combustion studies. There is a clear need to design simple experiments for deep understandings of the reactive RMI, and most related research during 1960 to recent years are numerical studies.

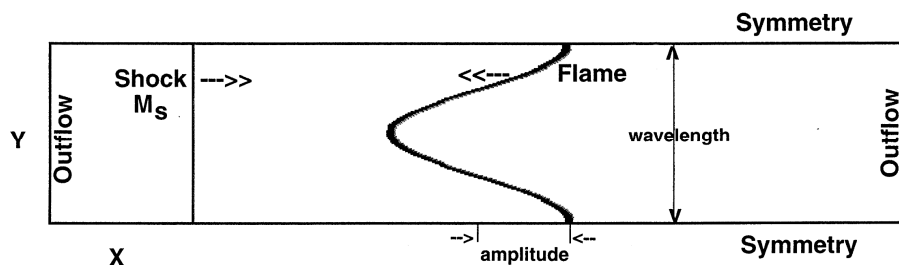


Figure 2-2. The numerical setup for the 2D reactive RMI study with the sinusoidal perturbed flame surface in Khokhlov et al. [37]

A more simplified model is to treat the flame front as a sinusoidal perturbed interface. Figure 2-2 presents the numerical setup in Khokhlov et al. [37]’s work: the channel on the RHS of the flame was fully burnt, while the

other part of the channel was filled by premixed unburnt gas. In this study, the reactive NS equations were solved with an ideal EOS model and a one-step reaction model. The governing equations were integrated using an explicit 2nd-order Godunov scheme. Comparison of inviscid and viscous numerical results show that the growth of secondary instabilities along the funnel was suppressed by microscopic viscous terms in NS equations. Various incident shock strength ($M = 1.5$ to 2.0), amplitudes, and wavelength of the perturbation were covered. Khokhlov et al. [37] found that:

- The energy release rate increased due to the SFI, and this increase did not exceed a factor of 20 or 30. Two effects were responsible for it, an increase of the flame surface area and an increase of the density. The second effect is generally related to the 1D gas compression effect of the incident shock, and these two effects are later referred to as two-dimensional and one-dimensional effects by Kilchyk et al. [83], respectively.
- The growth rate of the reactive perturbation depended weakly on the incident shock strength, as the funnels choked when the velocity of the cold mixture approached sound speed.
- The amplitude of the perturbation strongly impacted the energy release rate, as more vorticity and small-scale funnel structures were generated for larger amplitude.
- If the flame thickness was small compared to perturbation wavelength, the energy release rate per surface area was practically independent of the wavelength.
- Compared with the 2D case, the maximum heat release rate, the growth rate of heat release, and the length of funnel structure were larger by a factor of two or three in the 3D cases.

Khokhlov et al. [37] also pointed out that if the pressure or incident shock strength considerably increased, strong vorticity would lead to direct initiation of detonation or DDT.

Kilchyk et al. [83] adopted similar computational setups from Khokhlov et al. [37]'s work and analyzed both the effect of compressive or expansive waves in 2D simulations. Reacting NS equations were solved using a 2nd-order scheme, and the reaction was modeled by a 1-step global mechanism. The effects of SFI on energy release rate were ranked to either one-dimensional or two-dimensional effect: the one-dimensional contribution was evaluated by an analytic methodology based on the one-dimensional gas dynamics; the two-dimensional contribution, which was related to flame distortion and shock system, was evaluated by subtracting the one-dimensional contribution from the overall growth factor of fuel consumption rate. The one-dimensional effects grew monotonously with increasing Mach strength, while the two-dimensional effect peaked at around $M = 1.3$.

Chen et al. [111] studied the interaction of a planar shock and the successive reshocks with a 3D sinusoidal premixed flame. The reacting NS equations were solved with a 9th-order WENO scheme, and the reaction was

modeled by a 1-step mechanism. The interaction process was categorized into two stages based on the shock reflection:

- After the interaction with incident shock, the flame front developed into a “cap-spike-bubble” structure attached by rib and vortex roll structures. The mixing arising from flame distortion was mainly attributed to the large-scale spanwise vortex.
- After the interaction with reflected shocks, the flame fronts were gradually wrinkled and broken up.

Chen et al. [111] evaluated the chemical reaction and mixing characteristic time scale and found they behaved oppositely under successive reshocks: the chemical reaction rate gradually increased, and the mixing rate gradually decreased.

Bambauer et al. [124] also numerically studied the 3D reactive RMI using the SENGAsolver and investigated the effect of chemical reaction, shock strength, and initial flame perturbation on the flame surface area and mixing width. Because the combustion wave suppressed the wrinkled structure on the flame, the flame area in the reacting case was only 50% compared with the non-reactive one. After each reshocks, the flame thickness reduced about 50% due to flame compression and pressure increasing.

A non-premixed reactive study was reported by Attal and Ramaprabhu [104]. This study emphasized the different thicknesses of the initial interface separating fuel or oxidizer. For large thickness, a portion of the interface was diffusively filled by premixture and could be ignited under high temperature. This simulation was performed by solving NS equations using an extended chemical reacting FLASH solver. The oxidizer was at a high temperature, and the diffusive interface could be ignited without the help of shock. In this case, the combustion wave would perturb the interface and generate RM- or RT-like instability structures that could be explained by finite-thickness impulsive theory.

Yang et al. [98] performed both experimental and numerical studies on the RMI-induced mixing enhancement in a scramjet engine with a central strut. The RMI was induced by transverse high-temperature jets on the combustor wall. The numerical study was performed using FLUENT and produced agreeable results with the ground experiment. Numerical results indicated that the mixing efficiency increased by about 43%.

Apart from the simple RMI interface, lots of studies aiming for shock-flame interactions can also be regarded as reactive RMI. The flame surface is either multimode corrugated resulting from long hot-wire ignition[23] or in spherical or hemisphere shape as the result of point spark ignition [48, 50, 71, 76, 123].

A simplified numerical model is an interaction between a planar shock and a cylindrical flame. Picone et al. [14] additionally reduced the numerical modeling of the flame as fully burnt gas without chemical reaction. This

investigation suggested that the vorticity estimated by the nonlinear theory was consistent with this numerical result. The complex shock system induces extra flame distortion. Ju et al. [31] studied the impact of incident shock strength on the flame distortion by quantitative evaluation of the flame properties, including length of flame front and mass burning rate.

The SFI experiment by Thomas et al.[50] shown that, detonation wave structure emerged from the flame distortion by the reflective shock wave. Dong et al. [71] numerically reproduced this experiment and suggested that the stagnant state by the reflected shock should not be modeled by the reduced chemical mechanism, and at least the elementary skeletal mechanism was required to describe the shock-induced instability at elevated pressure and temperature.

RSBI

In 2012, Haehn et al. [88] reported an experimental RSBI study. According to Ref.[88], “*the present experimental study is the first of its kind where a spherical bubble is filled with a stoichiometric mixture of H_2 and O_2* ”. The major difference between Ref.[88] and aforementioned SFI studies in Ref.[14, 31, 48, 50, 71, 76, 123] is that, before the shock impact the bubble, initially, the bubble is not ignited yet. Depending on the incident shock strength, the SBI may lead to ignition. Haehn et al. [88] referred to this new class of SBI as the “*reactive shock-bubble interaction*”. This study is described in Section. 1.3.1.

To elucidate the unknown processes in this RSBI experiment, Diegelmann et al. [107, 108, 112] reported a series of numerical works, including both 2D and 3D simulations. The 2D numerical studies [107, 108] successfully predicted two combustion modes but did not faithfully maintain the initial geometric and thermodynamic setup with the experiment. The 3D numerical work [112] mostly followed the experimental setup but only reproduce the experiment partly satisfactorily.

In Ref.[108], the effects of incident Mach strength were investigated using a 2D cylindrical bubble. The reacting NS equations were integrated using WENO-CU6 [101] scheme for inviscid flux evaluation and the 3rd-order Runge-Kutta scheme for temporal advancement, and the combustion was modeled by comprehensive H_2 combustion chemistry with pressure-dependent reactions [60]. Two combustion modes were observed depending on the incident shock strength, and the authors suggested these could be explained by the prevalence of either low-pressure or high-pressure reactions. Even for the detonation cases, different combustion processes were detected: for $M = 2.30$ or higher, the results were direct detonation waves. For $M = 2.19$, the results were DDT. The detonation waves significantly reduced the mixing.

In Ref.[107], numerical studies were performed for various initial pressures with a cylindrical bubble by keeping $M = 2.30$. Same numerical methods as Ref.[108] were adopted. The deflagration wave was detected at the lowest initial pressure, and by increasing the initial pressure, a detonation wave was predicted. Both combustion types significantly reduced the mixing.

In Ref.[112], a 3D numerical study was conducted by maintaining the most experimental setup. The shock wave ignited the bubble before the shock-focusing point. A comparison with 2D results revealed the three-dimensional effect had a large impact on the late-stage bubble evolution. Though the ignition delay time, reactive wave speed in this study matched well with the experiment, the huge difference of the transverse bubble case caused by combustion in the experiment, was poorly predicted.

Apart from the experiment by Haehn et al. [88] and related numerical works, Billet et al.[70] also reported a numerical study of RSBI for the non-premixed combustion case. The bubble was filled by H_2 while the surround gases are air. To successfully get ignition, the pre-shock state was set at a high temperature (1000 K). The goal of this study was to evaluate the importance of volume viscosity and results shown that the pressure gradients and vorticity production were influenced by the volume viscosity. The vortex structures of ISBI were also modified by considering volume viscosity.

2.4 AMR methods

The AMR method is extremely suitable for problems with considerably different scales. To simulation the DDT process from the first principle, the numerical methods shall be able to handle the interest scales from the system to the flame thickness. Oran and Gamezo [65] estimated this range could be up to 12 orders of magnitude, and they and their colleagues developed several AMR methods [33, 48, 66] aim at DDT simulations. The astrophysical simulation meets the same obstacle. In the astrophysical community, the open-source AMR software, FLASH [41], has been extensively applied in research and has gotten more than 2000 citations until Sept 2021. The AMR method can be applied to both FVM, FEM, or FDM. Compared with the simply statistic Cartesian or curvilinear grids that are widely used for teaching or researching purpose, the AMR grids show great advantages in flexibility and lightness but is weak at cell addressing and constructing high-order schemes. Most AMR methods utilize lower schemes (such as 2nd -order MUSCL) to reduce the addressing loads and increase the grid resolutions for higher precision. As the AMR method focuses on the abstracted data structures concerning the fundamental grid level, researchers refer to it as the *framework*.

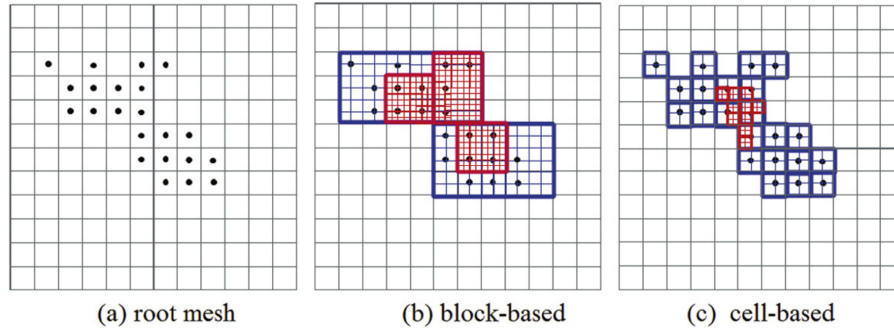


Figure 2-3. Schematic sketch of block-based AMR and cell-based AMR methods [105].

Figure 2-3 presents the typical grids generated by two different AMR data structures. The block-based AMR methods were proposed in Berger and Olinger [15] and later improved in Berger and Rigoutsos [21], and are extensively implemented in SAMRAI [45], AMROC [127], PARAMESH [42], and FLASH [41]. The cell-based AMR method was firstly proposed by Khokhlov [33]. Figure 2-3 (a) illustrates the root-level grids with the marked cells required for refinement.

Figure 2-3 (b) demonstrates two-level of refinement using the block-based AMR methods: the marked cells are covered by a logically Cartesian grid of which the 1st-level is colored by blue, and the 2nd-level refined cells are colored by red. As the governing equations on each patch of the refined domain can be integrated by calling the same algorithms designed for structured grids, it is easy to transplant an in-house code to block-based AMR methods. Difficulties lie in the parallel computation: all patches use ghost cells to build stencils for boundary cells, and this causes severe memory overhead and traffic of parallel communication.

Figure 2-3 (a) presents the schematic 2-level data structures in the cell-based AMR method: only the cells with markers are refined. Compared with the block-based AMR, the cell-based type is more flexible and produces much less excessive grids; the memory overhead is hugely alleviated. The main shortcoming of this type is the construction of large stencils for explicitly high-order schemes such as WENO [97]. In addition, the data structures in cell-based AMR are far from the classically structured grid, which induces more difficulties in the coding process than the block-based type. Nevertheless, because of the higher efficiency, the cell-based AMR method is used in this thesis.

The dynamic load balancing shall be satisfied when applying the AMR method in parallel computations. The scalability, which is proposed by computer scientists for High-performance Computation, evaluates whether the computational speed grows linearly versus the growth of computational nodes. The dynamic load balancing is genuinely required by parallel AMR computations and can help to get high scalability. As the grids are only locally refined in the interested region, if the newly refined grids are still stored on the local node, soon, the storage

of the node with the most refinement will outrate those with the least refinement. Practically, without dynamic load balancing in a 2D simulation, the largest ratio of cell numbers between parallel nodes can be as large as 100. In this case, the parallel computation will be limited by the heaviest node while the light nodes will be idle, which causes severely low scalability. The space-filling curve (SFC), which is a well-known technique for improving the efficiency of computational graphic efficiency, can also be applied to designing high-efficient algorithms for PDE solving. The SFC has been utilized in many modern AMR frameworks for high scalability, including ParMETIS [128], PETSc/Tao [129], and GAMER-2 [115].

3. Numerical model

3.1 Governing equations

The compressible reactive multi-component Navier-Stokes equations are used to model the reactive compressible flows in this work. In a two-dimensional Cartesian coordinate system, the governing equations with n_s species can be written as

$$\frac{\partial \mathbf{U}}{\partial t} + \frac{\partial \mathbf{F}}{\partial x} + \frac{1}{r} \frac{\partial (r\mathbf{G})}{\partial y} = \frac{\partial \mathbf{F}_v}{\partial x} + \frac{1}{r} \frac{\partial (r\mathbf{G}_v)}{\partial y} + \mathbf{S}_c + \Psi_a \mathbf{S}_a \quad (3.1)$$

where \mathbf{U} is the conservative variable vector,

$$\mathbf{U} = [\rho_1, \dots, \rho_{n_s}, \rho u, \rho v, E]^T \quad (3.2)$$

and \mathbf{F} and \mathbf{G} are the inviscid fluxes, which are given by

$$\mathbf{F} = [\rho_1 u, \dots, \rho_{n_s} u, \rho u^2 + p, \rho uv, (E + p)u]^T \quad (3.3)$$

$$\mathbf{G} = [\rho_1 v, \dots, \rho_{n_s} v, \rho uv, \rho v^2 + p, (E + p)v]^T \quad (3.4)$$

The viscous fluxes \mathbf{F}_v and \mathbf{G}_v are expressed in the following forms:

$$\mathbf{F}_v = \left[-J_{1,x}, \dots, -J_{n_s,x}, \tau_{xx}, \tau_{xy}, u\tau_{xx} + v\tau_{xy} - q_x - \sum_{i=1}^{n_s} J_{i,x} h_i \right]^T \quad (3.5)$$

$$\mathbf{G}_v = \left[-J_{1,y}, \dots, -J_{n_s,y}, \tau_{xy}, \tau_{yy}, u\tau_{xy} + v\tau_{yy} - q_y - \sum_{i=1}^{n_s} J_{i,y} h_i \right]^T \quad (3.6)$$

\mathbf{S}_c and \mathbf{S}_a are the source terms that arise from the chemical reactions and the assumption of axisymmetric flow, respectively. They are defined as

$$\mathbf{S}_c = [\dot{\omega}_1, \dots, \dot{\omega}_{n_s}, 0, 0, 0]^T \quad (3.7)$$

$$\mathbf{S}_a = [0, \dots, 0, 0, p - \frac{2\mu v}{y} - \frac{2}{3}\mu(\frac{\partial u}{\partial x} + \frac{\partial v}{\partial y} + \frac{v}{y}), 0]^T \quad (3.8)$$

In these expressions, ρ_i ($i = 1 - n_s$) is the species density; ρ is the total density of the mixture; u and v are the bulk velocity components; p is the pressure; E is the total energy per unit volume of the mixture; $J_{i,x}$ and $J_{i,y}$ are the species diffusion terms in the x and y directions, respectively; τ_{ij} are the viscous stress components; q_x and q_y are the heat conduction terms in the x and y directions, respectively; h_i is the species enthalpy; $\dot{\omega}_i$ is the chemical

mass production term of each species; μ is the viscosity of the mixture. For the two-dimensional planar flow $r = 1$ and $\Psi_a = 0$, while for the axisymmetric flow $r = y$ and $\Psi_a = 1$.

The diffusion terms of species i are defined as

$$J_{i,x} = -\rho \left(D_i \frac{\partial Y_s}{\partial x} - Y_i \sum_{m=1}^{n_s} D_m \frac{\partial Y_m}{\partial x} \right) \quad (3.9)$$

$$J_{i,y} = -\rho \left(D_i \frac{\partial Y_s}{\partial y} - Y_i \sum_{m=1}^{n_s} D_m \frac{\partial Y_m}{\partial y} \right) \quad (3.10)$$

where D_i is the species diffusion coefficient and Y_i is the species mass fraction.

Following Stokes' hypothesis, the bulk viscosity effect is neglected, and the viscous stresses can be written as

$$\tau_{xx} = \frac{2}{3} \mu \left(2 \frac{\partial u}{\partial x} - \frac{\partial v}{\partial y} - \frac{\Psi_a v}{y} \right) \quad (3.11)$$

$$\tau_{yy} = \frac{2}{3} \mu \left(2 \frac{\partial v}{\partial y} - \frac{\partial u}{\partial x} - \frac{\Psi_a v}{y} \right) \quad (3.12)$$

$$\tau_{xy} = \tau_{yx} = \mu \left(\frac{\partial u}{\partial y} + \frac{\partial v}{\partial x} \right) \quad (3.13)$$

The thermal conduction term is modeled according to the Fourier law,

$$q_x = -\kappa \frac{\partial T}{\partial x} \quad (3.14)$$

$$q_y = -\kappa \frac{\partial T}{\partial y} \quad (3.15)$$

where κ is the thermal conductivity of the mixture.

3.1.1 Thermodynamic model

The EOS for a chemically reacting mixture composed of thermally perfect gases is given by

$$p = \sum_{i=1}^{n_s} \rho_i \frac{R_u}{MW_i} T \quad (3.16)$$

where R_u is the universal gas constant and MW_i is the species molecular weight.

The total energy per unit volume of the mixture is defined as

$$E = \sum_{i=1}^{n_s} \rho_i \left(h_i - \frac{R_u}{MW_i} T \right) + \frac{1}{2} \rho (u^2 + v^2) \quad (3.17)$$

where the species enthalpy is evaluated from curve fits of the form

$$\frac{h_i(T)}{R_i T} = -a_{i,1} T^{-2} + a_{i,2} \frac{\ln T}{T} + a_{i,3} + a_{i,4} \frac{T}{2} + a_{i,5} \frac{T^2}{3} + a_{i,6} \frac{T^3}{4} + a_{i,7} \frac{T^4}{5} + \frac{b_{i,1}}{T} \quad (3.18)$$

The species isobaric heat capacity $C_{p,i}$ and entropy S_i are evaluated similarly. The coefficients $a_{i,k}$ and $b_{i,l}$ are obtained from the NASA thermochemical polynomial data [51].

3.1.2 Transport properties

The transport properties of the mixture are calculated using Wilke's mixing rule:

$$\mu = \sum_{i=1}^{n_s} \frac{X_i}{\phi_i} \mu_i \quad (3.19)$$

$$\kappa = \sum_{i=1}^{n_s} \frac{X_i}{\phi_i} \kappa_i \quad (3.20)$$

where X_i is the species molar fraction, and the term ϕ_i is defined as

$$\phi_i = \sum_{m=1}^{n_s} \frac{X_m \left\{ 1 + \sqrt{\frac{\mu_i}{\mu_m} \left(\frac{MW_m}{MW_i} \right)^{1/4}} \right\}^2}{\sqrt{8 \left(1 + \frac{MW_i}{MW_m} \right)}} \quad (3.21)$$

The viscous coefficient μ_i of each species is calculated using the Chapman-Enskog model [20]

$$\mu_i = 2.6693 \cdot 10^{-6} \frac{\sqrt{MW_i T}}{\Omega_{\mu,i} \sigma_i^2} \quad (3.22)$$

where σ_i is the molecular collision diameter, and the collision integral for viscosity is defined as in Ref. [9]

$$\Omega_{\mu,i} = A(T_i^*)^B + C \exp(DT_i^*) + E \exp(FT_i^*) \quad (3.23)$$

The parameters are $A = 1.16145$, $B = -0.14874$, $C = 0.52487$, $D = -0.7732$, $E = 2.16178$, $F = -2.43787$, and $T_i^* = T / (\varepsilon / k)_i$ using the Lennard-Jones energy parameter $(\varepsilon / k)_i$ for the i th specie. Table A-0-11 lists the molecular properties of all species in this study.

The thermal conductivity κ_i of each species is calculated using Eucken's relation [54],

$$\kappa_i = \left(C_{p,i} + \frac{5}{4} \frac{R_u}{MW_i} \right) \cdot \mu_i \quad (3.24)$$

and the diffusivity D_i of each species is modeled as

$$D_i = (1 - X_i) \left(\sum_{m \neq i} \frac{X_m}{D_{im}} \right)^{-1} \quad (3.25)$$

The binary diffusion coefficient is calculated using the constitutive empirical law as

$$D_{ij} = \frac{0.0266}{\Omega_{D,ij}} \frac{T^{3/2}}{p\sqrt{M_{ij}}\sigma_{ij}^2} \quad (3.26)$$

where M_{ij} is the equivalent molecular mass of the binary mixture defined as

$$M_{ij} = \frac{2}{\frac{1}{M_i} + \frac{1}{M_j}} \quad (3.27)$$

σ_{ij} is the averaged collision diameter, which is expressed as

$$\sigma_{ij} = \frac{\sigma_i + \sigma_j}{2} \quad (3.28)$$

and the collision integral for binary diffusion is defined as

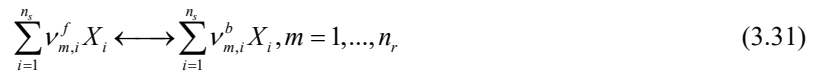
$$\Omega_{D,ij} = A^*(T_{ij}^*)^{B^*} + C^* \exp(D^*T_{ij}^*) + E^* \exp(F^*T_{ij}^*) + G^* \exp(H^*T_{ij}^*) \quad (3.29)$$

where $A^* = 1.06036$, $B^* = -0.1561$, $C^* = 0.19300$, $D^* = -0.47635$, $E^* = 1.03587$, $F^* = -1.52996$, $G^* = 1.76474$, and $H^* = -3.89411$. $T_{ij}^* = T / T_{\varepsilon_{ij}}$, in which $T_{\varepsilon_{ij}}$ is defined using the Lennard-Jones energy parameter [7]

$$T_{\varepsilon_{ij}} = \sqrt{\left(\frac{\varepsilon}{k}\right)_i \left(\frac{\varepsilon}{k}\right)_j} \quad (3.30)$$

3.1.3 Chemical model

The detailed chemical mechanisms are implemented in this work. The general formula for a chemical mechanism with n_r elementary reactions can be expressed as



where $\nu_{m,i}^f$ and $\nu_{m,i}^b$ are the stoichiometric coefficients of the reactants and products of each reaction. The net mass production rate for each species is calculated as

$$\omega_i = MW_i \sum_{m=1}^{n_r} (\nu_{m,i}^b - \nu_{m,i}^f) \left[k_{f,m} \prod_{j=1}^{n_s} \left(\frac{\rho_j}{MW_j} \right)^{\nu_{m,j}^f} - k_{b,m} \prod_{j=1}^{n_s} \left(\frac{\rho_j}{MW_j} \right)^{\nu_{m,j}^b} \right] \quad (3.32)$$

where $k_{f,m}$ and $k_{b,m}$ are forward and backward reaction rate constants, respectively, and are given by

$$k_{f,m} = A_{f,m} T^{B_{f,m}} \exp\left(-\frac{E_{f,m}}{R_u T}\right) \quad (3.33)$$

$$k_{b,m} = \frac{k_{f,m}}{K_{c,m}} \quad (3.34)$$

where $A_{f,m}$ is the pre-exponential factor, $B_{f,m}$ is the temperature exponential factor, and $E_{f,m}$ is the activation energy. $K_{c,m}$ is the equilibrium constant of each reaction, which is expressed as

$$K_{c,m} = \exp\left(-\frac{\Delta G_m^0}{R_u T}\right) \left(\frac{R_u T}{p_{\text{atm}}}\right)^{\sum_i (v_{r,i}^f - v_{r,i}^b)} \quad (3.35)$$

where ΔG_m^0 is the change of Gibbs free energy and $p_{\text{atm}} = 1$ atm.

3.2 AMR methods

The AMR method has huge strengths for problems with vastly separated scales. Thus, it has strong potential to solve detonation problems from the first principle owing to its locally high resolution. In this thesis, I implement a recent open-source cell-based AMR framework, ECOGEN, to construct the finite-volume scheme on compressible reactive flow. This young framework is mainly written in C++ and is easy to extend. It supports dynamic load balancing in parallel computation and has no dependence on other AMR frameworks. Although there are many AMR methods suitable for DDT simulation, this novel AMR framework is a strong competitor, especially on multi-dimensional, multi-component computational fluid dynamic (CFD) problems. In this section, I briefly review this novel AMR framework and describe the procedures and numerical schemes in solving the governing equations. For more information and latest updates of ECOGEN, please refer to Ref.[120][125] and its official website [130].

3.2.1 AMR data structure in ECOGEN

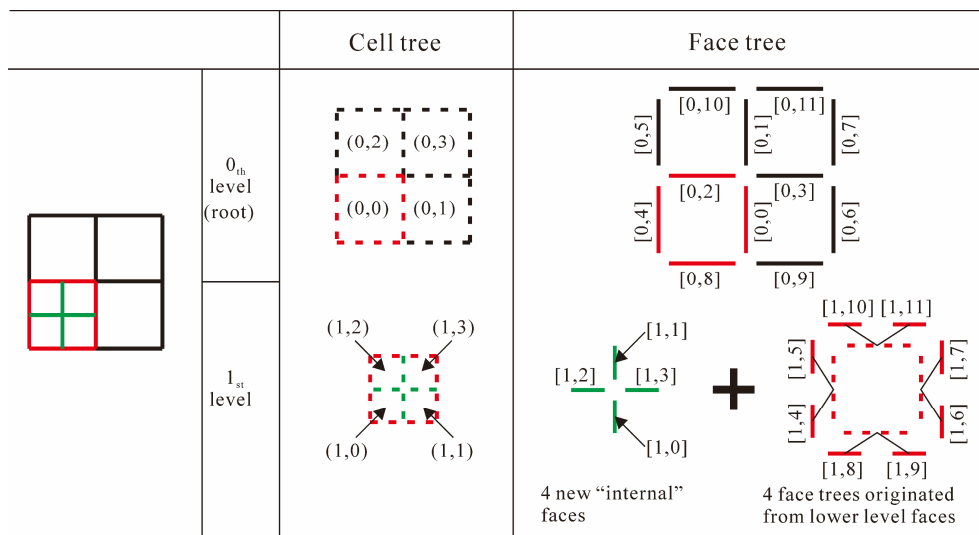


Figure 3-1. A schematic picture for a 2-dimensional Cartesian dual-tree AMR example in ECOGEN with 2-level grids.

The AMR method in ECOGEN implements a dual-tree data structure. This dual-tree structure consists of a cell-tree data structure and a face-tree data structure, both of them are similar to the classical fully threaded tree (FTT) data structure [33]. The strength of this new method is mostly attributed to the extra face-tree data structure: with acceptable memory overhead, the face tree provides straightforward grid connectivity essential for flux evaluation and high-order interpolation. Thus, the dual-tree AMR method considerably alleviates the efforts of accessing neighboring neighbors. For smooth grid transition, the level difference of two neighboring cells never exceeds one. All cells and faces are represented by nodes in the dual-tree, and each node contains the geometric and hydrodynamic information during simulation. To be more specific, if translating into the programming language, each node holds the pointers to memory blocks of metadata which include the geometric properties of cell elements and face elements, the primitive and conservative variables in governing equations, the temporary buffer array when estimating face fluxes or averaging fine cell values, and an AMR indicator for grid refinement.

For computational efficiency and implementation of SFC, all computational nodes on the same refinement level are reconstructed into a one-dimensional array, no matter the flow field is 1D, 2D, or 3D. Each cell or face node is represented by either branch (can be split) or leaf (cannot be split) in the dual-tree. For a clear illustration of the data structure, a simple 2D quad-tree example with 2-level refinement is shown in Figure 3-1, alerted readers can easily extend it into a higher-dimensional case. In the two-dimensional case, a cell node is indexed with the following information:

- (lv, i) – two indices in round brackets, which represent this cell is the i^{th} one on the lv^{th} level.
- $Split$ – a Boolean value that indicates whether the cell shall get further refined or not. This value equals 1 for branched nodes and 0 for leaf-wise nodes.
- $PrC(j)$ – 4 pointers to all child cell nodes, $j = 0, 1, 2, 3$.
- $PriF(j)$ – 4 pointers to all internal child face nodes, $j = 0, 1, 2, 3$.

and a face is indexed as

- (lv, k) – two indices in square brackets, which represent this face is the k^{th} one on the lv^{th} level.
- $PrF(k, n)$ – 2 pointers to all child face nodes, $n = 0, 1$.
- $PrnC(k, m)$ – 2 pointers to the “left” and “right” cell nodes, $m = l$ or r .

In Figure 3-1, cells and faces on the 0^{th} (root) level are colored in black, while the ones on the 1^{st} level are colored either in red or green. On the root level, there exist 4 cells targeted as $(0, j)(j = 0 - 3)$ and 12 faces targeted as $[0, k](k = 0 - 11)$. Only cell $(0, 0)$ is refined to a higher level, which means its $Split$ flag equals to *TRUE*, and it produces 4 child cells $(1, j)(j = 0 - 3)$ on the 1^{st} level, along with 4 “internal” child faces $[1, k](k = 0 - 3)$ inside it

and 8 child faces $[1,k](k = 4 - 11)$ bifurcated from its surrounding faces. Caution must be taken on 4 “internal” child faces during the refinement. The inheritances in cell tree and face tree are intertwining: the parent of faces $[1,8]$ and $[1,9]$ is the face $[0,8]$, while the parent of faces $[1,k](k = 0 - 3)$ is the cell $(0,0)$. Comparing with the classical FTT method, the child nodes in the dual-tree depend much less on the parent nodes except for initialization. This specificity purely lies in the direct access of face nodes to the “left” and “right” cell nodes, e.g., the face $[0,3]$ holds pointers to cell $(0,1)$ and cell $(0,3)$. These pointers replace the cumbersome access in the FTT method and can be easily extended to unstructured non-Cartesian grids. That is why I want to enlist them in the face nodes for emphasis. The case for the faces linking cells on different levels, e.g., the face $[1,6]$ with cell $(1,1)$ and cell $(0,1)$ is a bit different, and I will cover it later.

Cells and faces on different levels are reordered into the one-dimensional cell-/face-data structures, respectively. As mentioned above, every node in the dual-tree holds metadata with some amount of memory. If all the metadata are stored in the dual-tree, the data structure will cause considerable memory overload. An efficient way is to transfer only the pointer of the metadata when adding a node to the dual-tree and unbinding it when removing the node.

Table 3-1. Memory usage comparison between classical FTT AMR and dual-tree AMR methods on two types of governing equations. For the sake of clarity, only the variables in governing equations are considered.

	Data type	Classical FTT AMR	Dual-tree AMR	Ratio
	Words per cell [120]	17	43	<0.4
1D Euler Equations	Conservative variables	3		
	sum	20	46	0.43
Compressible 10-component Navier-Stokes Equations	Conservative variables	10+3+1=14		
	Diffusive coefficients	10+1+1=12		
	sum	43	69	0.62

Table 3-1 presents the memory usage of two AMR methods accounting for different governing equations. In the cell-based AMR methods, the size of words per cell evaluates the averaged memory required to store the numerical information, and it is a good evaluation of memory overhead. As Schmidmayer et al. [120] pointed out that for a given 3D hexahedron cell, the classical FTT methods required only 17 words per cell, while the size of this dual-tree AMR method was 43. Though the ratio between the FTT and this method (< 0.4) is low at first glance, it will substantially increase once the memory cost of the flow variables and high-order schemes are considered. For the 1D Euler equations at first order, at least three additional words are introduced to store flow

variables, which will increase the ratio to 0.43. For the governing equations in Chapter 2, each species and transport mechanism will add at least one variable, and if the gas mixture is modeled as 10 components as presented in later chapters, we can readily achieve a ratio larger than 0.6. The proportion will even be more prominent for the higher-order scheme with buffer memory cost concerning interpolation. Thus, the performance of this young AMR method is promising, especially for multi-component, multi-dimensional problems.

3.2.2 Advancing procedure

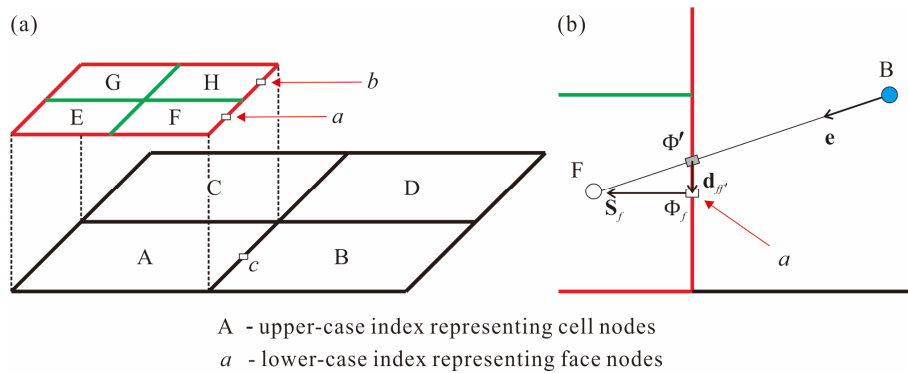


Figure 3-2 A 2D Cartesian dual-tree AMR grid with 2-level refinement, for clarity, only the interested cell nodes and face nodes are marked.

The AMR method in ECOGEN is a finite volume method (FVM). Taking a general form of the governing equation as an example,

$$\frac{\partial \mathbf{U}}{\partial t} + \nabla \cdot (\overline{\mathbf{F}}(\mathbf{U}) - \overline{\mathbf{F}}_v(\mathbf{U})) = \mathbf{S} \quad (3.36)$$

with \mathbf{U} as the vector of conservative variables, $\overline{\mathbf{F}}(\mathbf{U})$ and $\overline{\mathbf{F}}_v(\mathbf{U})$ as inviscid and viscous flux tensors, respectively, and \mathbf{S} is the source terms vector. When integrating the governing equations in the FVM method, by using the Gauss theorem and 1st-order Euler scheme for temporal advancement, for i^{th} cell on l^{th} level, the semi-discretized governing equation is expressed as

$$\mathbf{U}_i^{n+1} = \mathbf{U}_i^n + (\Delta t)_l \left[-\frac{1}{V_i^n} \sum_{s=1}^N A_s^n (\overline{\mathbf{F}}_s^n - \overline{\mathbf{F}}_{v,s}^n) \cdot \mathbf{n}_s + \mathbf{S}_i^n \right] \quad (3.37)$$

The superscript n and $n+1$ represent the variables that are either of the old or the updated step. The \mathbf{U}_i^{n+1} and \mathbf{U}_i^n are the conservative variable vector of i^{th} cells at $(n+1)^{\text{th}}$ and n^{th} step, respectively, and $(\Delta t)_l$ is the time step at the l^{th} level. V_i^n represents the volume of i^{th} cell, and A_s^n represents the area of s^{th} interface at n^{th} step. The subscript s indicates that the flux tensors are evaluated at the s^{th} interface using the “left” and “right” cell values.

On each refined level, Eq. (3.37) is advanced in time with a different time step $(\Delta t)_l$ related to the current level.

A global time step is calculated from the CFL condition by iterating cells through all levels:

$$\Delta t_0 = cfl \times 2^L \frac{\min(dx_L, dy_L)}{\max(|u+a|, |u-a|)} \quad (3.38)$$

where dx_L and dy_L are the grid sizes at the L^{th} level, c is the local sound speed, and the cfl number equals 0.3 – 0.6 in this thesis. As the grid size is halved when refined to the higher level, the time step on the q^{th} level is $(\Delta t)_q = 2^{-q} \Delta t_0$.

The time advancement of the dual-tree is performed in a pyramid manner. On each level, the unsplit cells, which are leaf nodes in the cell tree, are updated by advancing Eq. (3.37), while the splittable cells are updated by averaging their child cells on a higher level. For each step of advancement on the q^{th} level, the cells on the $(q+1)^{\text{th}}$ level advance for 2 time steps; thus, cells on different levels reach the same physical time. Figure 3-2 (a) illustrates a 2D AMR grid with 2-level refinement. For clarity, only the interested cells and faces are marked in a simple way other than that in Figure 3-1. Cells A to D are on the root level, and cells E to H are the children of cell A and belong to the 1st level. All the cells except cell A are leaf (unsplit) nodes, while cell A is a branch (split) node. During a single step of temporal advancement in global time step $(\Delta t)_0$

1. First, the integration of cells occurs on the higher level. Eq. (3.37) is called by cells E to H on 1st level for 2 times with the same time step $(\Delta t)_1 = (\Delta t)_0/2$, this process is not different from the traditional FVM method, and numerical details will be covered in Sec 3.3.
2. After the higher-level advancement ends, the lower-level advancement begins. In the beginning, the split cell A is updated by averaging the conservative variables by its children cells, namely cells E to H. Then, the primitive variables of cell A are renovated by the latest conservative variables, and the unsplit cells B to D are updated by calling Eq. (3.37). The integration of cell D is also similar to the normal FVM method, but for cells B and C, cautions must be taken when the neighboring cells belong to different levels.

The evaluation of the west flux in cell B will be described to clarify this special case. Cell B is connected to cell A via face c on the root level, and it is also connected to cells F and H via face a and b on the 1st level, respectively. Although the west fluxes can be evaluated on either face c or a combination of faces a and b , as the fluxes on face a and b are already calculated when updating cell F and cell H on the 1st level, it is wise to choose the higher-level faces to maintain the conservativity and also reduce computational load. Besides, as both grid size and time step are smaller on the higher level, this choice provides higher-precision flux. In the current AMR method, whenever the fluxes are evaluated on higher-level faces like face a , they are added or subtracted from

either neighboring cell simultaneously. Moreover, according to Eq. (3.37), if the fluxes on the face a is denoted by $(flux)_a$, then its contribution to cell B can be expressed as

$$\frac{A_a^n}{V_B^n} (flux)_a \quad (3.39)$$

and the contribution to cell F is opposite and written as

$$-\frac{A_a^n}{V_F^n} (flux)_a \quad (3.40)$$

where A_a^n represents the area of face a , and V_B^n and V_F^n represent the volume of cells B and F, respectively. For the 2D example in Figure 3-2, as $V_B^n = 4V_F^n$, the contribution of $(flux)_a$ to cell B is a quarter of the one to cell F.

Table 3-2. The granularity for both the 2D AMR and 2D uniform grid

Grid type	Level number	Cells on each level	Unsplit cells on each level updated by Eq. (3.37)	Frequency of calling Eq. (3.37) in every cell	Frequency of calling Eq. (3.37) on each level	Total amount of cells	Total frequency of calling Eq. (3.37) when advancing single Δt_0
AMR	0	N	$\frac{N}{2}$	2^0	$\frac{N}{2} \cdot 2^0$	$N(2^{L+1} - 1)$	$N\left(\frac{7}{6} \cdot 4^L - \frac{1}{6}\right)$
	1	$\frac{N}{2} \cdot (2^2)^1$	$\frac{N}{2^2} \cdot (2^2)^1$	2^1	$\frac{N}{2^2} \cdot (2^2)^1 \cdot 2^1$		
	2	$\frac{N}{2^2} \cdot (2^2)^2$	$\frac{N}{2^3} \cdot (2^2)^2$	2^2	$\frac{N}{2^3} \cdot (2^2)^2 \cdot 2^2$		
	⋮	⋮	⋮	⋮	⋮		
	$L - 1$	$\frac{N}{2^{L-1}} \cdot (2^2)^{L-1}$	$\frac{N}{2^L} \cdot (2^2)^{L-1}$	2^{L-1}	$\frac{N}{2^L} \cdot (2^2)^{L-1} \cdot 2^{L-1}$		
	L	$\frac{N}{2^L} \cdot (2^2)^L$	$\frac{N}{2^L} \cdot (2^2)^L$	2^L	$\frac{N}{2^L} \cdot (2^2)^L \cdot 2^L$		
uniform	0	$N \cdot (2^2)^L$	$N \cdot (2^2)^L$	2^L	$N \cdot (2^2)^L \cdot 2^L$	$N \cdot 4^L$	$N \cdot 8^L$
AMR/uniform value			L		$2^{1-L} - 4^{-L}$	$\frac{7}{6} \cdot 2^{-L} - \frac{1}{6} \cdot 8^{-L}$	
			$L = 0$		1.00	1.00	
			$L = 1$		0.75	0.56	
			$L = 2$		0.44	0.29	
			$L = 3$		0.23	0.15	
			$L = 4$		0.12	0.07	
$L = 5$		0.06	0.04				

The specific time-marching methods along with the grid refinements are critical to the efficiency of the AMR method. As Eq. (3.37) is called whenever updating all cells on any level, the granularity of temporal advancement in a single global time step Δt_0 can be roughly evaluated by counting the frequency of calling this equation. The

storage and complexity are shown in Table 3-2 to compare the performance on AMR grids and traditionally uniform grids. Here, I choose 2-dimensional cases as the example, and the minimum grid size of the uniform grids equals the smallest grid size in the AMR one. For simplicity, let us assume that exactly half of the cells on each level, except for the L^{th} level, are refined. If the cell number on the 0^{th} level is N , then the total amount of AMR cells is $(2^{L+1}-1)N$, while for the uniform grid the counterpart is $4^L N$, and the ratio of these two cell numbers is around 2^{L-1} . If we consider the storage of the whole dual tree, as the sizes of face tree nodes and cell tree nodes are of the same magnitude, the memory load of the dual-tree data structure is roughly $(2^{L+2}-2)N$, and a proper evaluation of the ratio is around 2^{L-2} . Note that in the AMR method, except for the highest level, only half the cells on each level are updated by calling Eq. (3.37); others are updated by averaging their children. For $L \geq 2$, the granularity is around $\frac{7}{6}4^L N$ and $8^L N$ for the AMR grid and uniform grid respectively, and the ratio is around $\frac{7}{6}2^{-L}$. For reference, the ratio values for $L = 0 - 5$ are listed, and the efficiency of this AMR method is dramatically high! It is shown that when L increases, the ratio decreases, which means the computational load decreases and the AMR method gets to be more efficient. The computational load of AMR is about half of the uniform one when $L = 1$. For the applications in the present thesis, when $L = 3$, the ratio is 0.15, and when $L = 5$, the ratio is less than 0.05. If we consider the 3D case other than 2D but keep other assumptions, for $L = 2 - 5$, the ratio of complexity is around 0.27 - 0.03.

3.2.3 Grid Refinement Process

The grid refinement is controlled by a refinement indicator $0 \leq \xi \leq 1$ which is evaluated and stored in each cell. On the cell-tree structure, each cell is targeted as either the split cell or the leaf cell depending on whether it can be further refined or not. For the leaf cell when $\xi > \xi_{\text{split}}$, the cell must be split; for the split cell when $\xi < \xi_{\text{join}}$, the cell can be joint. To assure smooth grid transition [33, 125], the difference in levels between two neighboring cells must be smaller than 2. The refinement indicator ξ is evaluated in two steps. In the first step, for each computational cell, ξ is determined by the significant gradients:

$$\xi = \begin{cases} 1 & , \text{ when } \frac{|Q_{i,neighbor} - Q_i|}{\min(Q_{i,neighbor}, Q_i)} > \varepsilon \\ 0 & , \text{ otherwise} \end{cases} \quad (3.41)$$

Here, Q represents the physical properties, including the p , ρ , T , velocity magnitude, and mass fraction. In the second step, a diffusive equation governs the smoothing of ξ

$$\frac{\delta \xi}{\delta t} = K \nabla^2 \xi \quad (3.42)$$

where \tilde{t} is a fictive diffusive time step, and $K = 2^{-2l} \max(dx_0, dy_0)^2$ is a diffusive coefficient that assures smooth AMR grid transition. Following Ref. [33, 125], in this study, $\varepsilon = 0.08$, $\xi_{\text{split}} = 0.02$, and $\xi_{\text{join}} = 0.11$.

To further promote computational efficiency in this combustion simulation, a special AMR strategy is designed based on the empirical threshold of the ignition/flame temperature $T_{\text{et}} = 900$ K to refine the hydrodynamic and chemical discontinuities separately:

$$L = \begin{cases} L_{\text{hydro}} \\ L_{\text{chem}} \end{cases}, Q = \begin{cases} p, \rho, T, \sqrt{u^2 + v^2} & , \text{when } T < T_{\text{et}} \\ p, \rho, T, \sqrt{u^2 + v^2}, Y_{OH} & , \text{when } T \geq T_{\text{et}} \end{cases} \quad (3.43)$$

Here, L_{hydro} and L_{chem} represent the highest refined levels for hydrodynamic and chemical discontinuities, respectively, and L_{hydro} is always smaller than L_{chem} .

3.3 Numerical methods other than AMR

The advancement of Eq. (3.37) on each level is performed in a face-by-face manner. By iterating over the leaf face nodes on the current level, both the inviscid and viscous fluxes are evaluated and added to the “left” and “right” cells. In this thesis, I encounter two types of source terms, one arises from the simplification of axisymmetric flow, and the other is caused by chemical reactions. In this section, the numerical schemes adopted to model these terms are described.

3.3.1 Inviscid fluxes

The inviscid fluxes are estimated using a Godunov-type method when solving the Riemann problems between the cell variables on both sides of the face. The multi-component Harten-Lax-van Leer Contact (HLLC) solver [74] is implemented to evaluate the inviscid flux, and the MUSCL scheme [12] with Van Leer limiter [10] is used to gain a 2nd-order precision interpolation.

3.3.2 Viscous fluxes

To evaluate the diffusion terms of a quantity ϕ , the values of ϕ on the faces are interpolated using a 2nd-order central scheme. Although I only use the rectangular Cartesian grid in the current thesis, the neighboring cells of different levels cause extra skewness. An example is shown in Figure 3-2 (b) as the neighboring cells B and F and the inter-cell face a. This skewness is corrected using a popular method which can be found in Ref. [113]: first, the linear interpolation profile is applied to estimate the value of ϕ' at the intersection a' between the cell interface and the line connecting the two neighboring cell centers, then the derivative of ϕ is used to interpolate the ϕ_a at the face centroid.

$$\phi_a = \phi_{a'} + (\nabla \phi)_{a'} \cdot \mathbf{d}_{aa'} \quad (3.44)$$

3.3.3 Axisymmetric source terms

The axisymmetric assumption is widely used to reduce the computational load in CFD studies. In this thesis, this simplification is applied to model the spherical SBI problem. Nevertheless, to keep some basic physical principles in the FVM method, such as mass conservation, the implementation of this assumption must be carefully handled when dealing with the axisymmetric source terms. If the coordinates z and r of the cylindrical coordinate system are replaced by x and y , the governing equation can be written in the Cartesian coordinate system with extra terms originated from coordinate transformation. Thus, both planar and axisymmetric flows get modeled by Eq. (3.1) with a flag ψ_a for axisymmetric terms \mathbf{S}_a . In the area of FVM method, two famous sets of governing equations exist with cells in rectangular or sector implementation.

Rectangular implementation

For the rectangular implementation, the semi-discretized form of Eq. (3.1) is written as

$$\frac{\partial}{\partial t} \int_{\Omega_{rec}} \mathbf{U} d\Omega_{rec} + \oint_{\partial\Omega_{rec}} (\tilde{\mathbf{F}} - \tilde{\mathbf{F}}_v) dS_{rec} = \int_{\Omega_{rec}} (\mathbf{S}_c + \mathbf{S}_{a,rec}) d\Omega_{rec} \quad (3.45)$$

where $d\Omega_{rec}$ and dS_{rec} stand for the rectangular volume element and surface element. In the Cartesian coordinate system, if the ‘‘depth’’ of the domain is set to 1 and the normal unit vector of the surface element is denoted by $\mathbf{n} = (n_x, n_y)^T$, then we have,

$$\begin{aligned} d\Omega_{rec} &= dx \cdot dy = dx dy \\ dS_{rec} &= n_x dx + n_y dy \end{aligned} \quad (3.46)$$

If the velocity is denoted by $\mathbf{V} = (u_x, u_y)^T$, then the velocity normal to the cell interface is given as $V = \mathbf{V} \cdot \mathbf{n} = u_x n_x + u_y n_y$, and the inviscid flux term $\tilde{\mathbf{F}}$ can be expressed as

$$\tilde{\mathbf{F}} = \begin{bmatrix} \rho V \\ \vdots \\ \rho n_s V \\ \rho u_x V + p n_x \\ \rho u_y V + p n_y \\ (E + p)V \end{bmatrix} \quad (3.47)$$

the viscous flux term $\tilde{\mathbf{F}}_v$ is written as

$$\tilde{\mathbf{F}}_v = \begin{bmatrix} -J_{1,x} n_x - J_{1,y} n_y \\ \vdots \\ -J_{1,n_s} n_x - J_{1,n_s} n_y \\ \tau_{xx} n_x + \tau_{xy} n_y \\ \tau_{xy} n_x + \tau_{yy} n_y \\ \left(u_x \tau_{xx} + u_y \tau_{xy} - q_x - \sum_{i=1}^{n_s} J_{i,x} h_i \right) n_x + \left(u_x \tau_{yx} + u_y \tau_{yy} - q_y - \sum_{i=1}^{n_s} J_{i,y} h_i \right) n_y \end{bmatrix} \quad (3.48)$$

in this scenario, the axisymmetric source term $\mathbf{S}_{a,rec}$ is expressed as

$$\mathbf{S}_{a,rec} = -\frac{1}{y} \tilde{\mathbf{F}}_y + \frac{1}{y} \tilde{\mathbf{F}}_{v,y} = -\frac{1}{y} \begin{bmatrix} \rho_1 u_y \\ \vdots \\ \rho_{n_s} u_y \\ \rho u_x u_y \\ \rho u_y^2 + p \\ (E + p) u_y \end{bmatrix} + \frac{1}{y} \begin{bmatrix} -J_{1,y} \\ \vdots \\ -J_{n_s,y} \\ \tau_{xy} \\ \tau_{yy} - \frac{2}{3} \mu \left(\frac{\partial u}{\partial y} + \frac{\partial v}{\partial x} + 2 \frac{v}{y} \right) \\ u_y \tau_{yx} + u_y \tau_{yy} - q_y - \sum_{i=1}^{n_s} J_{i,y} h_i \end{bmatrix} \quad (3.49)$$

Sector implementation

For the rectangular implementation, let $r = y$, Eq. (3.1) can be rearranged to

$$\frac{\partial(y\mathbf{U})}{\partial t} + \frac{\partial(y\mathbf{F})}{\partial x} + \frac{\partial(y\mathbf{G})}{\partial y} = \frac{\partial(y\mathbf{F}_v)}{\partial x} + \frac{\partial(y\mathbf{G}_v)}{\partial y} + y\mathbf{S}_c + y\mathbf{S}_{a,sec} \quad (3.50)$$

For volume element in sector shape, the semi-integrated form of Eq. (3.50) is written as

$$\frac{\partial}{\partial t} \int_{\Omega_{sec}} (y\mathbf{U}) d\Omega_{sec} + \oint_{\partial\Omega_{sec}} [y(\tilde{\mathbf{F}} - \tilde{\mathbf{F}}_v)] dS_{sec} = \int_{\Omega_{sec}} [y(\mathbf{S}_c + \mathbf{S}_{a,sec})] d\Omega_{sec} \quad (3.51)$$

in which

$$\begin{aligned} d\Omega_{sec} &= dx \cdot dy = dx dy \\ dS_{sec} &= n_x dx + n_y dy \end{aligned} \quad (3.52)$$

Eq. (3.51) can be rearranged to

$$\frac{\partial}{\partial t} \int_{\Omega_{sec}} \mathbf{U} d\hat{\Omega}_{sec} + \oint_{\partial\hat{\Omega}_{sec}} (\tilde{\mathbf{F}} - \tilde{\mathbf{F}}_v) d\hat{S}_{sec} = \int_{\Omega_{sec}} (\mathbf{S}_c + \mathbf{S}_{a,sec}) d\hat{\Omega}_{sec} \quad (3.53)$$

in which

$$\begin{aligned} d\hat{\Omega}_{sec} &= y d\Omega_{sec} = y(dx \cdot dy) \\ d\hat{S}_{sec} &= y dS_{sec} = y(n_x dx + n_y dy) \end{aligned} \quad (3.54)$$

The expression of $\tilde{\mathbf{F}}$ and $\tilde{\mathbf{F}}_v$ are the same with the rectangular case, and the axisymmetric source term $\mathbf{S}_{a,sec}$ is expressed in a very simple form,

$$\mathbf{S}_{a,sec} = -\frac{1}{y} \begin{bmatrix} 0 \\ \vdots \\ 0 \\ 0 \\ p - \frac{2}{3}\mu\left(\frac{\partial u}{\partial y} + \frac{\partial v}{\partial x} + 2\frac{v}{y}\right) \\ 0 \end{bmatrix} \quad (3.55)$$

Comparing the discretized equations of these two approaches, the differences mainly lie in the modeling of geometric variables and axisymmetric source terms: the expressions of $d\widehat{\Omega}_{sec}$ and $d\widehat{S}_{sec}$ in Eq. (3.54) is similar to $d\Omega_{rec}$ and dS_{rec} in Eq. (3.46) but require only one excess variable. However, the expression of $\mathbf{S}_{a,sec}$ in Eq. (3.55) is considerably simpler than $\mathbf{S}_{a,rec}$ in Eq. (3.49). Now let us consider the coding implementation of these two approaches if the same 2-dimensional computer program is used to simulate both planar and axisymmetric flow.

In the first approach, the expressions of $d\Omega_{rec}$ and dS_{rec} are the same with that of the planar case, and only one variable will be required to switch on/off the $\mathbf{S}_{a,rec}$. Although Eq. (3.49) seems to be complex, as almost all terms in this equation have already been prepared when modeling $\widetilde{\mathbf{F}}$ and $\widetilde{\mathbf{F}}_v$ according to Equations (3.47) and (3.48), no extra differential operation presents when evaluating $\mathbf{S}_{a,rec}$.

In the second approach, both the geometric variables and axisymmetric terms must be revised from the planar case. One variable shall be added to switch the geometric properties, for example,

$$d\Omega = \begin{cases} dxdy \\ y_{cell}dxdy \end{cases}, dS = \begin{cases} n_x dx + n_y dy \\ y_{face}(n_x dx + n_y dy) \end{cases}, \text{ for planar flow} \quad (3.56)$$

For the AMR method in this thesis, all cells and cell interfaces on every level must be adjusted according to Eq. (3.56), and the value y is gotten either from the cell center (for $d\Omega$) or face center (for dS). This process is challenging, as most of the cell nodes and face nodes are dynamically created during the computational process, and the creating procedures are different for numerous different scenarios. In contrast, the evaluation of the axisymmetric source terms in Eq. (3.55) is much simpler: only the y -momentum equation needs to be modified.

In this work, I adopt the second approach instead of the first one, although comparisons show that the programming implementation of the second approach is more arduous, and the first approach is adopted by many CFD works such as Ref.[56, 99,100], including the original ECOGEN software [120, 125]. The second approach is implemented in this work as it shows better mass conservativity, which is essential for accurate reacting-flow simulations. As we know, in the FVM method, both the inviscid and viscous flux flow in or out into neighboring cells; thus, this method is generically conservative. However, under the axisymmetric assumption, this intrinsic

conservativity gets destroyed by the extra source term $\mathbf{S}_{a,rec}$ or $\mathbf{S}_{a,sec}$. By ignoring the chemical source term \mathbf{S}_c , the spatial integration of the controlling equations will show the destruction of global conservativity. For the rectangular cell setup, the integration of Eq. (3.45) over domain Ω is

$$\frac{\partial}{\partial t} \sum_i \mathbf{U} d\Omega_{rec,i} = \sum_i \mathbf{S}_{a,rec} d\Omega_{rec,i} \quad (3.57)$$

and for the sector cell setup, the integration of Eq. (3.53) is,

$$\frac{\partial}{\partial t} \sum_i \mathbf{U} d\hat{\Omega}_{sec,i} = \sum_i \mathbf{S}_{a,sec} d\hat{\Omega}_{sec,i} \quad (3.58)$$

where both the $d\Omega_{rec,i}$ and $d\hat{\Omega}_{sec,i}$ are or can be derived from the FVM cell of Ω . These two equations present the temporal variation of global conservative variables due to the axisymmetric assumption. From the definition of $\mathbf{S}_{a,rec}$ and $\mathbf{S}_{a,sec}$ in Eqs. (3.49) and (3.55), respectively, it is easy to see that all global conservative properties in Eq. (3.57) change temporally, while in Eq. (3.58) except for the y -momentum, all other global properties are conserved.

In this thesis, without further announcement, the sector cell setup is applied in axisymmetric simulations for more rigorous conservativity. In Section 4.1.5, detailed numerical experiments will be performed to compare the mass conservativity of these two approaches.

3.3.4 Chemical source term

As the ordinary differential equations (ODE) of ignition and detonation processes are highly stiff, the chemical source terms are solved separately from the hydrodynamic terms. The CVODE solver of the SUNDIAL packages implemented in the CANTERA package [116] is used to integrate the stiff ODE with up to 6th-order temporal accuracy.

3.4 Solving procedure

Figure 3-3 demonstrates the schematic procedures of solving reacting flows in the Fire solver. Currently, it is only capable of handling the single-block Cartesian grids when utilizing the AMR method. At the beginning of the simulation, all the initial setups, including the grid, chemical and thermodynamic properties, setup of the schemes, and input/output parameters, are read by the program. The initial flow field will be set from the highest-level cells to the root-level ones. The primary integration processes consist of the integration of the hyperbolic and chemical source terms. After that, the parental cells will be updated by conservative accumulations on child cells. To achieve high accuracy, the integration starts from the highest level and advances reversely.

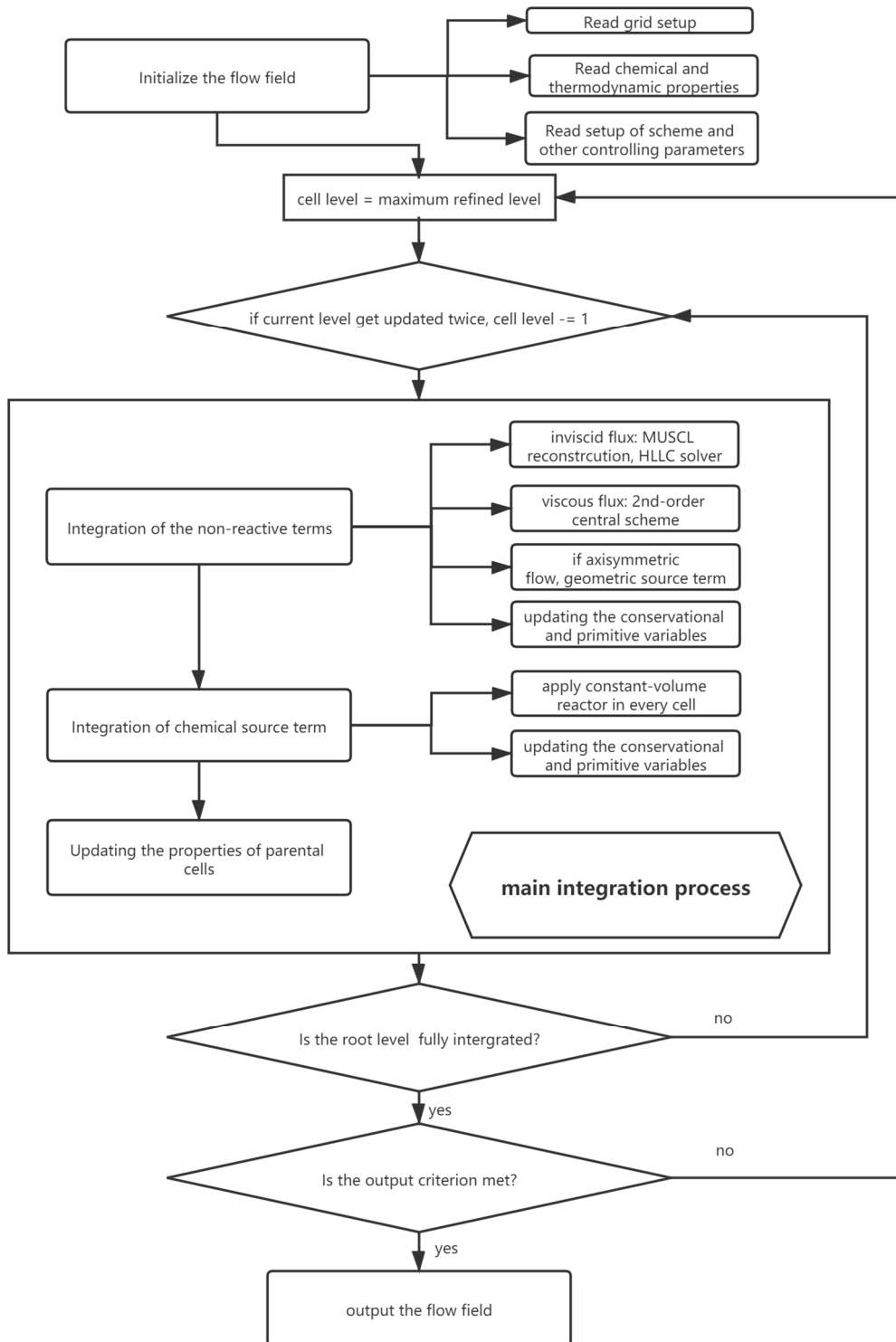


Figure 3-3. The schematic advancing procedures in the Fire solver.

4. Validations of Fire solver

This chapter applies the AMR solver presented in Chapter 3, Fire, to some inert and reacting problems for validation.

The Fire solver was first developed based on the AMR framework in ECOGEN-v1.0 in April 2020 and later transplanted to ECOGEN-v2.0 [130] in May 2020. The open-source project ECOGEN is currently maintained by Dr. Kevin Schmidmayer and aiming at solving compressible flows.

Table 4-1 Comparison of the other solvers in ECOGEN and the Fire solver

	Other solvers in ECOGEN	Novelties of Fire
Purpose	compressible two-fluid flow (shock-droplet interaction)	compressible combustion (detonation)
Reactive or not	inert	chemistry with detailed mechanisms
Mixture type	two-fluid, stiffened gas	multi-component gaseous mixture
Viscous or not	inviscid	viscous
Axisymmetric model	non-conservative	conservative

Table 4-1 compares the other solvers in ECOGEN with the Fire solver: different sets of governing equations, different mixtures and related equations of states and viscosity model, and chemical reactions are implemented in the Fire solver.

To demonstrate the performance of the Fire solver, Table 4-2 lists the testing cases for validation. All cases in this thesis are running using the same sets of numerical schemes without further announcement:

- Temporal integration: 2-step, 2nd-order TVD Runge-Kutta scheme.
- Inviscid flux: reconstructed using the 2nd-order MUSCL scheme and Van Leer limiter, and the face flux is evaluated using an HLLC Riemann solver extended to multi-component mixture.
- Viscous flux: 2nd-order central scheme.
- Chemical: 6th-order back differential method.

Table 4-2. Testing cases for validation of Fire solver

Section	Description	Models for validation
4.1.1	1-D shock propagation	Inviscid model
4.1.2	1-D convection-diffusion of an inert H ₂ /O ₂ front (Billet et al. [58])	Viscous model
4.1.3	2-D ISBI (Niederhaus et al. [68])	Vorticity fields in ISBI problem
4.1.4	2-D axisymmetric ISBI (Zhai et al. [84])	Comprehensive comparison in ISBI problem
4.1.5	2-D axisymmetric ISBI in REC and SEC implementations (Zhai et al. [84])	Conservativity of axisymmetric implementations
4.2.1	0-D ignition delay time	Chemical mechanism
4.2.2	1-D detonation (Paolucci et al. [102])	Detonation with detailed mechanisms
4.2.3	1-D detonation propagation (Lieberman et al. [82])	Detonation with detailed mechanisms
4.3	2-D RSBI (Diegelmann, 2016)	2-D validation of RSBI problem with detailed mechanisms

4.1 Applications on non-reactive flows

4.1.1 1-D shock propagation

A 1D $M = 1.20$ shock propagation in the air is studied here with different maximum refinement levels to demonstrate the efficiency of the current AMR method. Initially, the shock locates at 0.02 m. Figure 4-1 (a) presents the density distribution of different maximum refinement levels at 71 μ s along with the exact solution. The root grids of all these cases are identical with 12 cells uniformly distributed in the 1D domain. When refining the grid to a higher level, the grid size is halved. Thus, the grid size on p^{th} level is $dx_p = dx_0/2^p$.

As the maximum refinement level increases from 0 to 4 in Figure 4-1 (a), the agreements between numerical and analytical results get better. Apart from the AMR grids, a uniform grid with $dx = dx_4$ is also used to for reference. Figure 4-1 (b) compares the results from $L = 4$ AMR grids and uniform grids. The density distributions of these two cases almost overlap and agree well with the analytical solution.

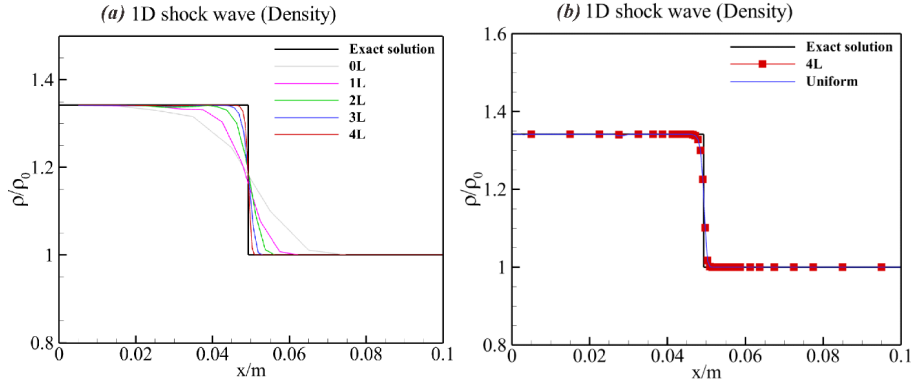


Figure 4-1. The density distribution of a 1D $M = 1.20$ shock wave propagating in air. (a) The results for $L = 0 - 4$ (b) Comparison of results for $L = 4$ AMR grids and uniform grid with $dx = dx_4$.

Table 4-3. The clock time of all cases in Figure 4-1. totalTime: fully clock time, amrTime: clock time of AMR process, uniform: the clock time in the uniform case with $dx = dx_4$. The simulations are performed on the author's laptop.

Case ID	totalTime(s)	amrTime(s)	Grid	$\frac{\text{amrTime}}{\text{totalTime}}$	$\frac{\text{totalTime}}{\text{uniform}}$	$\frac{\text{grid}}{\text{uniform}}$
0L	0.124994	0	12	0.00%	1.94%	6.25%
1L	0.207666	0.000856	19	0.41%	3.22%	9.90%
2L	0.282534	0.001814	25	0.64%	4.38%	13.02%
3L	0.441393	0.003107	30	0.70%	6.84%	15.63%
4L	0.790414	0.011958	37	1.51%	12.25%	19.27%
Uniform	6.45456	0	192	0.00%	100.00%	100.00%

All cases in Figure 4-1 are running serially without parallel communication, which provides an excellent chance to test the AMR efficiency over the traditional FVM method represented by the uniform grid case. Table 4-3 lists the clock time of total simulation, AMR process, and the ratio to the clock time of the uniform case, and the comparisons show that

- The 4L case, of which results almost overlap with the uniform ones, spends only 12.25% of the computational resources in the later one. Also, this value agrees well with the theoretical efficiency of 4-level refinement, 12%, which is discussed in Table 3-2.
- The computational storage and memory load, which is proportional to the grid size, is much smaller in the AMR cases. The maximum grid ratio is observed in the 4L case, which is reasonable as its maximum-refinement level is the largest, and this maximum ratio is still no more than 20%.

- The ratio between amrTime and totalTime is less than 2%, even for the 4L case.

The performance of the 1D shock wave case shows the AMR efficiency is more than 5 times higher than the counterpart in traditional FVM methods. In addition, when extended to 2D or 3D simulation, this strength is much more distinct and increases exponentially.

4.1.2 1-D convection-diffusion of an inert H₂/O₂ front

The inert H₂/O₂ front moves with a constant velocity $u_0 = 20\text{m/s}$ in a uniform pressure field $p = 1\text{ atm}$. The domain is 6.6 cm long. At $t = 0$, the front profile is defined as

$$Y_{H_2} = \begin{cases} 0.5 \times \left[1 + \tanh \left(C \left(\frac{l}{2} - |x - x_0| \right) \right) \right] & , x \geq x_0 \\ 1 & , x < x_0 \end{cases} \quad (4.1)$$

$$T = \begin{cases} 1500 \times \left[1 - \frac{1}{3} \tanh \left(C \left(\frac{l}{2} - |x - x_0| \right) \right) \right] & , x \geq x_0 \\ 1000 & , x < x_0 \end{cases} \quad (4.2)$$

in which $x_0 = 3.3 \times 10^{-2}\text{ m}$, $l = 6.0 \times 10^{-3}\text{ m}$, and $C = 8 \times 10^3\text{ m}^{-1}$. $Y_{O_2} = 1 - Y_{H_2}$ and the front thickness is about 0.7 mm. $T_{H_2} = 1000\text{ K}$ and $T_{O_2} = 2000\text{ K}$. During the simulation, $cfl = 0.6$, $dx_L = 0.05$, and $dt_L \approx 10\text{ ns}$. Figure 4-2 compares my numerical results with the DNS results reported by Billet & Abgrall [59]. Their study modeled the interface as stationary, hence here the DNS results are shifted in the x -direction accordingly. At $400\text{ }\mu\text{s}$, the diffusions have smoothed the front to about 5 mm for the hydrogen and temperature profiles. The distributions predicted by the current study are in excellent agreement with the DNS results [59].

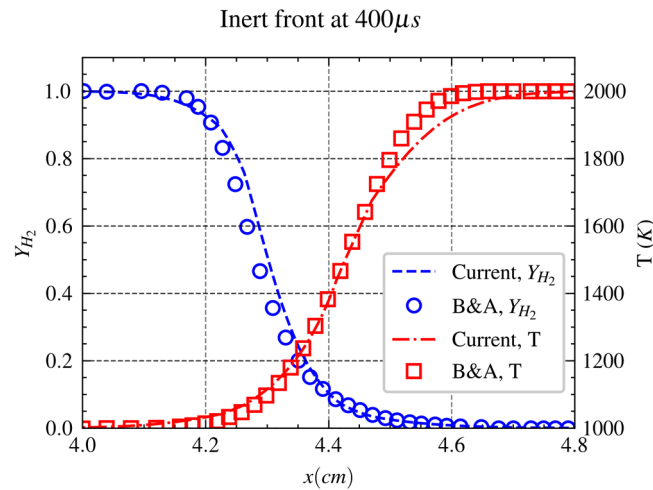


Figure 4-2. Solution of 1-D convection-diffusion of an inert front at $400\text{ }\mu\text{s}$. Results are predicted by Fire solver (lines) or from Billet & Abgrall [59] (symbols).

4.1.3 ISBI: vorticity

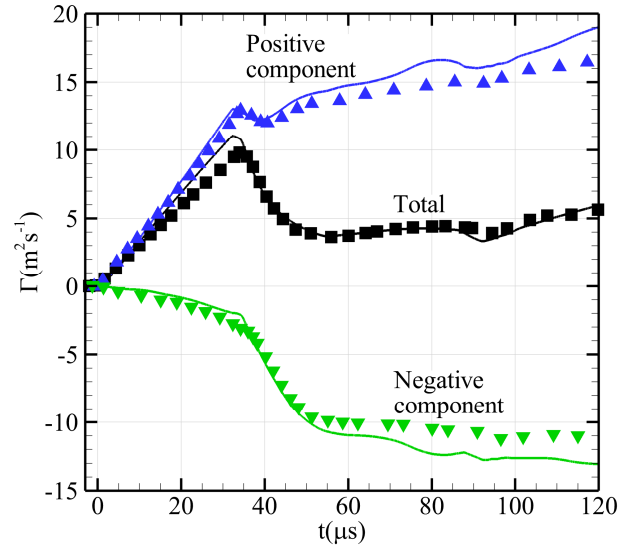


Figure 4-3. History of circulation Γ for the interaction of an $M = 1.22$ shock wave with a cylindrical bubble of R22. The markers are digitized from the results of a ‘smoothed’ interface in Niederhaus et al. [68]. The solid lines are results predicted by the Fire solver.

The cylindrical ISBI case reported in Niederhaus et al.’s numerical study [68] is reproduced. The initial bubble radius is 0.01 m, and pre-shock states are set as $T = 293$ K and $p = 1$ atm. The computational domain is similar to Figure 4-4 with scales following Ref.[68]: $x \in [0, 0.07]$, $y \in [0, 0.025]$. The root-level grid is of 25 Pts/R (points per radius length), and $L = 3$ AMR grids are applied with $dx_3 = 50 \mu\text{m}$. The behavior of total vorticity $\Gamma = \int \omega dx dy$ along with the negative and positive components are plotted in Figure 4-3. The ω value is calculated with transform current coordinates to the cylindrical coordinates in Ref.[68].

The circulation history in Figure 4-3 shows the Γ histories predicted by the Fire solver agree well with that in Ref.[68]. As the EOS in Fire (thermally perfect gas) is different from the one (calorically perfect gas) in Ref.[68], some reasonable discrepancies are observed in total vorticity before 40 μs , and in positive and negative components after 50 μs .

4.1.4 Axisymmetric ISBI study

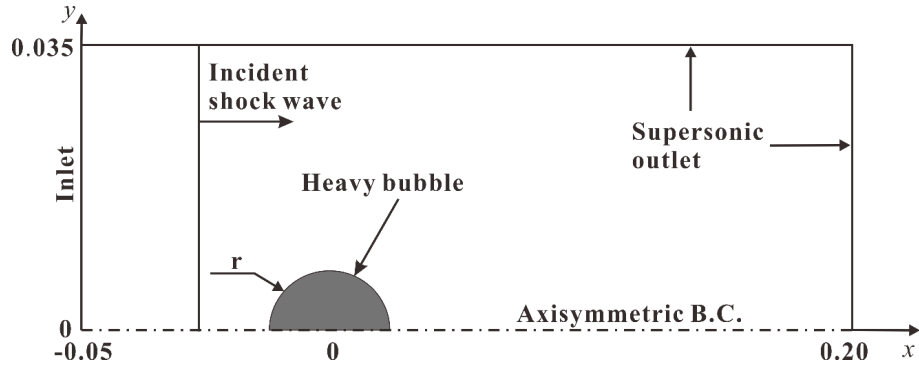


Figure 4-4. The initial geometry of the ISBI problem. The units are mm.

Table 4-4. Thermodynamic properties of gases in the simulation

Gas	Air	SF ₆
Pressure (atm)	1.0	1.0
Temperature (K)	298	298
Density (kg/m ³)	N ₂ 0.90468 O ₂ 0.27482	SF ₆ 5.97292

An ISBI study in Zhai et al. [84] is numerically reproduced as a benchmark test. In Ref.[84], the interaction of a planar shock with a heavy spherical bubble is researched experimentally and numerically, and detailed flow structures are captured by both high-speed schlieren technology and numerical method. The initial configuration is shown in Figure 4-4, and the problem is considered as axisymmetric. The nominal bubble diameter $D_0 = 3$ cm and the bubble is filled with pure SF₆ while the surrounding gas is air. Detailed initial thermodynamic properties are listed in Table 4-4, and the properties of viscosity modeling μ are shown in Table A-1. The Atwood number is 0.67. The incident shock wave propagates from left to right with $M = 1.23$ with the shock speed $W_s = 418.2$ m/s. The post-shock states are initialized using Rankin-Hugoniot relations.

To show the merits of the Fire solver, both the computational domain and the minimum grid size are kept the same with Ref.[84] for comparison. The domain size is 250 mm \times 35 mm. The lower boundary is treated as the symmetric axis, the left boundary as supersonic inlet, and the others as supersonic outlets. The numerical modeling mainly disagrees with the experimental setup as: first, the numerical method in Fire is only suitable for gaseous modeling, thus, the liquid soap film is not considered; second, in the experiment, the cross-section of the shock tube is rectangular while is a circular one in current numerical modeling; third, due to the interferences of the supporting device in the experiment, the bubble shape deviates from an ideal sphere. In addition, this device also

affects the interface evolution, especially at the lower half of the bubble sphere. Despite all these deviations in modeling, close agreements between the results in the current numerical study and experiment are attained.

Grid convergence test

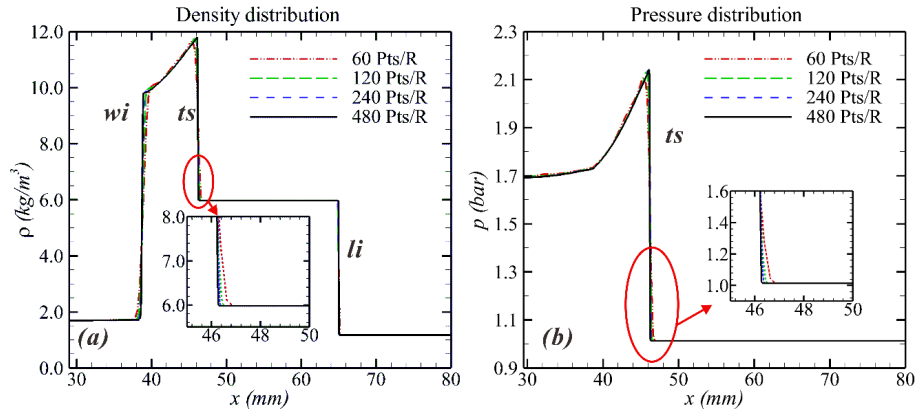


Figure 4-5. Grid convergence tests. (a) p and (b) ρ distribution along the bubble axis with grid resolution varies from 60 to 480 Pts/R for the viscous cases at 49 μ s. wi: windward interface, ts: transmitted shock, li: leeward interface.

Only the convergent numerical results are reliable for correct physical analysis. For the numerical ISBI study here, the sharpness of numerical shock wave structures is a proper convergent criterion and has been widely used. It shall be emphasized that the convergent criterion for the ISBI study is different from that for the RSBI case, and the latter one is much stricter and will be rigorously discussed in Chapter 5.

The p and ρ distribution on the axis at $t = 49 \mu$ s for the viscous cases are shown in Figure 4-5 (a) and (b) respectively. The root grid resolution is 60 Pts/R, and 4 testing cases are studied with $L = 0 - 3$. Correspondingly, the grid resolutions are 60, 120, 240, and 480 Pts/R. The detailed structures of transmitted shock (ts) are shown in the insets. Both insets display good grid convergence in pressure and density distributions. The blue dashed line of the 240 Pts/R (points per radius length) case overlaps well with the solid black line of the 480 Pts/R case. Although the 240 Pts/R grid setup already achieves grid convergence, for better comparison and consistency with Zhai et al.'s grid setup[84], $L = 3$ grids with 480 Pts/R are chosen in the following discussions and analysis.

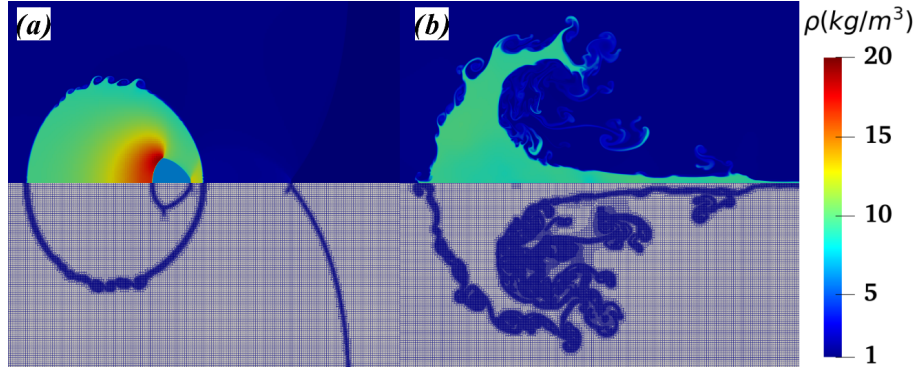


Figure 4-6. Density contour (upper parts) and AMR grid (lower parts) at (a) 114 μs and (b) 514 μs .

To demonstrate the performance of AMR methods in this ISBI problem, both the density contour and grids at the early and the late stage are shown in Figure 4-6. Figure 4-6(a) presents the flow field at 114 μs , in which the AMR grids are refined to 3rd level to capture the bubble interface, KHI structures around the bubble equator, refracted shock inside the bubble, and refracted shock downstream. Figure 4-6(b) presents the density contour and grids at 514 μs , at this moment, the bubble interface is filled with small-scale vortices caused by the KHI and RMI which are numerically described by highly-refined AMR grids.

Results and discussion

In Zhai et al.'s experimental study[84], the evolution of ISBI is recorded by an integrated high-speed schlieren system. In this section, the experimental and numerical results will be compared mainly based on the schlieren images. Several dimensionless properties are introduced to describe the bubble morphology, the vortex length L_v , and TBD width. The length scales are nondimensionalized by D_0 as

$$L_v^* = \frac{L_v}{D_0}, W^* = \frac{W}{D_0} \quad (4.3)$$

the hydrodynamically characteristic time is defined as $\tau_h = D_0/W_s \approx 71.7 \mu\text{s}$ and the dimensionless time is defined as $t^* = t/\tau_h$.

The integrated schlieren system is short at revealing the detailed flow structures inside the bubble, especially at the later stage, as the remains of soap film interfere with the schlieren system. Thus, the following discussions will be mainly based on the wave pattern at the early stage, including the primary counter-rotating vortex (CRV) and interface development.

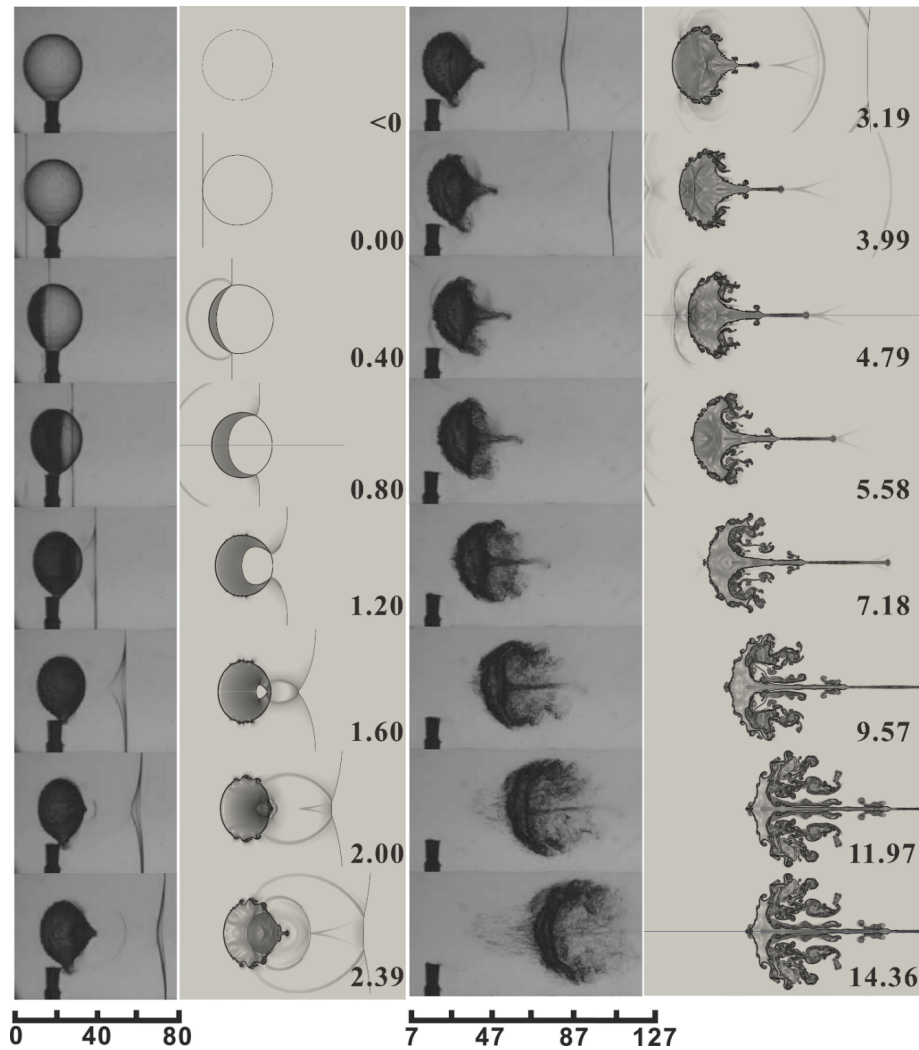


Figure 4-7. Experimental (1st and 3rd columns) and numerical (2nd and 4th columns) schlieren images for the SF₆ $M = 1.23$ ISBI results. The experimental images are from Ref. [84], and the numerical images are predicted by the Fire solver with $L = 3$.

Figure 4-7 presents both the experimental and numerical schlieren images with each moment labeled by dimensionless time t^* , and the physical temporal duration is around 1100 μs . The numerical results are mirrored for better comparison. Similar to the temporal classification in Ref. [68], the development of ISBI is divided into three temporal stages:

- Initial stage when $t^* < 1 + \pi/2$: the curved shock waves arrive at the downstream bubble pole.
- Intermediate stage when $1 + \pi/2 < t^* < 4$: the shock-focusing occurs, and a jet emerges at the downstream pole.
- The later stage when $t^* > 4$. During which the bubble interface is more convoluted, and the primary CRV appears.

At $t^* = 0.40$, the incident shock interacts with the windward side interface, and this interaction generates the refracted shock wave and a reflected shock wave due to acoustic impedance and mechanical equilibrium. The incident shock wave then travels nearly perpendicular along the leeward side interface ($t^* = 1.20$). As the Atwood number is large ($At = 0.67$), the transmitted shock travels much slower than the incident shock and gradually becomes irregular [68]. At $t^* = 1.60$, the curved diffracted shock waves along the upper and lower hemisphere meet at the downstream pole outside the bubble, while the refracted shock converges inside the bubble. The high-pressure region caused by SFP pushes the bubble gas streaming outside by a jet at the downstream pole ($t^* = 2.00$). The mushroom-like structures caused by RMI are observed around the jet at $t^* = 3.19$, also the effect of KHI is distinct around the equator at this moment. The primary vortex starts developing at $t^* = 3.99$. Because of SFP, an upstream-traveling shock propagates along the bubble axis and transits through the upstream interface at $t^* = 4.79$. The distance between transmitted shock and interface in the experiment is smaller than that of the simulation. Due to the RMI, the interface at the upstream pole becomes unstable at $t^* = 5.58$, and sooner develops into a jet at $t^* = 7.18$. This jet structure is proved by a dark tip protruding at the upstream pole in the experimental image at the exact moment. The primary vortex gets more convoluted as the bubble travels further to the right. At $t^* = 9.57$, both the experimental and numerical images show the shedding behavior during the evolution of the primary vortex. The main disagreement in the numerical results is an abnormally long jet structure at the axis downstream. Nevertheless, as this long jet locates far away from the major of the bubble, the evolution of bubble gas and interface is little disturbed by it. Also, another disagreement lies in the last two frames, where some obscure structures are detected upstream of the leeward side only in the experimental image. These lagging structures are confirmed in my early work as the soap fog driven by the flow field [122].

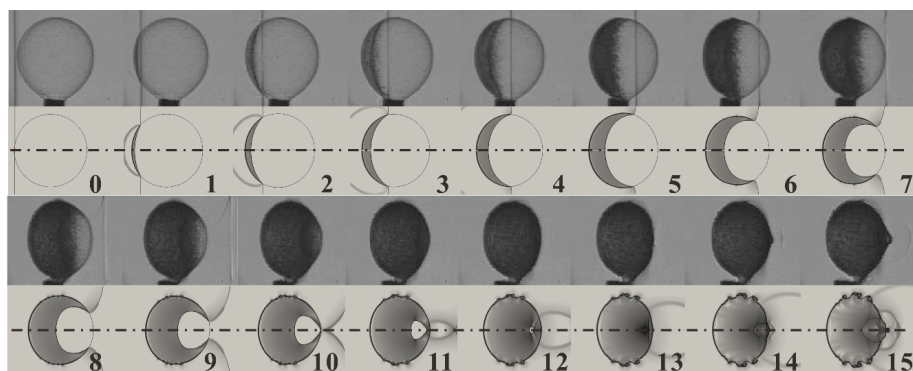


Figure 4-8. Experimental and numerical schlieren images of the ISBI at the initial stage for $M = 1.20$ and $D_0 = 30$ mm with the time interval of $10 \mu\text{s}$. The experimental images are from Ref. [84], and the numerical images are predicted by the Fire solver with $L = 3$.

Figure 4-8 presents the experimental and numerical schlieren images of the ISBI at the initial stage for $M = 1.20$ and $D_0 = 30$ mm. The detailed process of the SFP and jet formation is clearly shown. A good agreement can be found between the numerical predictions and experimental results. In frames 1–4, before the incident shock wave arrives at the equator, the refracted shock wave is a regular type. It shall be highlighted that $t^* \approx 0.5$ in frame 4. Later as the incident shock travels along the leeward side interface, the refracted shock gets more curved as it cannot catch up with the incident shock (frame 5-9). Sooner in frame 10, it reconfigures into a Type-I shock-shock interaction, according to Edney [6]. Also, in this frame, the upper and lower diffracted shock interacts at the axis. The outcome shocks of this interaction then travel upstream and transmit into the bubble, then compress the bubble gas together with the refracted shock (frame 11-12). This is the mechanism of the shock-focusing phenomenon, which creates a tiny region of extremely high pressure and high temperature inside the bubble [88]. The downstream-traveling shocks interact with the interface and produce a jet at the downstream pole (frame 13-15).

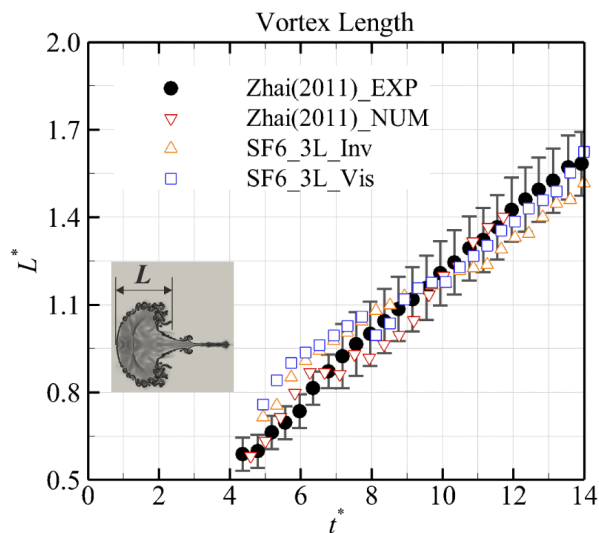


Figure 4-9. The dimensionless primary vortex length L_v^* as a function of t^* . The circle and gradient markers are results digitized from Ref.[84], and the triangle and square markers represent inviscid and viscous results predicted by the Fire solver with $L = 3$, respectively.

Both inviscid and viscous numerical studies are performed using the current AMR method and compared with the experimental and numerical results in Ref.[84]. The inviscid AMR simulation is performed as the reported numerical results in Ref.[84] is inviscid. Figure 4-9 presents the history of dimensionless primary vortex length in all the cases. The general trend of L_v^* increment in the experiment is well predicted by all three simulations. The current AMR program overpredicts the primary vortex length when $t^* < 8$, for both inviscid and viscous cases, and when $t^* > 8$, the agreement with experiments is much better, especially for the viscous one even in a very later

stage at $t^* = 14$. Altogether, the prediction of L^* value in my program exceeds the one in Ref.[84] after $t^* = 8$, while is worse before that moment.

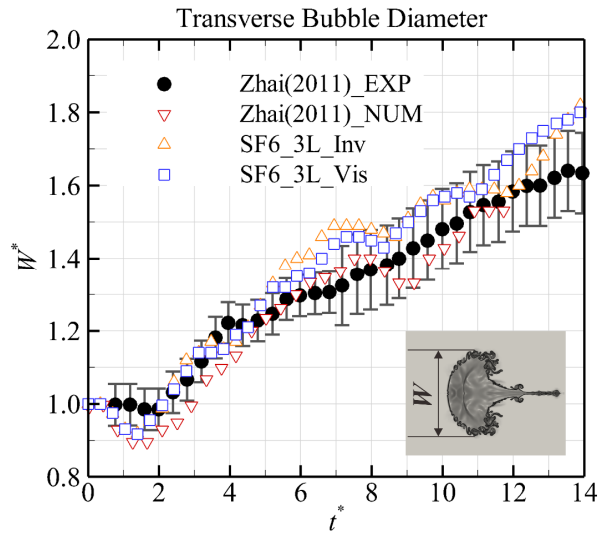


Figure 4-10. The dimensionless TBD value (W^*) as a function of t^* . The solid circle and reversed triangle are digitized from Ref.[84], and the triangle and square markers represent inviscid and viscous results predicted by the Fire solver with $L = 3$, respectively.

Figure 4-10 presents the history of W^* for all the cases. Surprisingly, in the early stage when $1 < t^* < 2$, the experimental W^* is larger than any of the three numerical predictions. However, as this valley shape of TBD is obtained by many numerical and experimental studies such as Ref.[89, 114], the numerical results shall be more accurate here, and the disagreements shall be attributed to experimental uncertainty. When $2 < t^* < 4$, the experimental W^* increases as the size of the vortex structure expand, then after $t^* = 4$, it keeps increasing but with a lower growth rate. This trend is well predicted by all three numerical studies. Comparing the matching with experimental results, both the inviscid and viscous show better prediction than the one in Ref.[84] when $2 < t^* < 5$. After $t^* = 5$, all the numerical results lie inside the error band, except for a small period in the range $6 < t^* < 7$ for the current AMR method.

4.1.5 Mass conservativity of REC and SEC setup

In Section 3.3.3, two FVM methods with different treatments on finite cells are discussed to model the axisymmetric flow. The LHS terms in Equations (3.57) and (3.58) are the non-conservativity contribution of axisymmetric source terms. In this section, numerical experiments are performed to quantitatively evaluate the mass conservativity of these two FVM methods, and other setups of the problem are kept the same as those in Section 4.1.4.

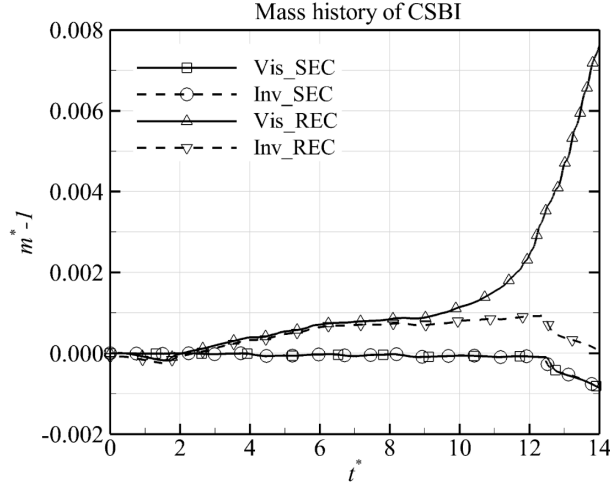


Figure 4-11 The global mass history of the ISBI case in 4 different numerical experiments. The lines with square and circle markers represent viscous and inviscid cases using SEC configuration, and the ones with the triangle and reversed triangle markers represent viscous and inviscid cases using REC configuration.

The global mass conservativity $m_b^*(t) = \frac{m_b(t)}{m_{b,0}}$ is defined as the ratio between instantaneous bubble mass and initial bubble mass. The bubble mass $m_b(t)$ is numerically calculated by accumulating the mass of SF₆ in the flow domain according to

$$m_b(t) = \sum_i \rho_{\text{SF}_6,i}(t) dV_i = \sum_i \rho_{\text{SF}_6,i}(t) \cdot 2\pi y_i \Delta x_i \Delta y_i \quad (4.4)$$

where i is a generalized cell index, y_i is the radial coordinate of cell center, Δx_i and Δy_i are the length scales. To show the accuracy of Eq. (4.4), the theoretical initial bubble mass is compared here for reference. For an ideal bubble with $D = 3$ cm and $\rho_{\text{SF}_6} = 5.97292$ kg/m³, the theoretical bubble mass is,

$$m_{b,0,\text{theo}} = \frac{1}{6} \pi D^3 \cdot \rho_{\text{SF}_6} = 8.444 \times 10^{-5} \text{ kg}$$

and the initial bubble mass numerically evaluated by Eq. (4.4) is,

$$m_{b,\text{num}} = 8.436 \times 10^{-5} \text{ kg}$$

The relative error of the initial mass is,

$$\delta = \frac{|m_{b,\text{num}} - m_{b,0,\text{theo}}|}{m_{b,0,\text{theo}}} \approx 0.09 \%$$

Thus, Eq. (4.4) is quite accurate at the initial moment.

Figure 4-11 plots the mass history of four ISBI cases which utilize different axisymmetric implementations and are either viscous or inviscid. The vertical coordinate shows the numerical deviation of the total mass. For the SEC implementation, both the inviscid and viscous cases maintain strict mass conservativity, and the relative

deviation is less than 0.01% when $t^* = 1.6$. However, for the REC configuration, obvious deviations are observed and are not monotonous. Before $t^* < 2$, the bubble mass decays in both inviscid and viscous cases, and the maximum mass deviation is around 0.02%. At $t^* = 1.6$, m_b starts increasing and exceeds the initial mass by about 0.1%. After $t^* = 10$, the effect of viscosity becomes prominent. The large slope of the viscous case indicates that its total mass rapidly increases and quickly exceeds 0.7% at $t^* = 14$, while the deviation of the inviscid case keeps lower than 0.1%. At $2 < t^* < 12$, the declination of both the SEC cases is caused by the limitation of the computational domain, as the tail of the bubble flows out of the downstream boundary. Although the mass of the inviscid REC bubble decreases, the viscous one keeps rapidly increasing. These numerical experiments show the mass conservativity is mostly maintained in the SEC configuration and is destroyed in the REC one. Besides, the relative mass deviation of the viscous case is more prominent, and its value can be more than 5 times larger than the inviscid counterpart at $t^* = 14$.

In this thesis, the SEC axisymmetric model is implemented in all axisymmetric simulations without further declaration. Eq. (3.49) shows that in the REC configuration, not only the global mass but all global conservative properties are affected by the axisymmetric source terms. Also, the vectors on LHS are inviscid and viscous contributions, respectively. The global mass is discussed here as it is the easiest one to track. Since the density is highly coupled with other conservative variables in the compressible flow, the conservativity of other global properties, such as global energy and global momentum, are also worth studying. Furthermore, as the temperature and pressure are crucial in reacting flows, the influences of these two axisymmetric implementations on these primitive variables are also interesting problems. These will be covered in future works.

4.2 Applications on reactive flows

4.2.1 0th-dimensional cases

In this thesis, the pressure-dependent H_2/O_2 mechanism in Ó Conaire et al. [60] is used to model combustion at elevated temperatures and pressures during shock focusing. Figure 4-12 shows the ignition delay time with $X(H_2:O_2:Ar) = 2:1:97$ at 33 atm as predicted by several chemical mechanisms and measured in shock tube experiments by Petersen et al. [28]. Comparisons show that our simulation with the Ó Conaire mechanism performs well against the experiments, showing that the Ó Conaire mechanism suits the high-pressure combustion simulation with good accuracy. Figure 4-13 shows the prediction of induction time at 1 atm by Ó Conaire' mechanism predicted by the same manner, and the results also match well with experimental data.

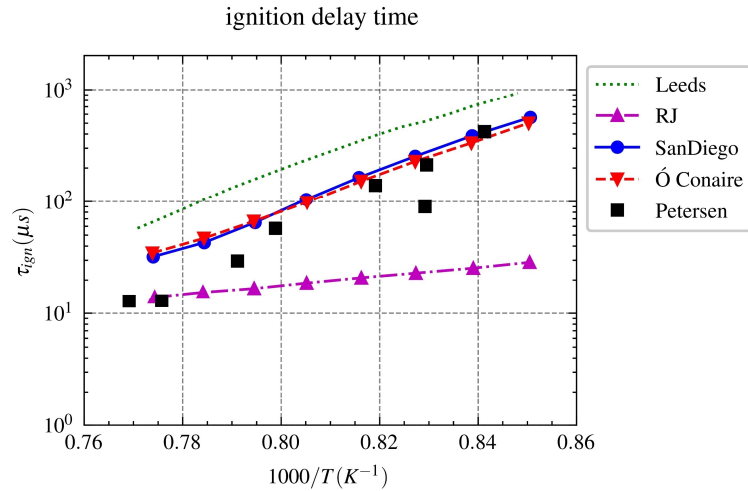


Figure 4-12. Ignition delay time with $X(\text{H}_2:\text{O}_2:\text{Ar}) = 2:1:97$ at 33 atm. Numerical predictions: the Leeds mechanism is from Ref. [46], RJ represents the reduced Jachimowski mechanism from Ref. [19], the San Diego mechanism is from Ref. [106], and the Ó Conaire mechanism is from Ref. [60]. The experimental data are from Petersen et al. [28].

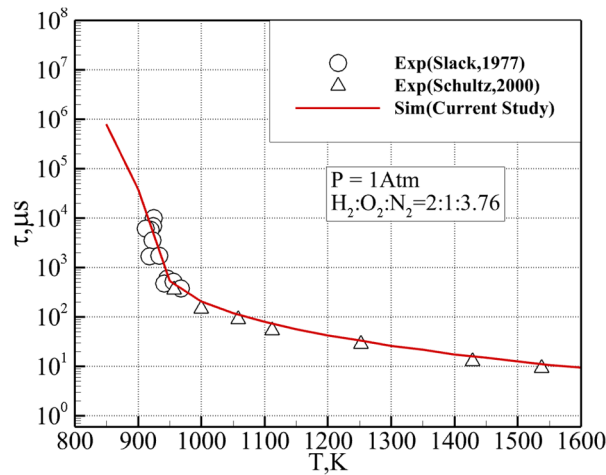


Figure 4-13 Induction time with $X(\text{H}_2:\text{O}_2:\text{N}_2)=2:1:3.76$ at 1 atm. Experimental data are from Slack [11] and Schultz and Shepherd [131]

4.2.2 1-D detonation initiated by a reflected shock

Follow the problem considered in Ref. [47, 102], a one-dimensional detonation initiated by the reflection shock is simulated here. The composition is $X(\text{H}_2:\text{O}_2:\text{Ar}) = 2:1:7$. For consistency, the 9-species/37-step H_2/O_2 chemical mechanism in Paolucci et al. [102] is used. The domain is $L = 12$ cm long. The left boundary is an inlet, and the right is a solid, adiabatic wall. Initially, a right-propagating shock wave is set up at $x_0 = 6$ cm with the following jump conditions

$$\begin{aligned}
& x < 6 \text{ cm}, & x \geq 6 \text{ cm} \\
\rho_1 = 1.8075 \times 10^{-1} \text{ kg/m}^3, & \rho_2 = 7.2 \times 10^{-2} \text{ kg/m}^3, \\
p_1 = 3.5594 \times 10^4 \text{ Pa}, & p_2 = 7.173 \times 10^3 \text{ Pa}, \\
u_1 = 4.8734 \times 10^2 \text{ m/s}, & u_2 = 0 \text{ m/s}, \\
T_1 = 7.4767 \times 10^2 \text{ K}, & T_2 = 3.7825 \times 10^2 \text{ K}.
\end{aligned}$$

where the superscript 1 or 2 representing the left or right sides of the jump. The shock profile is given as

$$\Gamma(x) = \frac{1}{2} \left[(\Gamma_1 + \Gamma_2) - (\Gamma_1 - \Gamma_2) \tanh \left(\frac{x - x_0}{1.2 \times 10^{-4}} \right) \right] \quad (4.5)$$

where $\Gamma = (\rho, p, u)^T$. During the simulation, $cfl = 0.6$, $dx_0 = 1 \text{ mm}$, $L = 5$, and $dt_L = 8 \text{ ns}$.

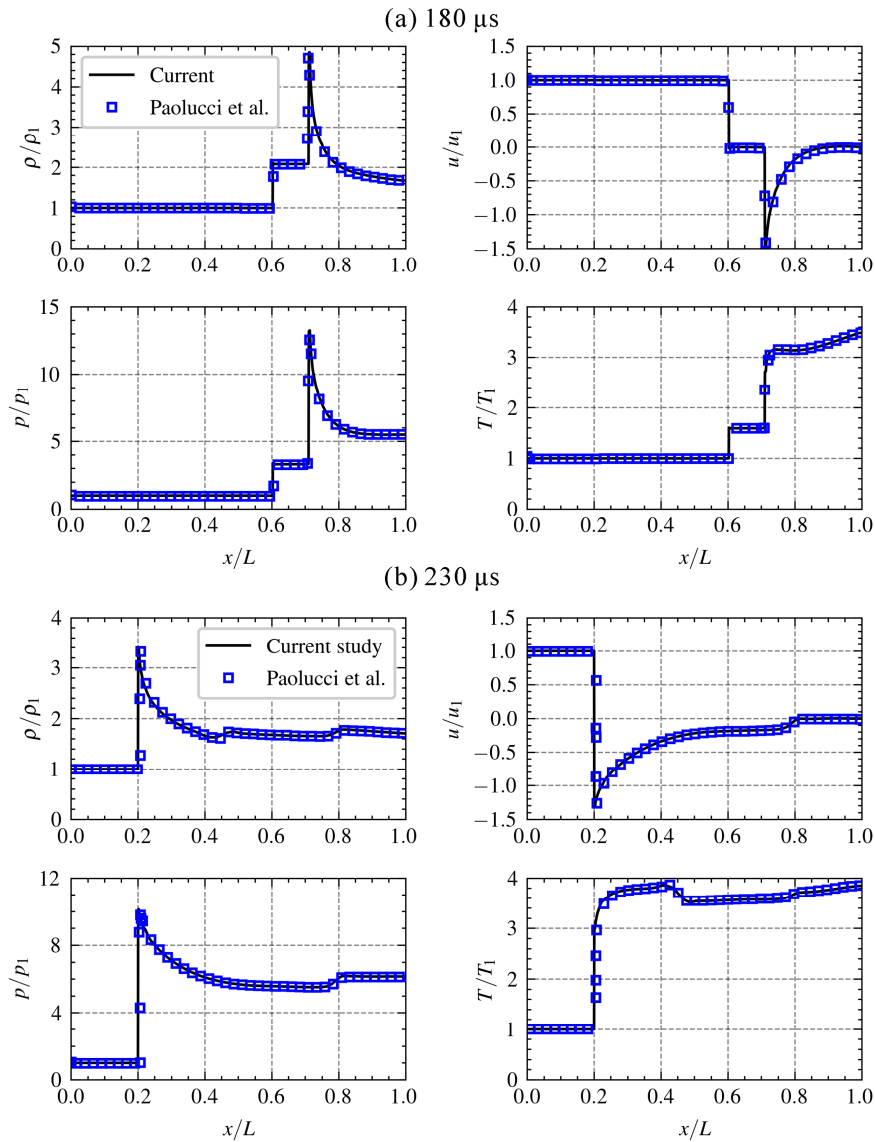


Figure 4-14. Solution of 1-D detonation at (a) 180 μs and (b) 230 μs . Results are from results using the Fire solver (lines) or from Paolucci et al. [102]. (symbols).

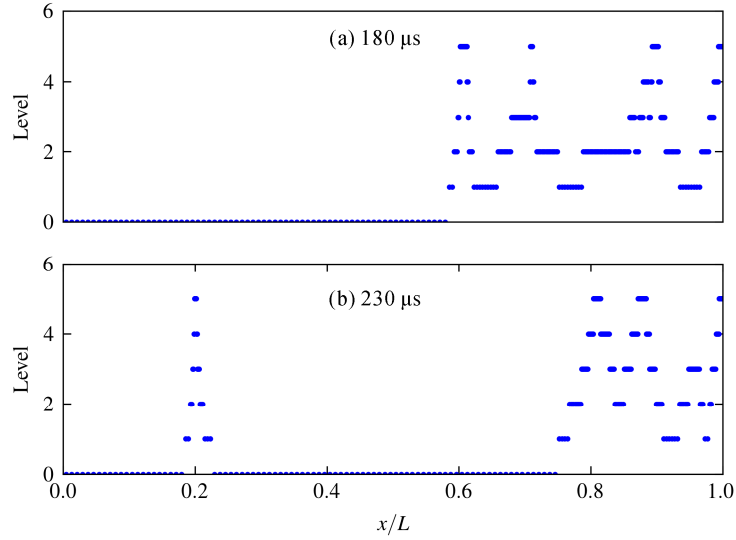


Figure 4-15. Adaptive mesh distributions of 1-D detonation at (a) 180 μs and (b) 230 μs .

4.2.3 1-D detonation initiated by temperature gradient profile

The Zeldovich mechanism [13], which points out that the gradient of reactivity determines the speed of the intensive reaction zone, is crucial in explaining the detonation formation. In this section, a linear temperature gradient is chosen to initiate the detonation of the H_2/O_2 mixture using the Ó Conaire mechanism, and the numerical results are compared with the results reported by Liberman et al.[82] for validation. The initial flow field is defined as

$$p(x, 0) = p_0, u(x, 0) = 0, T(x, 0) = T^* - (T^* - T_0)\left(\frac{x}{L}\right), 0 \leq x \leq L.$$

The temperature gradient is characterized by the ratio of the temperature difference ($T^* - T_0$) and the length of the temperature gradient. For the H_2/O_2 mixture at $p_0 = 1$ atm, $T^* = 1500$ K is higher enough for ignition, and $L = 8$ cm ensures a shallow reactivity gradient for detonation.

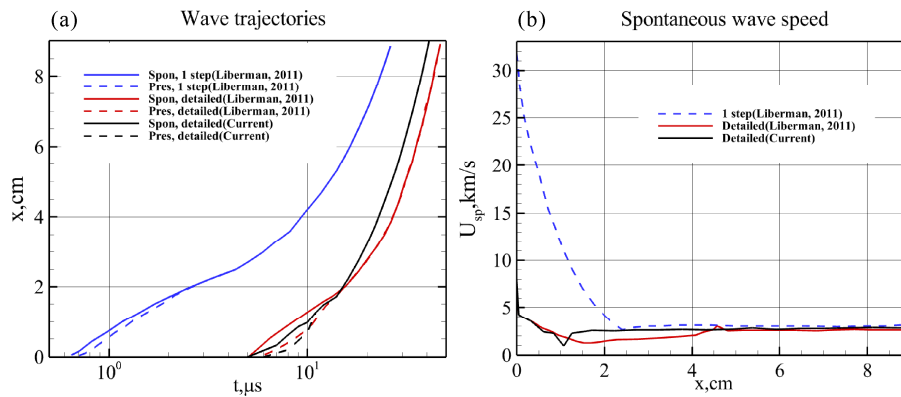


Figure 4-16. Numerical results of the 1D detonation test. (a) Spontaneous wave (solid lines) and pressure waves (dashed lines) trajectories, (b) Velocity of the spontaneous wave. The data of blue and red lines are from Ref.[82].

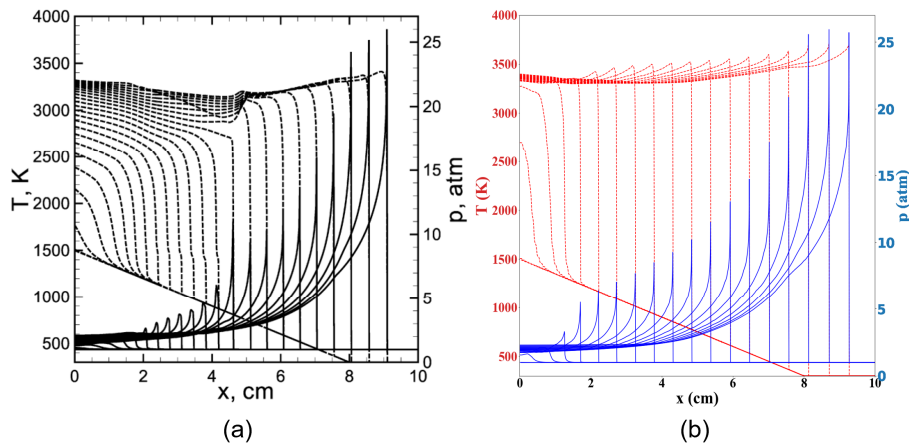


Figure 4-17. Detonation initiation process by the $L = 8$ cm temperature gradient in H_2/O_2 stoichiometric mixture at $p_0 = 1$ atm. (a) the result in Ref.[82], (b) the results predicted by the Fire solver $\Delta t = 2\mu s$.

Figure 4-16(a) presents the spontaneous wave and pressure wave trajectories predicted either in Ref.[82] using 1-step or detailed mechanism or in this thesis. The current numerical results agree well with the results of the detailed model in Ref.[82] in the case of induction time and initial spontaneous wave speed. The difference between the results of the detailed chemical models and the 1-step chemical model is essential. The long delays predicted by both detailed chemistries are the induction stage related to the chain branching reactions. The detailed chemical models predict a fast wave speed and weak chemical acoustic adjustment significantly different from the 1-step chemistry case.

Figure 4-17 presents the detonation initiation process by $L = 8$ cm temperature gradient in Ref. [82] (subfigure (a)) and predicted by current AMR code (subfigure (b)). Though different H_2/O_2 mechanisms are used in these two numerical studies, the detonation initiation processes are similar. The pressure wave gradually propagates to the RHS of the computational domain. At around 8.5 cm, both simulations predict the same pressure peak almost at the same moment.

4.3 2-D RSBI case

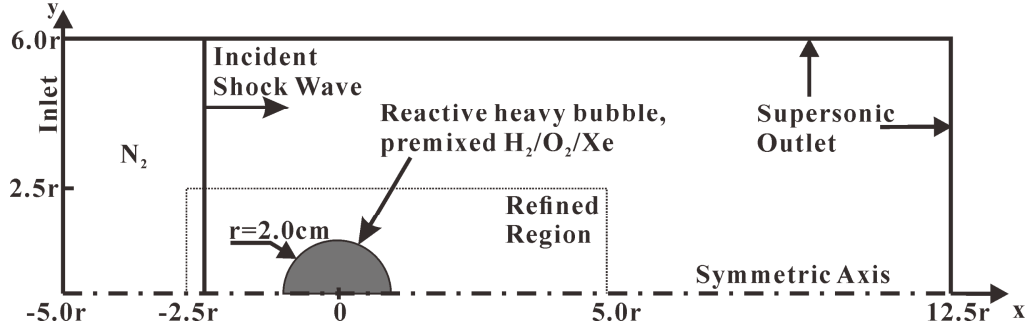


Figure 4-18. The computational domain of ISBI and RSBI simulations.

I study the inert and reactive SBI within a two-dimensional domain in Figure 4-18 and use the symmetric assumption to reduce the computational load. The left boundary is set as the inlet, the upper and right boundaries are set as the supersonic outlet, and the lower boundary is set as symmetric. Initially, the bubble center is located at $(0,0)$. The bubble and its surrounding N_2 atmosphere are defined by the molar fraction of the bubble mixture, similar to that in Ref. [107]:

$$X_{\text{bubble}} = \frac{1 - \tanh\left(\left(\sqrt{x^2 + y^2} - r\right) \cdot C\right)}{2} \quad (6)$$

where $r = 2 \text{ cm}$ is the nominal bubble radius, $C = 2 \times 10^5$ and $X_{N_2} = 1 - X_{\text{bubble}}$. For both inert and reactive SBI simulations, the bubble compositions are $X(\text{H}_2:\text{O}_2:\text{Xe}) = 2:1:3.76$, and the chemical source terms are switched off in the inert case. The computational domain is a $17.5r \times 6r$ rectangle. The incident shock wave propagates from the left side of the computational domain, and the post-shock states are set according to the Rankin-Hugoniot relations. I perform a numerical study on the $M = 2.30$ cylindrical RSBI problem by following the initial setups in Ref.[108]: initially, the pre-shocked states are $T_1 = 350 \text{ K}$ and $p_1 = 0.5 \text{ atm}$. To further decrease the computational load, once the bubble is ignited and the predicted combustion type is stable, the computational domain moves with some constant speed relative to the laboratory coordinate system to keep the shocked bubble inside the refined region. This is achieved by subtracting the shocked bubble speed calculated using a one-dimensional simulation from the velocity field and was prevalently utilized in other combustion simulations [37, 65, 70].

For code validation in this section, a 400 Pts/R grid comparable to Ref.[108] is applied without further grid-convergence study. Initially, $T_1 = 350 \text{ K}$ and $p_1 = 0.5 \text{ atm}$. As Ref. [108] evaluated the inviscid fluxes using a 6th-order scheme, we manage to achieve similar results by halving the minimum grid size. $L = 3$, and in the refined region, $dx_0 = 400 \mu\text{m}$ and $dx_L = 50 \mu\text{m}$.

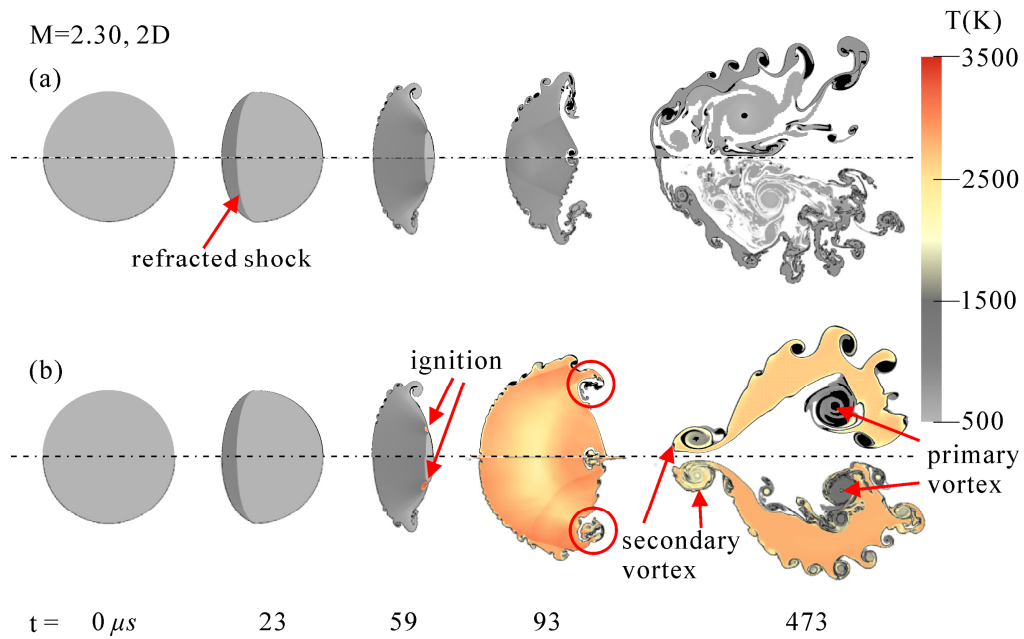


Figure 4-19. Temperature contour plots of (a) the 2D cylindrical ISBI case and (b) the RSBI case with limiting $Y_{Xe} > 0.1$. In each subfigure, the upper regions depict the results in this study, and the lower regions depict the results in Ref. [108].

Figure 4-19 compares the simulated temperature contours of the cylindrical RSBI and ISBI cases at $M = 2.30$ between this study and Ref. [108]. Without further notice, the thick black/purple lines delineate the iso contour of $Y_{Xe} \in [0.35, 0.55]$, representing the bubble interfaces, and the dash-dotted lines represent the symmetry lines (in the cylindrical case) or the axis (in the axisymmetric case). Comparing our results with those in Ref. [108], the ISBI behaviors are almost the same from 0 to $93 \mu s$. At $t = 473 \mu s$, although more small-scale structures are shown in Ref. [108] inside the vortex and on the interface, the bubble head location, position and shape of the primary vortex, and unstable interfacial structures are effectively reproduced in our AMR simulation. For the reactive case, the ignition time and location at $59 \mu s$ are nearly the same. At $93 \mu s$ and $473 \mu s$, the damping of unstable interfacial structures, heat expansion, and temperature distribution are also similar in both studies. These analyses prove that our numerical method is a reliable tool for RSBI simulations.

5. RSBI: grid convergence study and AMR criterion test

In this chapter, rigorous grid-convergence studies are present by examining the numerical flame structures predicted by different grid setups. The purposes of numerical RSBI cases in this thesis are categorized into 3 types:

- To validate the current code against previous numerical results(in Section 4.3).
- To present rigorous grid convergence study (in Section 5.1) and AMR criterion test (in Section 5.2).
- To analyze the flow fields in RSBI (in Chapter 6),

For all RSBI cases in Chapters 5 and 6, the initial setups and geometrical configurations are presented in Section 4.3 and Figure 4-18. The initial pre-shocked states in Haehn et al.'s experiment [88] are faithfully followed: $T_1 = 295$ K and $p_1 = 1$ atm. The $M = 1.34$ case is investigated as a representative of the lower limiting case, and the $M = 2.83$ case is investigated as a representative of the higher limiting case.

5.1 Grid-convergence study for $M = 1.34$ case

Five cases with different grid setups are tested. Table 5-1 and Figure 5-1 present the AMR grid setups around the bubble. In Case 134-1, $dx_0 = 400$ μm on the root level. In other cases, the root grids around the downstream pole are specially set with $dx_0 = 64$ μm to improve the computational efficiency and dynamic load balancing. From Case 134-2 to Case 134-5, the L_{chem} increases from 2 to 6, and dx_{min} decreases from 16 to 1 μm .

Table 5-1. The initial grid setups around the bubble in the grid-convergence study of the RSBI at $M = 1.34$.

Case ID	minimum dx_0 (μm)	L_{hydro}	L_{chem}	$dx_{\text{min}} = dx_{L_{\text{chem}}}$ (μm)
134-1	400	3	3	50
134-2	64	2	2	16
134-3	64	2	4	4
134-4	64	2	5	2
134-5	64	2	6	1

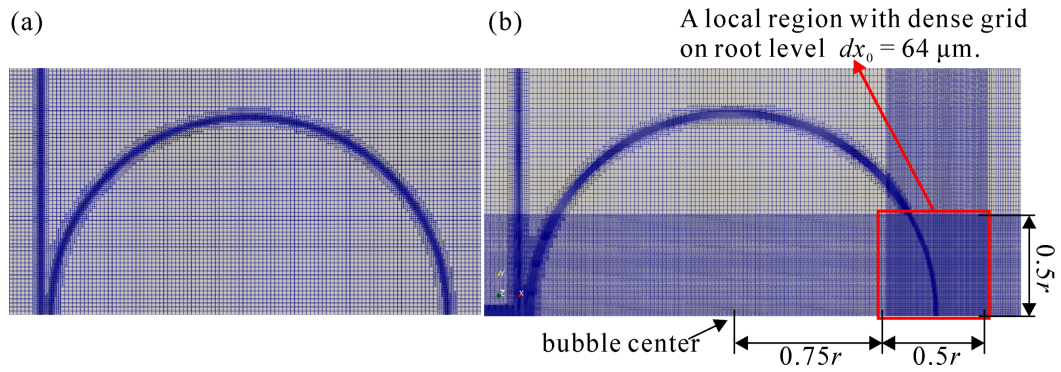


Figure 5-1. The initial AMR grids around the bubble in the grid-convergence study of the RSBI at $M = 1.34$. (a) Case 134-1. (b) Cases 134-2 to 134-5. The root grids in the $0.5r \times 0.5r$ area near the downstream pole are set to $dx_0 = 64 \mu\text{m}$.

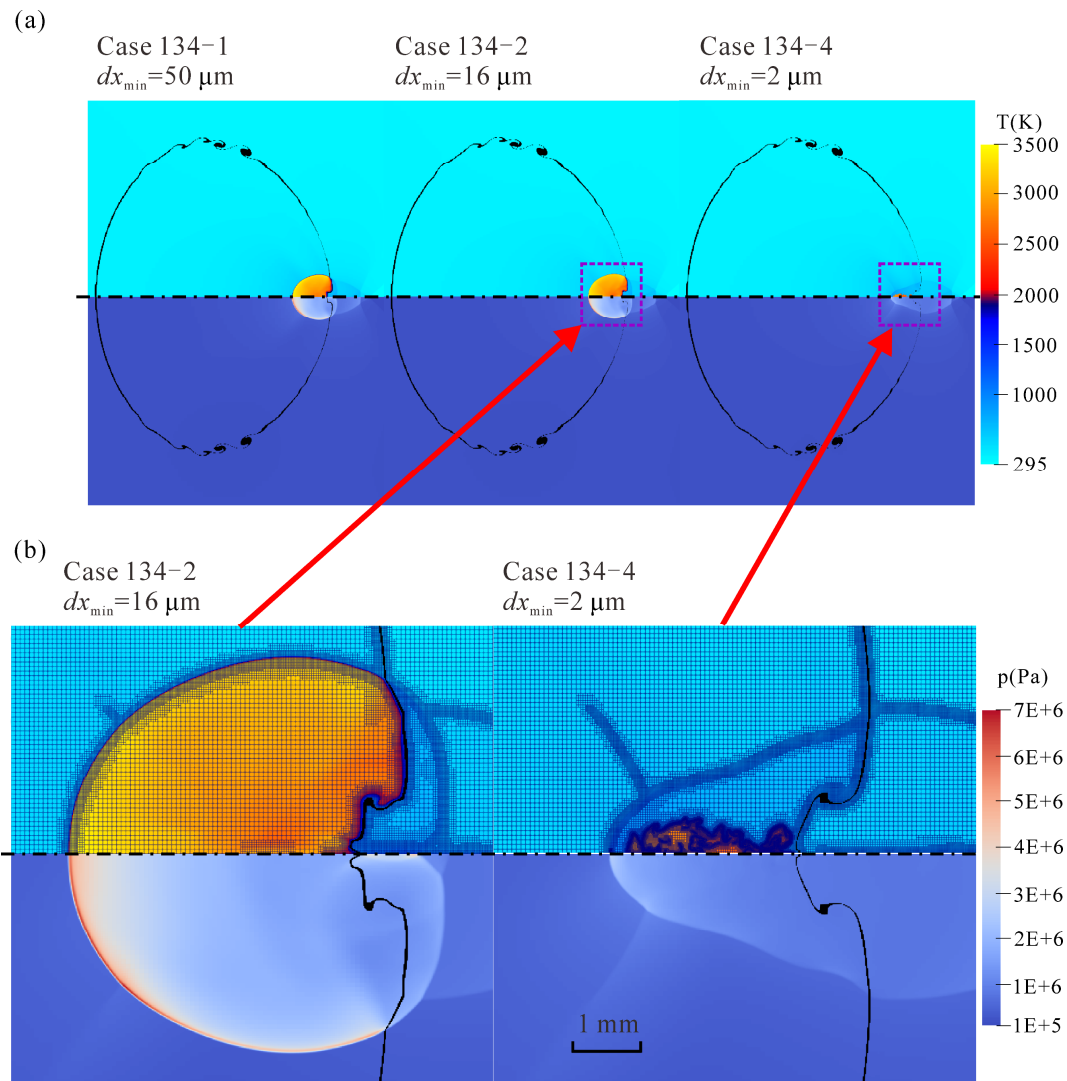


Figure 5-2. Flow fields for the $M = 1.34$ RSBI in Cases 134-1, 134-2, and 134-4 at $125 \mu\text{s}$. In each subfigure, the upper regions depict temperature contours, and the lower regions depict pressure contours. (a) Global views of the bubble in all 3 cases and (b) detailed views of the flame and grids for only Cases 134-2 and 134-4.

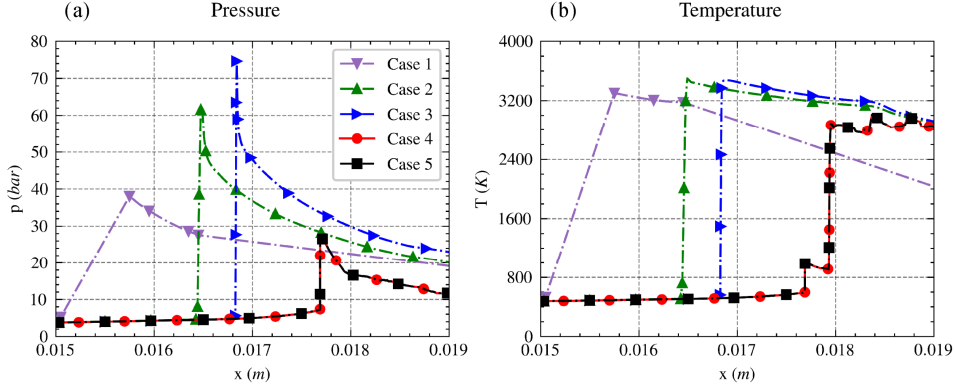


Figure 5-3. One-dimensional pressure and temperature distributions along the symmetry axis from Cases 134-1 to 134-5 at $125 \mu\text{s}$.

Figure 5-2 depicts the combustion results for the $M = 1.34$ RSBI at $125 \mu\text{s}$ in Cases 134-1, 134-2, and 134-4. At this moment, shock focusing ignites the bubble, and the combustion mode is stable. On the one hand, both the flames predicted in Cases 134-1 and 134-2 are spherical detonation waves; on the other hand, the flame in Case 134-4 is deflagration with a smaller flame and lower peak pressure when compared with the former cases. Further examination of the one-dimensional flame structures along the symmetry axis in Figure 5-3 shows that Cases 134-2 and 134-3 predict typical detonation waves in which the flame fronts closely attach to the preceding shocks with a large pressure jump, whereas Cases 134-4 and 134-5 predict consistent deflagration waves in which the flame fronts are decoupled from the shocks with a mild pressure difference. Therefore, the grids in Case 134-4 can adequately guarantee grid convergence in this combustion simulation.

The grids for Case 134-4 in Figure 5-2 (b) clarify the AMR strategy based on T_{et} in Section 3.2.3. The reflected shocks and bubble interfaces are colder than T_{et} and are only refined to the 2nd level ($L_{\text{hydro}} = 2$), while the flame fronts are hotter than T_{et} and become refined to the 5th level ($L_{\text{chem}} = 5$). Using this strategy, the flame fronts and reaction waves are adequately described by the grids ($dx_{L_{\text{chem}}} = 64 \mu\text{m}$), which are nearly one order smaller than the grids around the hydrodynamic discontinuities ($dx_{L_{\text{hydro}}} = 64 \mu\text{m}$), and the computational efficiency is higher than that exhibited when treating all discontinuities uniformly.

Therefore, the discussions and analyses of $M = 1.34$ cases in Chapter 6 are all based on the results from Case 134-4. The simulation covers $854 \mu\text{s}$ after the incident shock reaches the upstream bubble pole. For reference, the incident wave speed is $W_i = 468 \text{ m/s}$, the hydrodynamic time scale is $\tau_{\text{H}} = 2r/W_i = 85.4 \mu\text{s}$, and the non-scaled time

range $t^* = t/\tau_H$ is from 0 to 10. The time step is limited by a maximum CFL number of 0.3. The minimum time step is approximately 5.80 ns on the root level and 0.18 ns on the highest refined level when shock focusing and ignition occur. All simulations were performed in parallel on 180 cores of the Tianhe supercomputer in Tianjin Supercomputer Center, China, and the computational time for the reactive case was approximately 10 days.

5.1.1 Developments of detonation in Case 134-2 and deflagration in Case 134-4

To demonstrate the unphysical detonation caused by inappropriate grids, the development of detonation waves in Case 134-2 and the deflagration waves in Case 134-4 from a deflagration flow field is discussed.

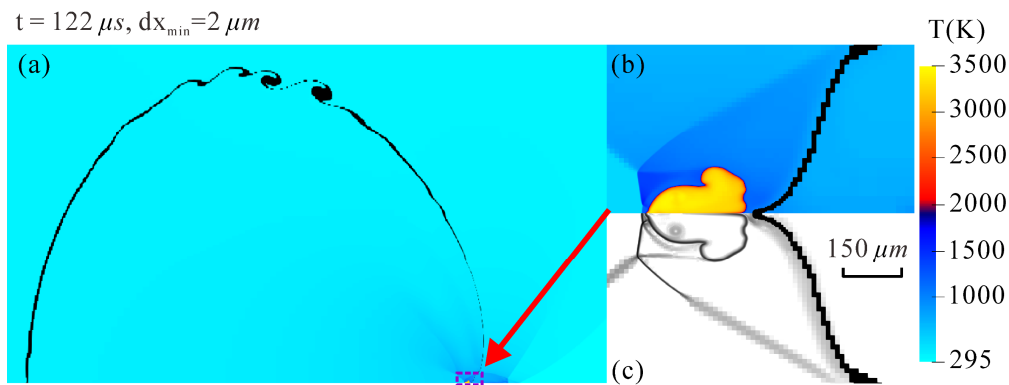


Figure 5-4. Flow fields for the $M = 1.34$ RSBI in Cases 134-4 at $122 \mu s$. (a) a global view of the bubble, (b) a detailed view of the flame, and (c) schlieren contours in the dashed purple rectangle near the SFP region.

Figure 5-4 presents the flame and schlieren contour in the Case 134-4 at $122 \mu s$, which is $3 \mu s$ ahead of pseudo-detonation in Figure 5-2. Figure 5-4 (a) shows a global view of the bubble and the flame appears near the bubble pole due to SFP. Figure 5-4 (b) and (c) are the temperature and numerical schlieren contours, respectively. The compression wave structures from the backward-propagating jet can be seen in subfigure (c). Also, the flame front is detached from the compressible wave, and a small gap is detected on the bubble axis.

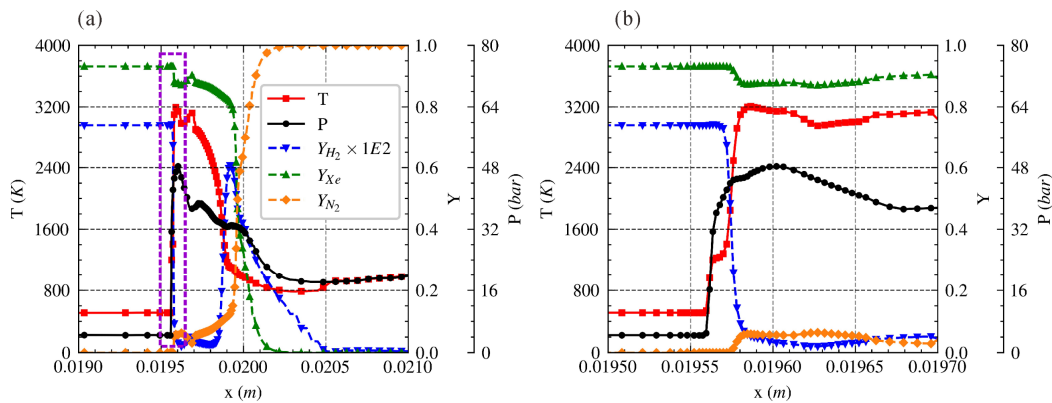


Figure 5-5. One-dimensional distribution of combustion properties along the bubble axis across the upstream frame fronts for RSBI Case 134-4 at $122 \mu s$.

Figure 5-5 presents the one-dimensional distribution of combustion properties across the flame for Case 134-4 at 122 μs . It shall be noticed that, though the mainstream travels from the left to right, the flow around the flame is convecting with an upstream-propagating jet to the left. Figure 5-5 (a) shows that Y_{Xe} decreases dramatically around $x = 0.04$ m where locates the downstream interface of the bubble. In the vicinity, Y_{H_2} reaches a peak at 0.0199 m, and gradually decades to zero at 0.0205 m. As H_2 is more diffusive than Xe , the width of H_2 diffusion length is longer than that of Xe . Also, the temperature gradually drops from 2400 K to around 900 K outside the bubble. The upstream flame front is found around 0.0199 m where a steep increase of temperature and drastic decrease of fuel present. Surprisingly, the mass fraction of inert species, Y_{Xe} , reaches a local minimum value at the flame front. Though Xe is not consumed in the reaction, it is diluted by the N_2 entrained by the jet flow. Interestingly, the distribution of Y_{N_2} is not intuitively monotonous. Figure 5-5 (b) displays an enlargement of the upstream flame front. To represent the grids across the flame, the markers in Figure 5-5 are set to represent the grid distribution in the numerical study: In subfigure (a), only 1 out of 4 numerical grids are plotted, while in subfigure (b), all grids are plotted. An apparent decoupling between the upstream pressure wave and flame on the bubble axis is observed in subfigure (b), and the gap is about 12 μm . Based on the Y_{H_2} distribution, the flame thickness is around 20 μm . To correctly predict the decoupling phenomenon and the flame structure from the first principle in the FVM method, the local grids must be able to discretize the flame profile smoothly [61].

It shall be noted that, at 122 μs , the flames in both Case 134-2 and 134-4 are deflagration and with similar flame structures. After 125 μs , Case 134-2 predicts a detonation wave, while Case 134-4 predicts a deflagration wave. These two different predictions indicate the detonation results in Case 134-2 are due to insufficient grid resolution.

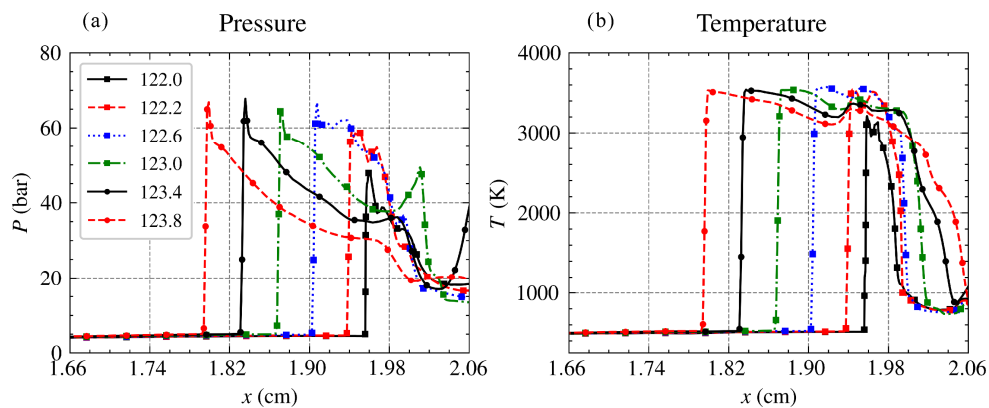


Figure 5-6. 1-dimensional distribution of pressure and temperature along the bubble axis across the upstream frame fronts in RSBI Case 134-2 from 122.0 to 123.8 μs .

Figure 5-6 presents the pressure and temperature distribution across the upstream flame in RSBI Case 134-2 from 122.0 to 123.8 μs . The peak pressure at the flame front increases from 48 bar at 122.0 μs to 59 bar at 122.2 μs , then raises to 66 bar at 122.6 μs . Meanwhile, the flame temperature increases from 3200 K to 3500 K. After 122.6 μs , a developed left-traveling detonation wave is observed. The peak pressure value at the detonation front is 68 bar at 123.4 μs . Based on the pressure profiles from 122.6 to 123.8 μs , the detonation front speed is around -916.6 m/s in the lab coordinate. The unburnt gas is at $p = 5.5$ bar, $T = 500$ K, and moves with $u \approx 180$ m/s. Considering the unburnt gas speed, the detonation flame speed is approximately 1096.6 m/s to the left. Using the SDToolbox by Lawson and Shepherd [119], the analytical CJ speed is 1116 m/s, which is very close to the detonation flame speed on the axis. Later, the flame develops to the detonation wave shown in Figure 5-2 at 125 μs .

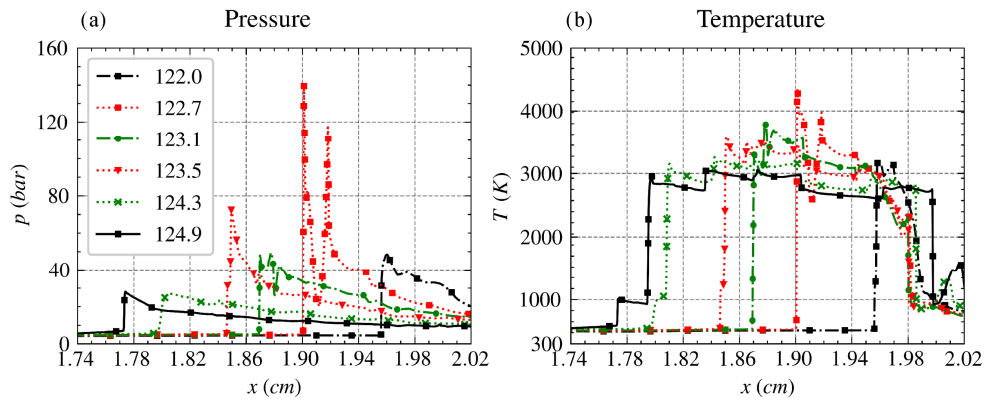


Figure 5-7. One-dimensional distribution of pressure and temperature along the bubble axis across the upstream flame fronts in RSBI Case 134-4 from 122.0 to 124.9 μs .

Figure 5-7 plots the pressure and temperature distributions across the upstream flame in RSBI Case 134-4 from 122.0 to 124.9 μs . From 122.0 to 124.9 μs , the flame is deflagration in the beginning (at 122.0 μs), then an extremely high-pressure peak presents at 122.7 μs . However, the transient peak pressure gradually drops, and finally (at 124.9 μs) at stable deflagration is observed. The whole process will be elaborately explained in Section 6.1.

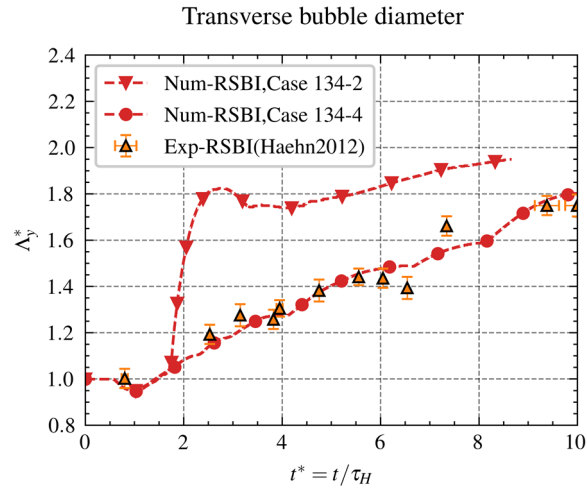


Figure 5-8. The nondimensional TBD values as a function of nondimensional time in this thesis and Haehn et al.'s experiment [88].

Apart from the flame structure discussions, the deflagration wave predicted by RSBI Case 134-4 can also be verified in Haehn et al.'s experiment [86]. Figure 5-8 compares the history of Λ_y^* predicted by numerical studies in this thesis and measured in the experiment. Generally, the TBD histories predicted by Case 134-4 overlaps well with experimental data, while significant discrepancies from experimental data are observed for Case 134-2 after $t^* = 1.8$. When $t^* < 1.8$, the TBD histories predicted by both grids overlap. After $t^* > 1.8$, the TBD values predicted by the coarser grids steeply increase and are much larger than the ones predicted by the denser grids. Notice that, for the early evolution of detonation wave in Figure 5-2, $t^* = 125/85.36 = 1.46$. Until this moment, though sustainable detonation wave has developed, it has no effect on the TBD value as it has not reached the equatorial interface. At $151 \mu\text{s}$ (presented in Figure 5-9), the TBD value begins to increase as the transverse bubble interfaces are accelerated by the detonation wave.

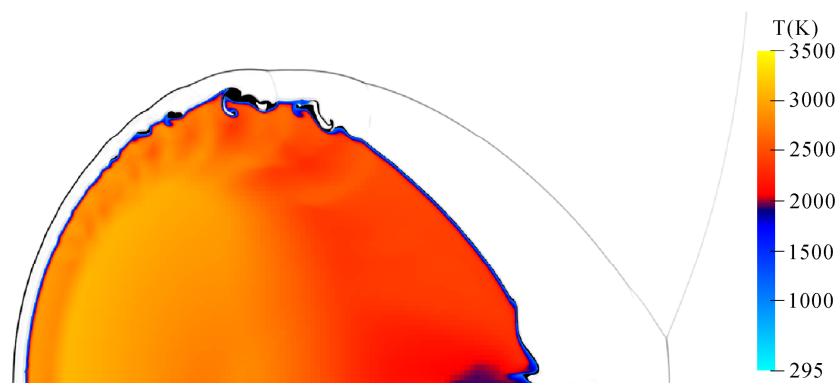


Figure 5-9. The temperature and numerical schlieren contour of RSBI Case 134-2 at $151 \mu\text{s}$. Only cells with $T > 1000 \text{ K}$ are shown.

5.2 Effects of AMR criterion for $M = 2.83$ case

Two cases with different AMR criteria are tested. Table 5-2 lists the AMR grid setups in Case 283-1 and 283-2. The grid setups in these two cases are shown in Figure 5-1 (a). For Case 283-1, the AMR criteria are based on hydrodynamic properties; while for Case 283-2, extra AMR criterion using Y_{OH} is considered.

Table 5-2. The initial grid setups around the bubble in the grid-convergence study of the RSBI at $M = 2.83$.

Case ID	minimum dx_0 (μm)	$L_{\text{hydro}} = L_{\text{chem}}$	AMR criterion using Y_{OH}	$dx_{\text{min}} = dx_{L_{\text{chem}}}$ (μm)
283-1	400	3	Off	50
283-2	400	3	On	50

5.2.1 Specific AMR criterion at ignition

The AMR grid is refined around discontinuity in the flow field. In Section 3.2.3, the discontinuity is estimated by the local relative variance of interesting flow properties. The recommended properties in the original work of ECOGEN [120] are ρ , p , T , and magnitude of velocity. The numerical studies in Section 4.1.4 prove this combination can capture shock wave, material interface, and flame front well. However, it cannot handle the ignition spot properly.

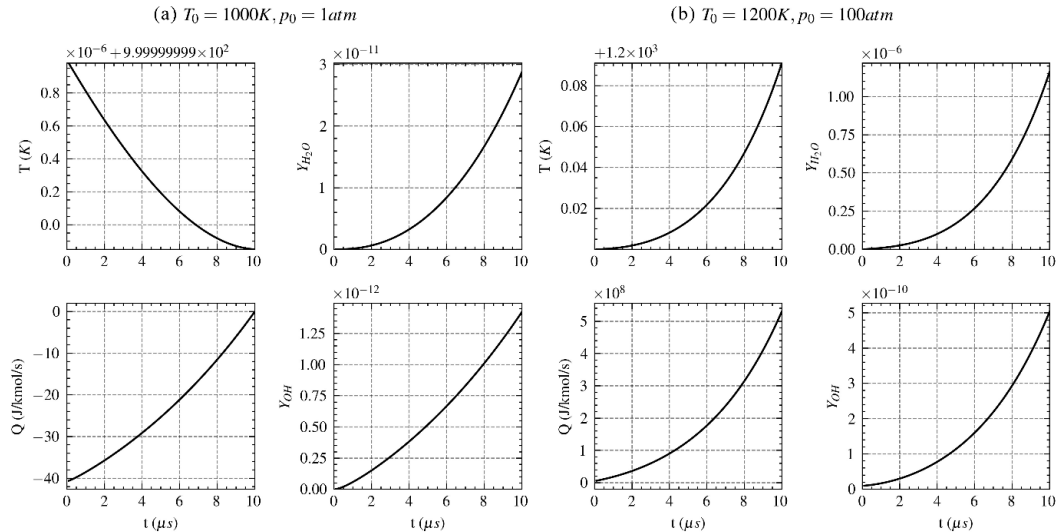


Figure 5-10. Ignition performance of 0th-dimensional ignition test. Initial condition: $X(\text{H}_2:\text{O}_2:\text{Xe}) = 2:1:3.76$, (a) $T_0 = 1000 \text{ K}$, $p_0 = 1 \text{ atm}$. (b) $T_0 = 1200 \text{ K}$, $p_0 = 100 \text{ atm}$. Q : heat release rate.

Let us take a quick look at the ignition process to see whether any AMR criterion based on the hydrodynamic properties can sense the ignition. Figure 5-10 presents results from two 0th-dimensional simulations with 2 sets of

initial temperature and pressure using the Ó Conaire H₂ combustion mechanism[60]. Initially, case (a) is similar to ignition at standard pressure and temperature, while case (b) imitates the ignition by shock focusing at high temperature and high pressure. Only 10 μs is simulated to emphasize the early ignition process. Notice that, for case (a) 10 μs is so short that the primary reactions are chain-initiating and endothermic. Hence, the heat release is negative and the temperature decreases. Contrastively, for case (b) the endothermic process is too short to be captured in this short temporal range. Hence, the heat release is positive, and the temperature increases. ΔT_{final} is the absolute difference between the initial and final temperature. For case (a), $\Delta T_{\text{final,a}} < 1\text{e-}6$ K, and in case (b) $\Delta T_{\text{final,b}} \approx 0.1$ K. The latter one is much larger as the chemical reaction rates are larger. However, even for the high-temperature, high-pressure case, to detect ΔT_{final} on the scale of 0.1 K, the refinement criterion shall be approximate $\xi = \frac{\Delta T_{\text{final,b}}}{T_{\text{ini}}} = \frac{0.1}{1200} \approx 8.33 \times 10^{-5}$, which is nearly 4 orders smaller than the recommended AMR criterion $\xi = 0.11$. Thus, additional AMR criteria must be evoked to detect ignition spots.

The properties of intermediate species are good candidates for ignition detection in combustion AMR study. In some AMR numerical detonation studies using a 1-step mechanism [77, 105], the gradient of reaction progress is the main factor in building the AMR criterion. In the current study, the local significant difference of Y_{OH} is chosen as a chemical-related criterion for ignition detection. This criterion is only applied to cells with distinct progress on combustion to avoid excessive grid refinement: referring to Figure 5-10, an empirical lower limit of combustion, $Y_{\text{OH}} = 1\text{e-}10$, is chosen in the current study.

5.2.2 Test on grid-convergence

In Diegelmann et al.'s numerical study [112] with incident $M = 2.83$, a 3-dimensional numerical study was performed with a grid resolution of 140 Pts/R. As presented in Section 4.3, a 3-level refinement grid with 50 Pts/R on root level is applied in this section. First, the AMR simulation is performed without considering Y_{OH} in grid refinement.

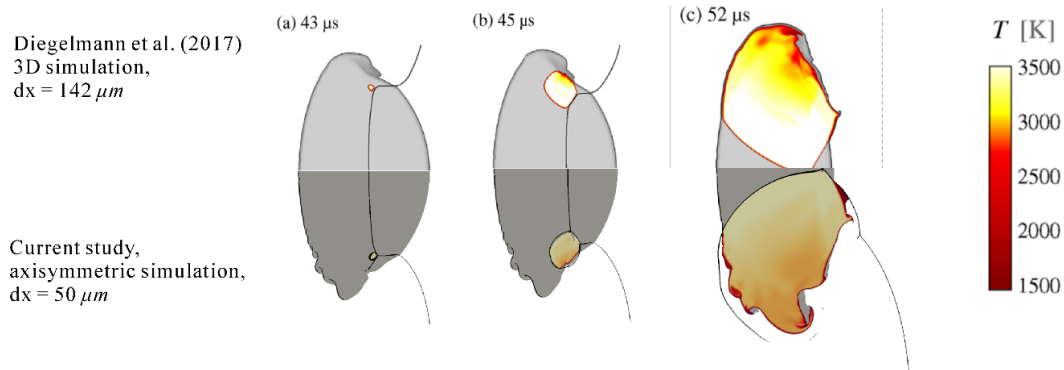


Figure 5-11. Temperature contour plots for Case 283-1 inside the bubble. The upper parts are results from Ref. [112], while the lower parts are results in the current AMR study.

Figure 5-11 presents the combustion flow field in Ref. [112] and in Case 283-1. The ignition at $43 \mu\text{s}$, detonation wave propagation at $45 \mu\text{s}$, and expansion of flame front at $52 \mu\text{s}$ are synchronously predicted at the same location. Though the inviscid reconstruction in Ref.[112], WENO-CU6, is much less dissipative than the MUSCL scheme in the current AMR solver, more small-scale flow structures are observed in the lower half as denser grids are applied. More unstable structures on the windward interface are detected in the current study at $43 \mu\text{s}$, and when the detonation wave transmitted through the upstream interface at $52 \mu\text{s}$, the evolution of formal unstable structure is poorly predicted in the upper parts. When the detonation wave approaching the axis, the current AMR method predicts a later arrival compared with the results in the upper half at $52 \mu\text{s}$. This difference may be attributed to the geometrical modeling as they performed 3-dimensional simulation, while here I perform an axisymmetric simulation to reduce the computational load.

These comparisons show that the axisymmetric configuration is good enough to produce the same combustion phenomena in the 3-dimensional configuration, and the current AMR method is again benchmarked by a published numerical RSBI study.

Generally, for the FVM method, numerical results predicted by dense grids are more physically reliable than those by coarse grids. Similarly, for the AMR method, denser grids produce better results, and the additional key point lies in the intelligent refinement criterion. As it is shown in Sec. 5.2.1, along with p , T , and ρ , additional evaluation of ζ relevant to Y_{OH} must be considered to detect ignition. Here the results with or without this special AMR treatment on ignition are compared.

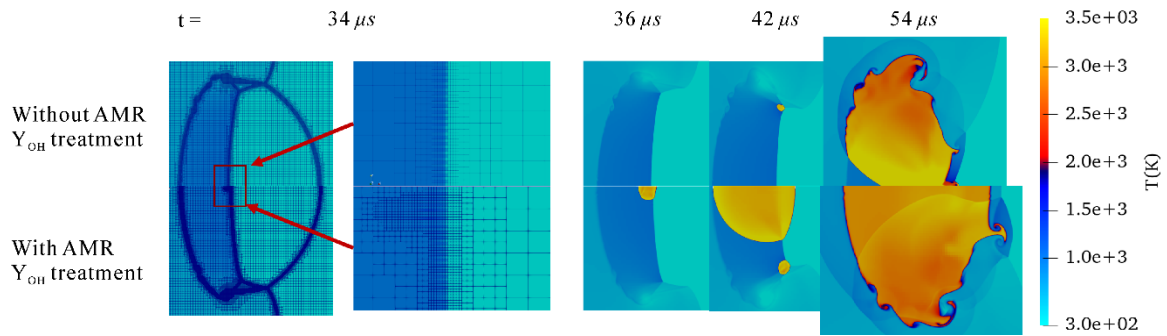


Figure 5-12. Temperature contour and AMR grids for reactive Cases 283-1 and 283-2. The AMR grids are plotted at $34 \mu s$ to show the different grids.

Figure 5-12 presents the temperature contour and AMR grids in Cases 283-1 and 283-2. The results with or without AMR criterion based on Y_{OH} are compared to show the performance of special AMR treatment on ignition. Different grids are observed at $34 \mu s$ at potential ignition spot near axis when apparent temperature rise is not detected: the grids on the upper half are only refined near the transmitted shock wave, while the grids on the lower half are additionally refined in the post-shock region. Later at $36 \mu s$, in the lower half, a hot flame is observed on the bubble axis near the transmitted shock wave. In contrast, no hot region presents on the upper half. At $42 \mu s$, both the upper and lower halves detect detonation at SFP which is present in Figure 5-11. In the lower half, the hot flame on the axis expands to a large volume. At $54 \mu s$, on the upper half, the detonation waves have met on the bubble axis. On the leeward interface and some portion of the windward interface, the detonation wave transmits to the surrounding N_2 gas and degenerates to shock waves. On the lower half, the detonation wave has swept through all portions of the bubble interface, and the bubble is fully burnt. This indicates that the fuels are all consumed, and a higher fuel consumption rate is observed in the lower one.

6. Two combustion modes in RSBI simulation

In this chapter, I demonstrate the different combustion modes in the RSBI study predicted by the Fire solver. In Haehn et al.'s RSBI experiments [86, 88], weak or strong combustion wave was detected in either lower or higher Mach number limit, yet they were not confident about the combustion type. These two combustion types will be verified as deflagration or detonation in this chapter by the RSBI simulation results with $M = 1.34$ and 2.83, respectively.

6.1 Deflagration wave in $M = 1.34$ case

Most numerical setups of this case are presented in Section 5.1. The grid convergence study shows convergent deflagration results are predicted by $dx = 2 \mu\text{m}$ in Case 134-4. The following analyses are all based on this case.

6.1.1 Numerical results

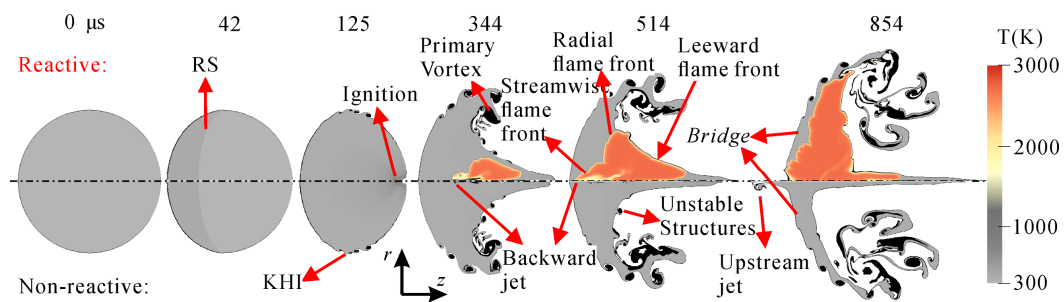


Figure 6-1. Temperature contours for the $M = 1.34$ RSBI (upper) and ISBI (lower) with limiting $Y_{Xc} > 0.1$. RS: refracted shock, KHI: Kelvin-Helmholtz instability

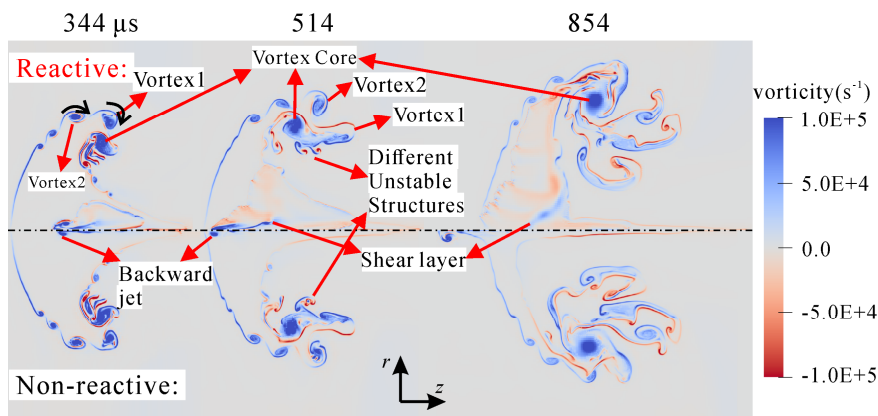


Figure 6-2. Vorticity contours for the $M = 1.34$ RSBI (upper) and ISBI (lower) at the later stage.

I first consider the non-reactive results in Figure 6-1 and Figure 6-2. In this shock-heavy-bubble interaction case with $At = 0.48$, at $42 \mu\text{s}$, the windward side interface triggers large-scale RMI and gets compressed. The

refracted shock (RS) travels slower than the incident shock and is convergent. At 125 μs , the velocity differences across the equatorial interface induce the secondary KHI. Shock focusing of the diffractive waves, which is not visible in this frame, occurs at the rear of the bubble and extrudes the downstream-pole interface inward. At 344 μs , the primary vortex, which is caused by the large-scale RMI, emerges near the equator, and small-scale structures, which are caused by the secondary KHI, appear on the leeward side interface. Figure 6-2 shows that shock focusing induces an obvious backward jet in the vorticity contour along the symmetry axis, and the jet propagation agrees with the “vortex ring projectile” in Zabusky and Zeng [30]. At 514 μs , the primary vortex grows, and the backward jet has nearly arrived at the upstream pole. In the last frame at 854 μs , the primary vortex further grows, with its radial boundary approaching the axis, and produces many mushroom-like RMI structures with positive and negative vorticities. The upstream bubble material connecting the counter-rotating vortices becomes thinner and was referred to as the “bridge” by Tomkins et al. [72]. The backward jet has now penetrated through the windward side interface to form an upstream jet.

The sequences in the upper halves of Figure 6-1 and Figure 6-2 show the development of the RSBI case. Before 42 μs , the bubble has not yet been ignited, and the inert and reactive flow fields are the same. In Figure 6-1, at 125 μs , ignition occurs due to shock focusing on the bubble’s downstream pole. The flame structures are on a scale of less than 1 mm and are later discussed in Section 6.1.4. At 344 μs , the flame grows inside the bubble, but the flame fronts have not yet interacted with the interface. The flame continues to expand until 514 μs , and here, we separate the flame fronts into three groups according to the orientations and denote them as the streamwise, radial, or leeward flame fronts. Compared with the ISBI case, the small-scale structures on the leeward side interface are damped by a baroclinic effect due to the pressure gradient and density jump across the flame [37, 90], and the bubble tail lies more downstream. Figure 6-2 shows the head of backward jet in the reactive case, which lies more upstream at 344 μs and slightly more downstream at 514 μs than the inert jet. At 514 μs , the pressure waves originated from combustion perturb the flow field, and different unstable structures are observed at the edge of primary vortex. Nevertheless, these pressure waves are too weak to affect other parts of the interface. At 854 μs , the flame consumes most unburnt mixtures in the bridge region, the streamwise flame front reaches the upstream interface, and the outermost radial flame front approaches the unburnt primary vortex. Compared with the inert case, the bridge region becomes thicker because of heat expansion, and the upstream jet disappears. The structures of the primary vortex, which are characterized by distributed bubble materials, are barely influenced by combustion. Therefore, the vortex core and the large-scale mushroom-like RMI structures seem to be the same

as those seen in the inert case. Figure 6-2 implies that the flame fronts generate extra vorticities inside the bubble, and a shear layer is located near the axis inside the flame.

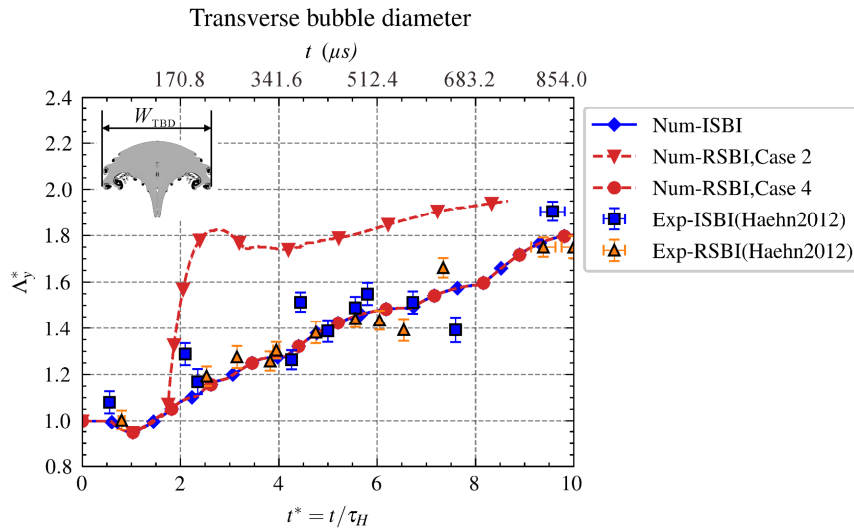


Figure 6-3. For the $M = 1.34$ case, the nondimensional TBD values as a function of nondimensional time in our simulation and Haehn et al.'s experiment [88].

Figure 6-3 plots the nondimensional TBD $\Lambda_y^* = W_{TBD}/2r$ as a function of nondimensional time t^* , in which W_{TBD} is the value of TBD. Most inert and reactive experimental data are effectively predicted by the simulations. In the time range in Figure 6-3, the flame fronts have not reached the equatorial interface, and the pressure waves caused by deflagration are very weak. Hence, the TBD history is not affected by the combustion and the results for both RSBI and ISBI overlap. Before $0.6\tau_H$, as the incident shock only compresses the windward side interface, the TBD values remain constant. After $0.6\tau_H$, the incident shock reaches the leeward side interface, and the TBD decreases due to the large-scale RMI effects. The TBD value reaches its minimum value at approximately τ_H . After that, the continuing increase is due to the growth of the primary vortex. The plateau at approximately $4\tau_H$, which is seen both experimentally and numerically, can be explained by the unsteady evolution of Vortex1 and Vortex2 from 344 to 514 μs in Figure 6-2; when the primary vortex rotates clockwise, since the movement of Vortex1 tends to decrease the TBD while the development of Vortex2 tends to increase it, the overall outcome is a plateau at approximately $4\tau_H$. After $4.1\tau_H$, since the spanwise movement of Vortex2 prevails, the TBD value increases. The later trends at $6.5\tau_H$ and $8\tau_H$ can be interpreted similarly. We also plot the TBD history predicted by the Case 2 simulation, and the detonation waves greatly increase the TBD values after $1.7\tau_H$. The overestimation of the experimental data further proves that the detonation obtained on coarse grids is not physical.

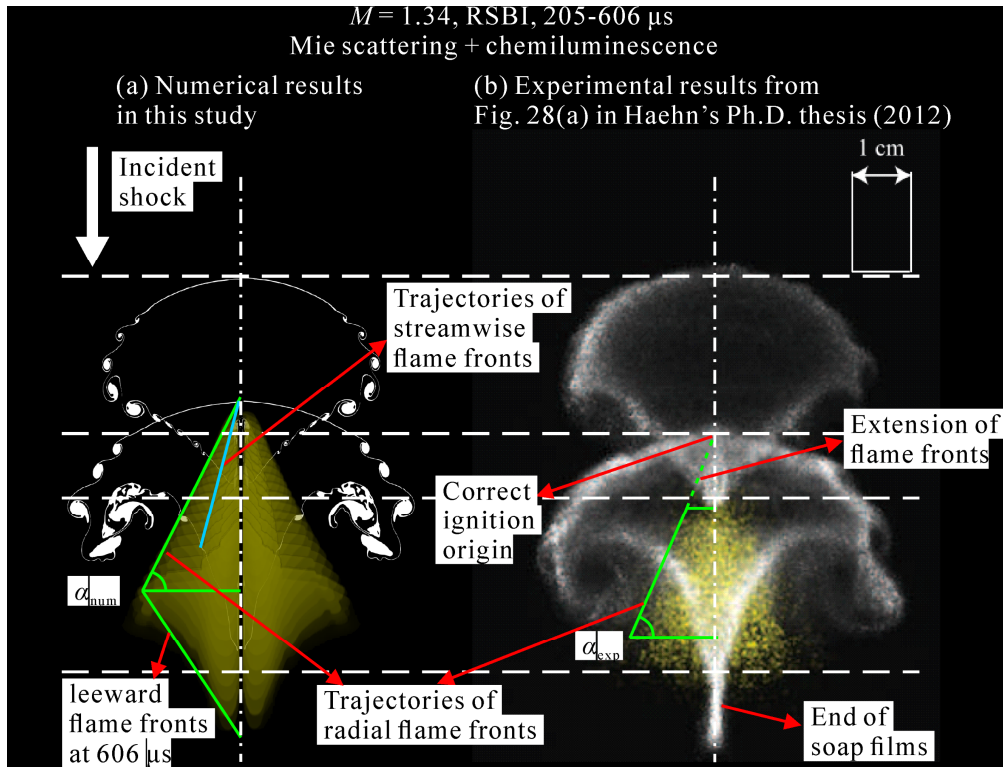


Figure 6-4. Combined images of the bubble morphology and combustion signals in the $M = 1.34$ RSBI case from 205–606 μs . (a) Our numerical results: the white solid lines represent bubble interfaces, and the yellow region is the superposition of the enhanced OH^* contour. (b) The experimental result from Ref. [86]. The dash-dotted white lines represent the symmetry axis.

Figure 6-4 shows the combined images of the bubble interfaces (white signals) and flame fronts (yellow signals). The bubble interfaces are experimentally captured by the planar Mie scattering method and numerically plotted as the iso contours of $Y_{\text{Xe}} \in [0.35, 0.55]$ instantly at 205 and 409 μs . The flame fronts are experimentally diagnosed by planar chemiluminescence from 409 – 606 μs , and numerically plotted as suppositions of instant OH^* distributions evenly sampled in the same time range. The numerical OH^* distributions are calculated using the quasi-steady-state assumption [94]. The dashed white lines mark the experimental locations of the bubble heads or tails, and the tails are regarded as the intersection of leeward interfaces instead of the ends of soap films to avoid interference. Since the experiment did not record the vertical locations, the best we can do is to vertically align the numerical and experimental bubble heads at 205 μs and plot the corresponding results at 409 μs . At 205 μs , both the numerical and experimental interfaces consist of a hemisphere on the windward side and a reversed cone on the leeward side, and the corresponding streamwise bubble lengths are almost identical. At 409 μs , both results show obvious primary vortex structures and small-scale unstable KHI structures similarly. Although both the numerical head and tail lie more upstream than the experimental head and tail, the streamwise length scale remains nearly the same. This observation indicates that numerically, the bubble travels less downstream, and the

dislocation is around 0.47 cm. This difference may be caused by the mass of the soap film bubble interface in the experiment. Table 6-1 shows the relative TBD error from Figure 6-4. Overall, the relative error of W_{TBD} is less than 9%.

Table 6-1. Lengths and angles in Figure 6-4

	t (μ s)	EXP	NUM	Relative Error(%)
TBD value	205	5.165 cm	4.704 cm	8.93
	409	6.118 cm	5.835 cm	4.62
α		23.54°	27.45°	15.76
$\cot \alpha$		2.295	1.942	15.41

The flame fronts in Figure 6-4 are outlined in solid green. In these two-dimensional images, the experimental result is an isosceles trapezoid, while the numerical results consist of a triangle and a reversed triangle. In general, the numerical triangular signal is consistent with the observation by Haehn et al. [88] at the lower Mach number limit. These numerical and experimental signals are explained as the superposition of the streamwise main flow and spanwise flame propagation. The trapezoidal shape in the experimental image may result from the failure to capture early ignition signals, and the correct origin of the flame front shall lie on the intersection of the extended flame fronts (dashed green line) and the symmetry axis (dash-dotted white line). With this correction, the ignition spot coincides with the bubble head at 409 μ s, which is precisely reproduced by the simulation. The numerical and experimental inclinations of the flame fronts are denoted as α_{num} and α_{exp} , respectively, and they can be used to evaluate the speed ratio between the flame fronts and the main flow $V_{flame}/V_{mainflow} = \cot \alpha$ [88]. Table 6-1 also compares these numerical and experimental angles and speed ratios, and the maximum relative error is less than 16%. The hypotenuse of the numerical triangular signature is the trajectories of the radial flame fronts, and the hypotenuse of the reversed triangular signature is the leeward flame front at 606 μ s. Since we neglect the soap film in the modeling, the numerical flame fronts are not damped by the water droplets [75, 126]; otherwise, better agreements would be achieved as the reversed triangular signals may disappear. Another interesting numerical finding is the trajectory of the streamwise flame fronts marked by the solid cyan line. These flame fronts are entrained by the backward jet. These numerical signals were not identified in the experimental work by Haehn et al. [88] due to the overlap with the radial flame front signals. Considering that the experiments were inevitably influenced by the interfacial perturbations and that the numerical deviations arise from the chemical mechanism and the neglect of the soap film, the unsteady bubble morphology and flame signature are, surprisingly, reproduced both qualitatively and quantitatively.

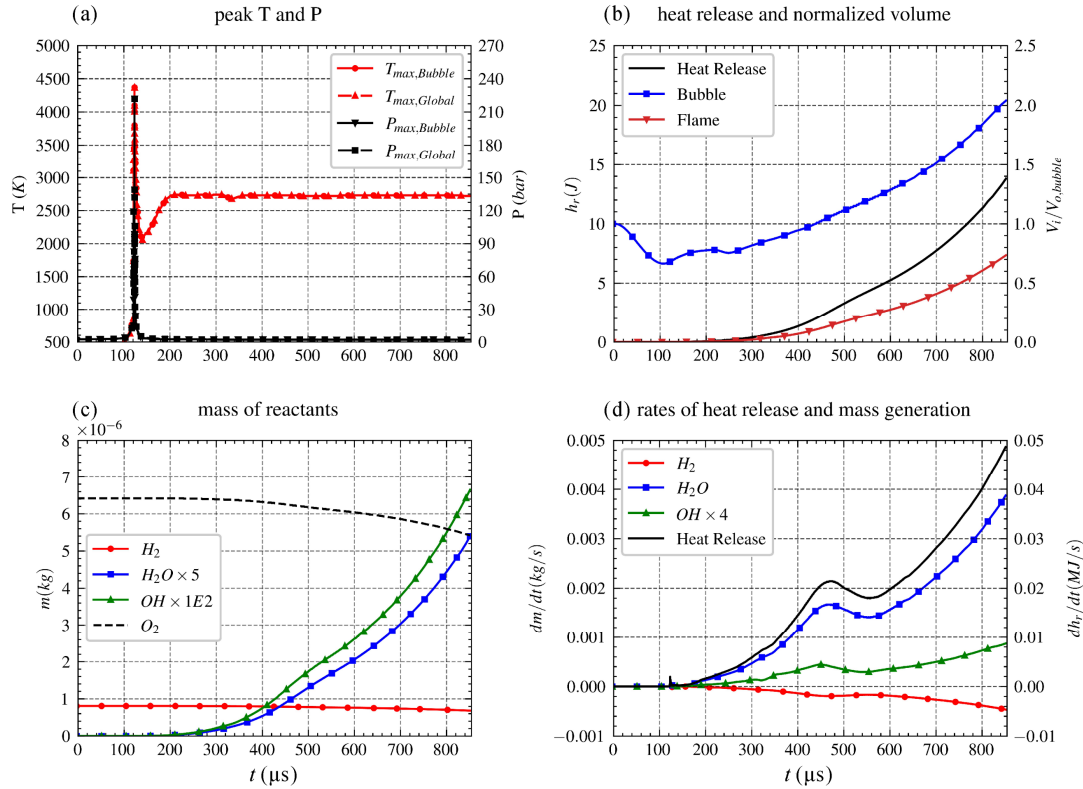


Figure 6-5. Instantaneous properties of the $M = 1.34$ RSBI case from 0 to 854 μ s: (a) peak temperature and pressure in the global flow field and inside the bubble, (b) heat release, normalized volume of the bubble, and burnt mixture, (c) mass of some reactants, and (d) rates of heat release and mass generation.

Figure 6-5 plots the global history of several thermodynamic or chemical properties during the simulation. Most of the time, the location with the maximum thermodynamic states lies inside the bubble. The peaks with $T_{max,bubble} = 4400$ K and $p_{max,bubble} = 223$ bar are detected at approximately 122 μ s when shock focusing occurs and quickly ignites the bubble. In Figure 6-5 (b), the volumes are normalized by the initial bubble volume $V_{0,bubble}$. The bubble volume declines before 100 μ s due to the shock compression and then varies non-monotonically because of the non-linear SBI evolution until 240 μ s. After 240 μ s, it increases continuously while the effects of the primary vortex dominate. Obvious heat release and flame expansion are detected only after 250 μ s. Figure 6-5 (c) and Figure 6-5 (d) indicate that the maximum fuel consumption rate (4.66×10^{-4} kg/s), which is observed at the end, is more than two times larger than the average rate (1.73×10^{-4} kg/s). Figure 6-6 presents the Y_{H_2} contour and can be used to explain the nonmonotonic behaviors of dm_{H_2}/dt from 400 to 700 μ s. The overall fuel consumption rate is caused by the collective effect of the upstream, radial, and leeward flame fronts. Since the leeward flame fronts arrive at the interface and are no longer accessible to the fresh unburnt premixtures after 470 μ s, dm_{H_2}/dt decreases despite the contributions from other flame fronts. After 560 μ s, the radial fronts continue stretching in

the bridge region. Considering the axisymmetric configuration, the fuel consumption rate is dominated by radial fronts and continues to increase.

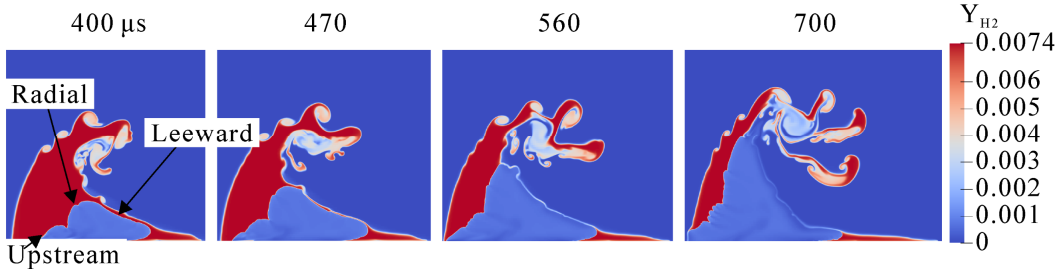


Figure 6-6. Y_{H_2} contours in the $M = 1.34$ RSBI case from 400 to 700 μs .

6.1.2 Effects of combustion on vorticity and mixing

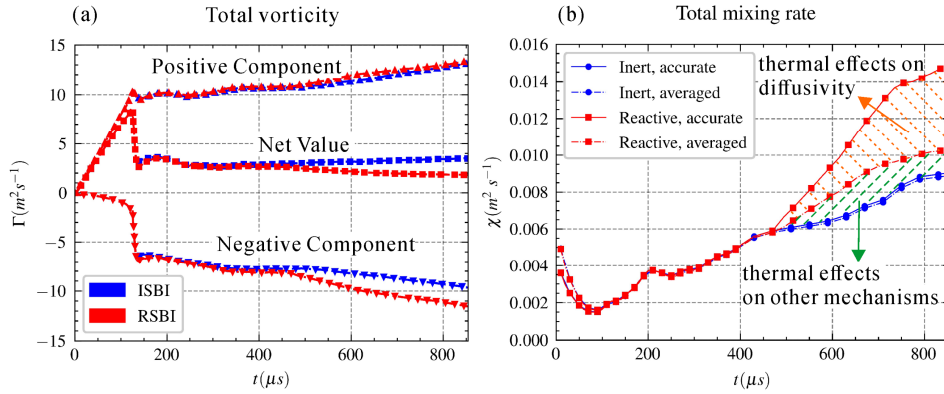


Figure 6-7. The history of (a) the vorticity and (b) the mixing rate in both the $M = 1.34$ ISBI and RSBI cases.

Figure 6-7 plots the vorticity and mixing rate in the ISBI and RSBI cases. The total vorticity is defined as $\Gamma = \int \omega dx dy$. To avoid the interference of combustion on the gradients of the reactive species, we examine the mixing behaviors between two inert species, N_2 and Xe , which are initially located either inside or outside the bubble. The mixing rate χ between N_2 and Xe is adopted from Tomkins et al. [72] as

$$\chi = \int D_{Xe,N_2} (\nabla Y_{Xe} \cdot \nabla Y_{Xe}) dx dy \quad (5.1)$$

where D_{Xe,N_2} is the binary molecular diffusivity.

Figure 6-7 (a) presents the total vorticity along with the positive Γ^+ and negative Γ^- components. For the ISBI case, the net vorticity is always positive. Before 122 μs , the magnitudes of Γ and both components monotonically increase: the magnitude of Γ^+ increases via the primary RMI effects and the magnitude of Γ^- increases via the secondary KHI effects. At 122 μs , the positive component drops slightly, and the magnitude of Γ^- drastically increases because of shock focusing. The net vorticity value also decreases. From 125 μs to the end, the incident

shock has already passed through the bubble. Therefore, the magnitudes of Γ^+ and Γ^- grow slowly. During the simulation, the Γ^+ values in both the inert and reactive case nearly overlap, but the long-term magnitudes of Γ^- in the RSBI case are larger than those in the ISBI case. Overall, before 470 μs , the Γ values in both cases are the same. After 470 μs , the Γ of the RSBI case is smaller as a result of the negative vorticities deposited on the flame fronts (see Figure 6-2).

Figure 6-7 (b) illustrates the history of the mixing rate χ . Tomkins et al. [72] proposed that the mixing rate in a shock-accelerated flow depends on several mechanisms, including the steepening of ∇Y_i through the straining effects and an increase in interfacial area due to the RMI and KHI effects. In this combustion study, apart from the thermal effects caused by the aforementioned two mechanisms, since the combustion drastically changes p and T , another mechanism arises according to Eq. (3.26), e.g., $D_{\text{Xe,N}_2} = D_{\text{Xe,N}_2}(p, T)$, and we refer to it as the thermal effects due to the diffusivity. To quantitatively evaluate the importance of these mechanisms, we compare both the “accurate” and “averaged” mixing rates: the accurate rate is obtained by numerically integrating Eq. (5.1), whereas the averaged rate is evaluated similarly but uses the averaged diffusivity $\bar{D}_{\text{Xe,N}_2} = D_{\text{Xe,N}_2}(p_1', T_1')$, where p_1' and T_1' are the post-shock pressure and temperature behind the incident shock, respectively. The incident shock fully passes the bubble at approximately 120 μs . Before 120 μs , the inaccuracy of the averaged χ results from the overestimation in $\bar{D}_{\text{Xe,N}_2}$ because the bubble is only partially compressed. After that, the accurate χ in the inert case can be effectively evaluated using $\bar{D}_{\text{Xe,N}_2}$. In the reactive case, the difference between the accurate and averaged χ , which is shaded by the dashed orange lines, represents the contribution related to the thermal effects on diffusivity. In addition, the difference between the reactive averaged χ and inert accurate/averaged χ , which is shaded by the dashed green lines, represents other contributions relevant to the concentration gradient and interfacial area. The inert accurate χ decreases before 90 μs as a result of the shock compression on the windward interface. From 90 to 210 μs , χ increases because of the small-scale interfacial structures caused by secondary KHI. The decrease from 210 to 250 μs can be explained by the competition between different mechanisms [72]: the increase in the interfacial area promotes the mixing rate but also smooths the concentration gradient, and sometimes the overall outcome is a decrease in mixing. After 250 μs , the primary vortex continues to develop and entrain the surrounding N_2 , which dominates the continuous increment of χ . The mixing behaviors of both the inert and reactive case before 470 μs are the same. After 470 μs , the flame fronts reach the leeward interface and promote mixing. At 700 μs , the reactive χ is approximately 83% larger than the inert one, in which

59% of the growth is related to the diffusivity and 41% is due to other mechanisms. The temporal integration of χ after 470 μs shows that combustion increases mixing by approximately 57%, in which 71% of the growth is related to diffusivity and 29% is due to other mechanisms. Therefore, in this study, combustion significantly promotes mixing in SBI, and the contributions primarily lie in the thermal effects on diffusivity.

6.1.3 Mach reflection transition in the ISBI

In this section, we analyze the Mach reflection transition process and the formations of two hot spots after shock focusing in the ISBI case. The flow field of interest is as the rectangular region in Figure 5-1 (b).

Figure 6-8 demonstrates the shock-focusing process from 116.8 to 121.0 μs in the ISBI case. At 116.8 μs , the curved incident shock (IS) propagates along the leeward side interface toward the symmetry axis. With a positive Atwood number, fast–slow refraction occurs between IS and the bubble interface (BI), which produces a refraction shock (RS2); besides, RS1 is caused by refraction at the windward side interface. A Type II shock-shock interaction, as discussed by Edney [6], occurs between RS1 and RS2, and the outcomes are two triple points (TPs), a nearly normal shock, and two transmitted shocks denoted by TS1 and TS2. Of these two shocklets, TS2 is strong, and TS1 is weak. Slow–fast refraction occurs between TS2 and BI, resulting in a secondary refracted shock (sRS) and a reflected shock (RfS). At 118.0 μs , the interaction between RS1 and RS2 reconfigures into a Type I shock-shock interaction. At 119.2 μs , we observe the cross of RS1 and RS2 without obvious interference. At 120.0 μs , RS1 reaches the downstream pole, and RS2 merges with other derived wave structures and is no longer distinguishable. At 120.6 μs , RS1 propagates through the downstream slow-fast interface, and the outcomes are a refracted shock (RS3) and reflected rarefaction waves. At the rear of the downstream pole, the sRS catches up with the IS and will collide with its reflection on the axis; this finding is a new explanation of shock focusing in complement with the collision of curved incident shocks [30, 43]. Meanwhile, the shocks inside the bubble merge near the downstream pole. At 121.0 μs , after the shock collision, a hot spot with a maximum temperature of approximately 1500 K is detected at the rear of the downstream pole. The shock collision generates two hot jets that propagate upstream and downstream. For the upstream jet inside the bubble, Mach reflection occurs, and the merged shock acts as the secondary incident shock (sIS).

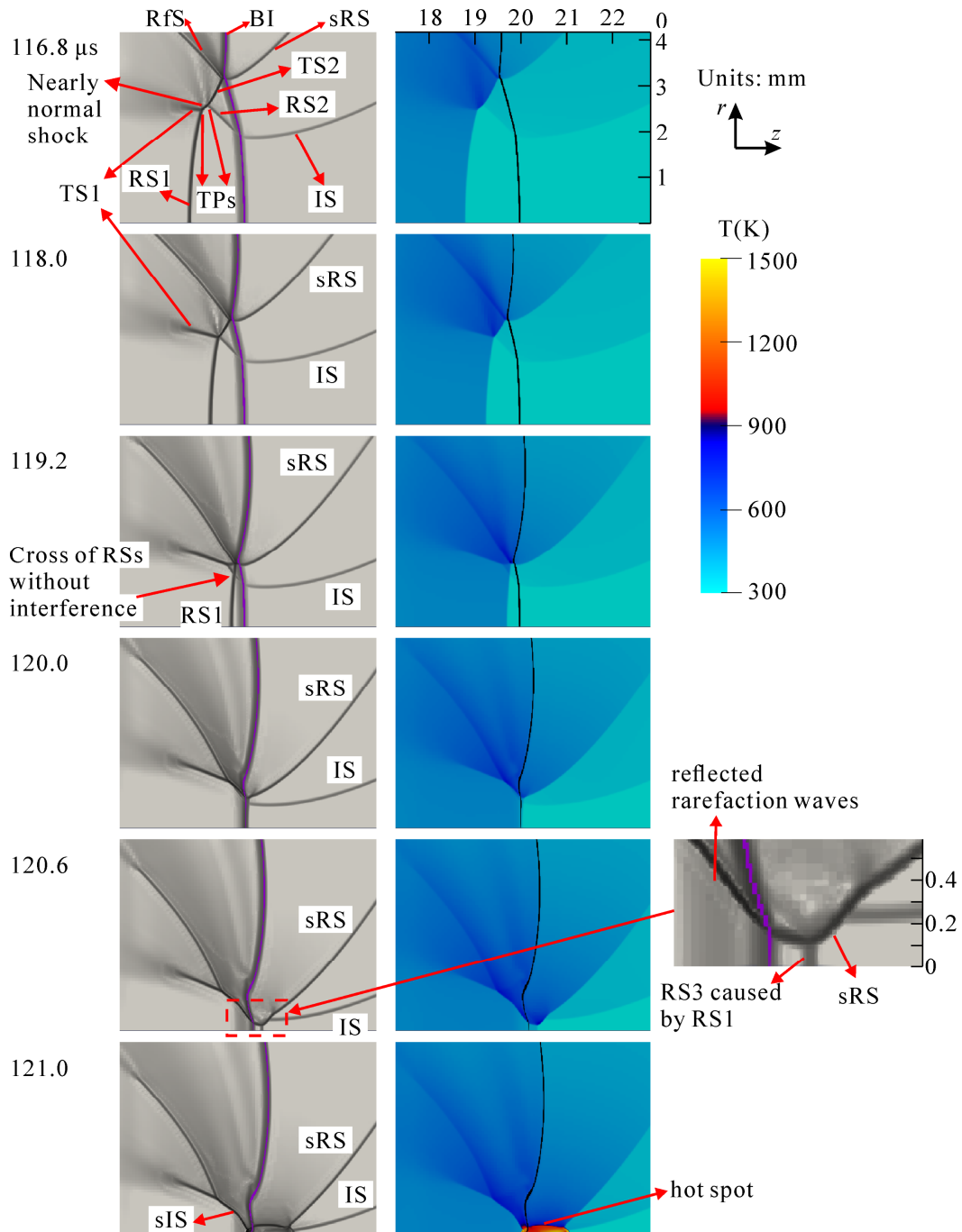


Figure 6-8. Numerical schlieren and temperature contours near the downstream pole in the ISBI case from 116.8 to 121.0 μs . BI: bubble interface, IS: incident shock, RS1, RS2: refracted shocks, RfS: reflected shock, sIS: secondary incident shock, sRS: secondary refracted shock, TS1, TS2: transmitted shocks, TP: triple point. The lower boundary in each frame coincides with the symmetry axis.

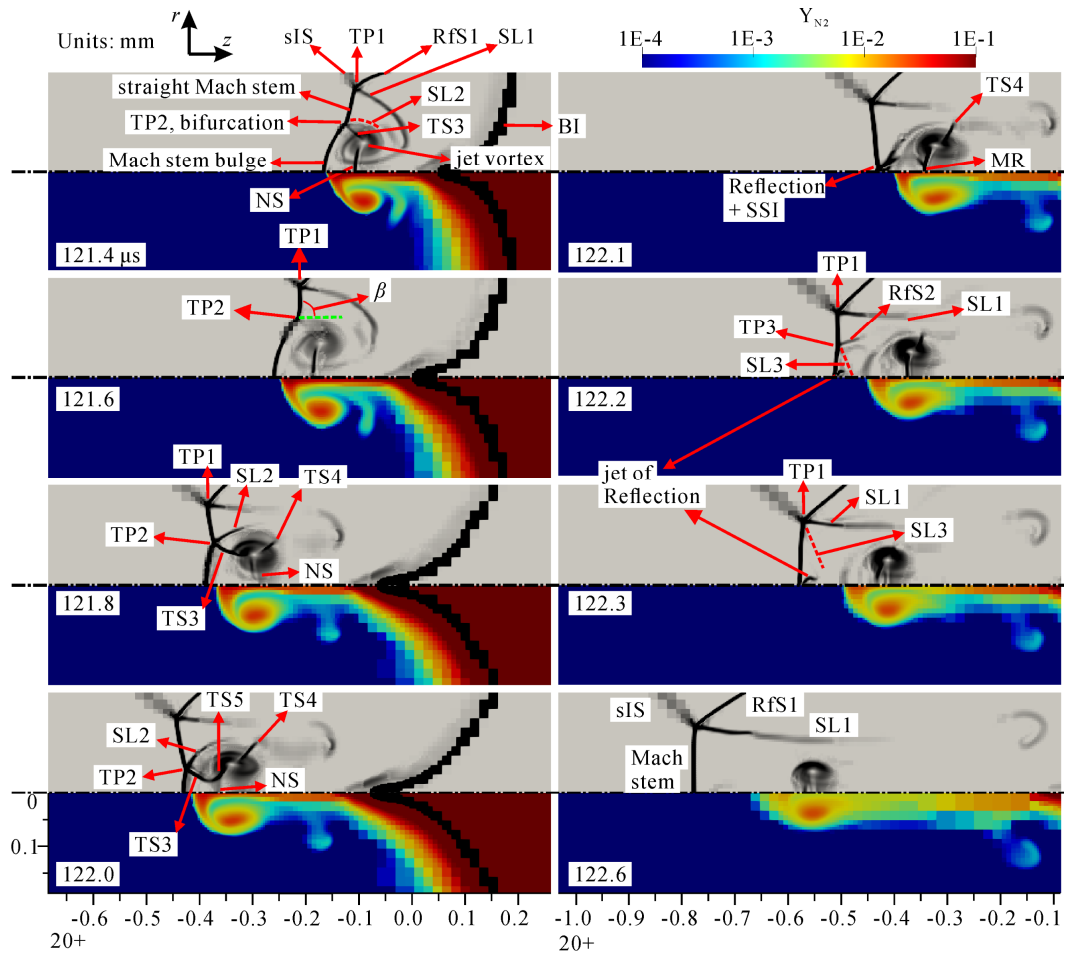


Figure 6-9. Sequences of numerical schlieren contours (upper regions) and Y_{N_2} contours (lower regions) during the Mach reflection transition in the ISBI case from 121.4 to 122.6 μs . MR: Mach reflection, NS: normal shock, SL: slip line, SSI: shock-shock interaction, TP: triple point, TS: transmitted shock. For the meanings of other symbols, please refer to Figure 6-8.

Figure 6-9 presents the Mach reflection transition from 121.4 to 122.6 μs . At 121.4 μs , although the main flow feature propagates to the right, the secondary incident shock (sIS) moves to the left. The sIS has a relatively poor resolution because it is colder than T_{et} , and the local grids are loosely refined. Hornung [43] pointed out that the SFP is indeed the cylindrical shock reflection phenomenon, and the outcome must be Mach reflection because of the Guderley singularity that arises from the cylindrically converging shocks [38]. Therefore, here, we observe a Mach stem, a reflected shock (RfS1), a triple point (TP1), and a slip line (SL1). Moreover, because of the strong backward jet, the Mach stem bifurcates into the upper straight Mach stem and the lower Mach stem bulge with a new triple point (TP2) [53, 56]. The Mach stem bulge is weaker than the straight Mach stem. To make the flows behind them mechanically equilibrium, a Type III shock-shock interaction occurs at TP2 and generates a transmitted shock (TS3) and a slip line (SL2, the red dashed curve) according to Edney [6]. In addition, a nearly

normal shock (NS) appears inside the jet to match the pressure behind the Mach stem bulge and in the jet flow, and the jet vortex entrains SL1 into the core.

In Figure 6-9, at 121.6 μs , since the temperature around TP2 drops below T_{et} , the disappearance of TS3 is possibly caused by insufficient grid resolution. Because TP1 travels faster than the Mach stem foot, TP2 gradually lies behind TP1; the inclination of the straight Mach stem, β , increases from a sharp incline (at 121.4 μs) to nearly 90° (at 121.6 μs) and later becomes obtuse. At 121.8 μs , the Type III shock-shock interaction reappears. TS3 further interacts with the normal shock (NS) in the backward jet and produces another transmitted shock (TS4). At 122.0 μs , as TP1 lies more upstream than the Mach stem foot, TP2 and TS3 approach the symmetry axis. A new transmitted shock (TS5) appears as a result of the interaction between TS3 and NS. Meanwhile, the jet vortex alters the local pressure distribution; this alteration reallocates TS4, which is no longer closely related to TS3 and NS. At 122.1 μs , TP2 collides with its reflection on the axis, and TS5 produces a Mach reflection (MR) downstream. During this collision of triple points, the waves connecting to TP2, including the straight Mach stem, TS3, SL2, and the Mach stem bulge, and they all reflect on the axis and cause strong shock-shock interactions. At 122.2 μs , the reflected shock (RfS2) that arises from the triple point collision interacts with the Mach stem and forms a triple point (TP3) and a slip line (SL3, the red dashed line). This reflection also induces a new jet behind the Mach stem. At 122.3 μs , RfS2 reaches SL1, the Mach stem becomes nearly straight, and SL3 now connects to TP1. After 122.3 μs , the new jet no longer affects the Mach stem, and the wave systems transit to a single Mach reflection.

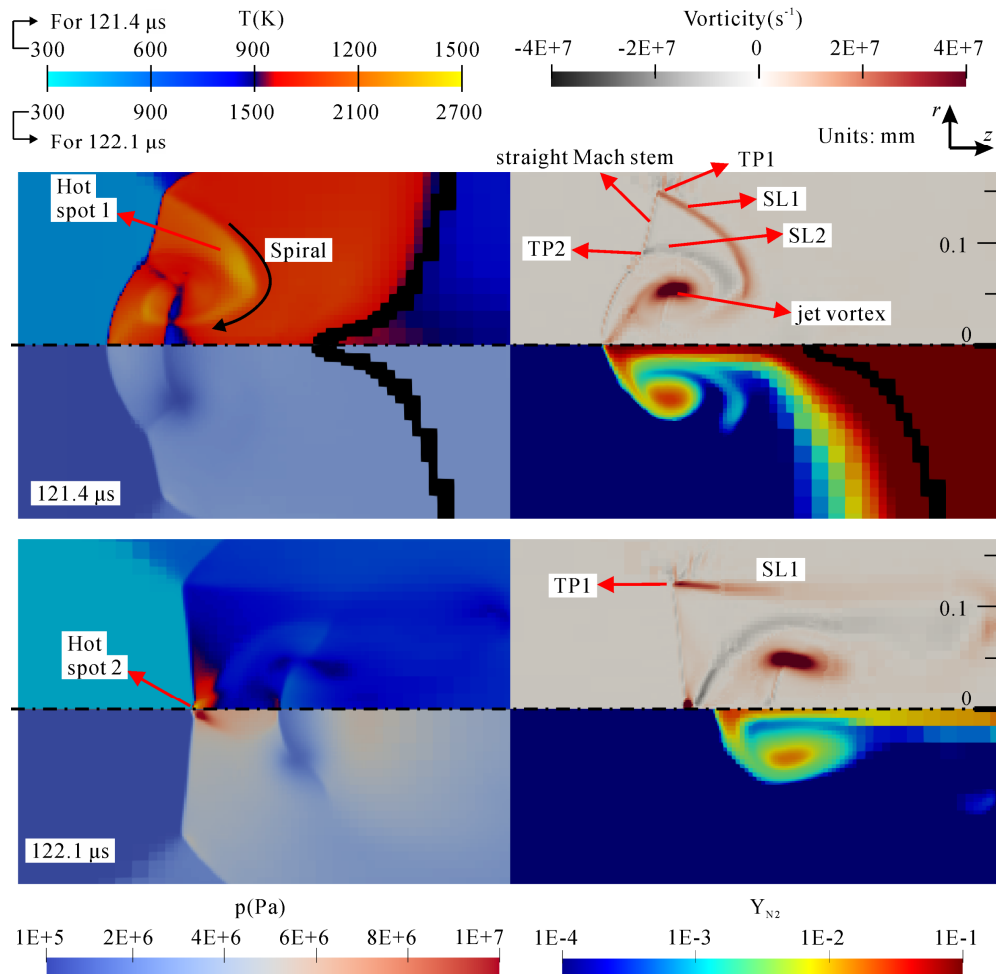


Figure 6-10. The formations of two hot spots in the ISBI case at 121.4 and 122.1 μs . The contour in each quadrant represents the (I) vorticity, (II) temperature, (III) pressure, and (IV) Y_{N_2} . For the meanings of other symbols, please refer to Figure 6-9.

Figure 6-10 illustrates the flow fields when two hot spots form in the ISBI case at 121.4 and 122.1 μs . At 121.4 μs , the backward jet propagates into the bubble and induces bifurcated Mach reflection. The jet vortex entrains the mixtures compressed by the straight Mach stem into the vortex core, which converts some kinetic energy into internal energy and further increases the temperature to approximately 1500 K. These form spiral hot spot 1. At 122.1 μs , the triple point collision includes complex shock-shock interactions on the axis, which leads to the formation of hot spot 2 at approximately 2700 K and 100 bar. The importance of this type of hot spot, which originates from the bifurcated Mach reflection and triple point collision, was verified by Bhattacharjee et al. [95] on detonation re-initiation and by Mahmoudi et al. [92] on flame propagation. Further analysis shows that the formation of these hot spots in both the inert and reactive cases are very similar, so the discussions here also apply to RSBI, and these two hot spots are responsible for the ignitions.

The possible causes of the Mach reflection transition are discussed here. Hornung [43] pointed out that Mach reflection with bifurcation is affected by the incident shock strength, reflected angle, and polytropic exponent. As the jet partly consists of lighter N_2 , it is very likely that the transition is influenced by the light-heavy refraction across the bubble interface as it changes these factors. This phenomenon should be further investigated using a simple geometry in the future.

6.1.4 Ignition and failure of DDT

In this section, I discuss two ignitions during the Mach reflection transition and the failure of DDT in the reactive case.

Ignition by the hot spiral in the jet vortex

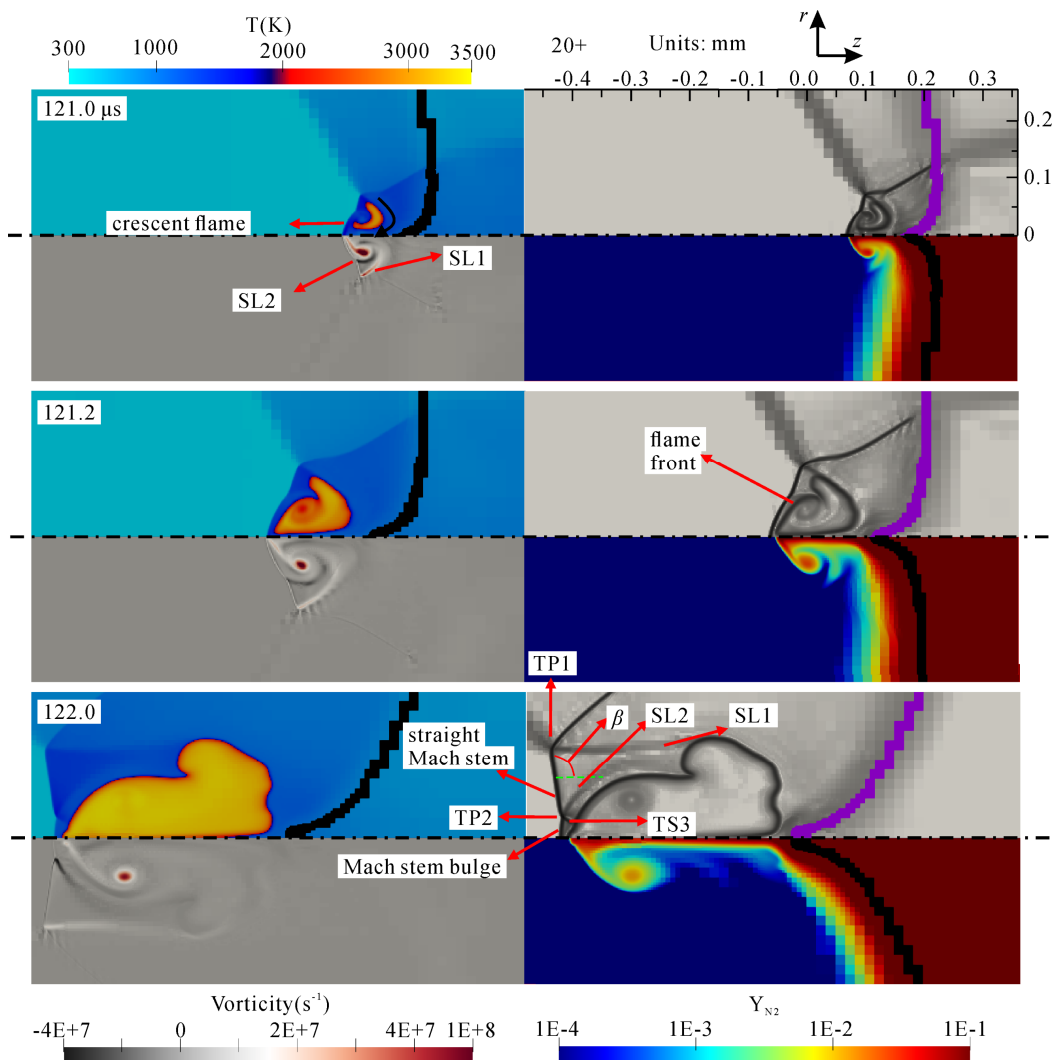


Figure 6-11. Sequences of the flow fields during the first ignition in the RSBI case from 121.0 to 122.0 μs. The contour in each quadrant represents the (I) enhanced numerical schlieren, (II) temperature, (III) vorticity, and (IV) Y_{N_2} . For the meanings of symbols, please refer to Figure 6-8 and Figure 6-9.

Figure 6-11 presents the flow fields during the first ignition from 121.0 to 122.0 μs in the RSBI case. At 121.0 μs , the premixtures are ignited by spiral hot spot 1 in the jet and produce the crescent flame. The backward jet is attached to the preceding Mach stem, but the flame fronts are decoupled from it. At 121.2 μs , the lower flame front gets entrained into the jet vortex core, and the upper flame front propagates along the slip line toward the straight Mach stem. At 122.0 μs , TP1 lies more upstream than the Mach stem foot, and a Type III shock-shock interaction occurs at TP2. The flame extrudes more horizontally near the axis because of the streamwise jet penetration. The temperature distribution inside the jet vortex is no longer inhomogeneous and implies that the reaction here is almost completed. Until this moment, the bifurcated Mach stem is almost the same as the inert stem. Therefore, the Mach reflection transition will occur in the RSBI case.

Figure 6-12 presents the flame development during the second ignition and failure of DDT in the reactive case. At 122.1 μs , the triple point collision produces hot spot 2 which is responsible for the second ignition. Since this collision occurs before the flame affects the flow field, the second ignition is not caused by the earlier jet flame through the diffusivity mechanism but is more related to the spontaneous ignition. The newborn flame fronts induce a bulge at the Mach stem foot. At 122.2 μs , which is not shown, the bulge interacts with the preceding Mach stem, and the results are a triple point, a reflected shock, and a slip line, and the interaction is similar to the inert case in Figure 6-9. At 122.3 μs , the reflected shock reaches TP1, SL3 now connects to TP1, and a portion of the newborn flame propagates along SL3 to TP1. The flame fronts are now fully decoupled from the preceding shocks, and the pressure field proves that the flame is deflagration. At 122.5 μs , the flame fronts reach SL1 and produce a refracted shock (RS4). Along SL3, the flame almost reaches TP1. The unburnt mixtures between the flame fronts and Mach stem are hotter than 1500 K. At 122.6 μs , the flame fronts interact with TP1, and this interaction produces a fast combustion wave that travels toward the axis with a speed of approximately 1050 m/s. This fast flame is due to the reactivity gradient in the hot unburnt premixture through the Zeldovich mechanism [13]. The upper portion of the Mach stem experiences a shock-flame interaction and turns into shear layer 1, but the lower portion is still decoupled from the flame. Near TP1, the mixtures between SL1 and RfS1 are ignited and deposit vorticities. From 122.7 to 122.8 μs , the Mach stem overlaps with the flame fronts. The fast combustion wave collides with its reflection on the axis and produces a jet vortex, a triple point (TP3), and a slip line (SL4, the red dashed line in the schlieren contour). The interaction between the flame and TP1 produces a train of weak pressure waves between the leftmost flame fronts and shear layer 1. The averaged pressure ratio across these pressure waves is about 1.02, and the leading wave perturbs the flame front and induces shear layer 2. At 122.8 μs , SL4 collides with shear layer 2, which amplifies the perturbations on the flame front. The Mach stem still

overlaps with the flame fronts. At 122.9 μs , transverse instabilities develop on the flame fronts, and the lower portion of the Mach stem becomes decoupled from the flame fronts.

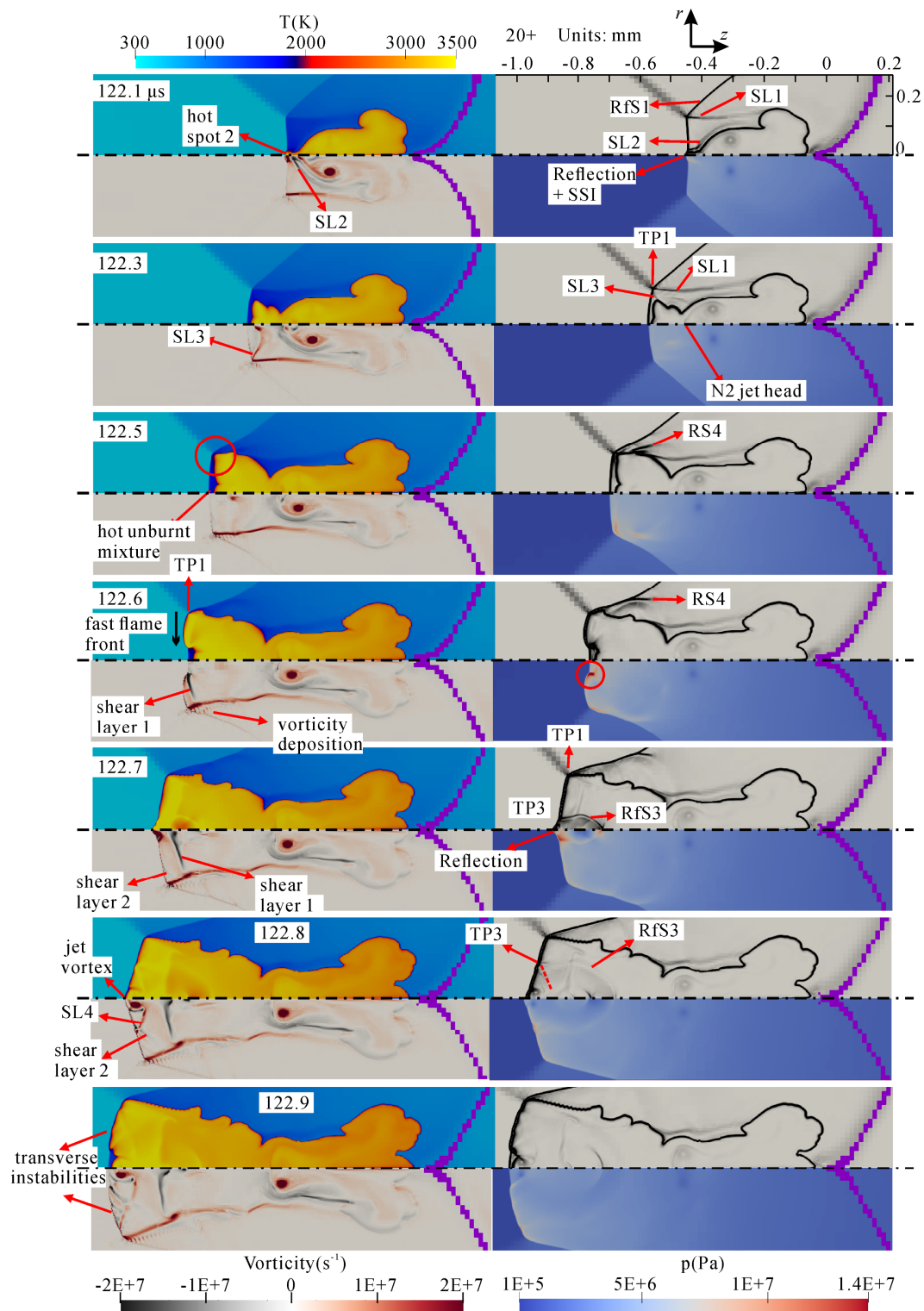


Figure 6-12. Sequences of the flow fields during the second ignition and failure of DDT in the RSBI case from 122.1 to 122.9 μs . The contours in each quadrant represent the (I) numerical schlieren, (II) temperature, (III) vorticity, and (IV) pressure. For the meanings of symbols, please refer to Figure 6-8 and Figure 6-9.

Figure 5-7 plots the one-dimensional upstream flame structures on the symmetry axis after the second ignition. From 122.0 to 124.9 μs , the second ignition induces complex three-dimensional shock-flame interactions that are responsible for the extreme peak pressure value (such as 140 bar at 122.7 μs). The flame fronts are decoupled from the preceding shock at 123.1 μs but attach to it again at 123.5 μs . Examinations of flow fields show the later attaching, and the formation of a pressure peak can be interpreted similarly to the collision of fast flame fronts on the axis in Figure 6-12. Since the later peak value is more benign than those at 122.7 μs , no detailed analysis will be presented. Although the flame fronts tend to accelerate, the DDT process eventually fails. The Mach stem is fully decoupled from the flame, and stable deflagration is maintained after 124.3 μs .

The influences of combustion on compression wave structures are also worth discussing. At 121.2 μs , the flame in the hot spiral alters the local sound speed, which destroys the normal shock wave in the backward jet and the later complex shock system shown in Figure 6-9 at 121.8 μs . Additionally, the TS3 from the Mach stem bifurcation is damped by the near flame front. At 122.1 μs , the downstream Mach reflection of TS5 disappears in the hot jet. After 122.1 μs , the second ignition and fast combustion wave strongly influence the Mach reflection structure by interfering with TP1, SL1, and the preceding Mach stem.

The flame instabilities are caused by the shock-flame interactions or slip-line-flame interactions. In Figure 6-12, at 122.3 μs , the flame fronts of the second ignition are perturbed by SL3. After the flame front interacts with SL1, at 122.6 μs , a corrugated flame with two sets of peak and valley structures becomes apparent. At 122.7 and 122.8 μs , these corrugated flame fronts are further perturbed by the shear flow and baroclinic torque caused by the RMI effects. The small-scale instabilities on the flame near TP1 are possibly numerical and originate from using rectangular grids to approximate the curved flame front, as suggested by Shen and Parsani [110]. At 122.9 μs , significant transverse instabilities are present on the leftmost flame fronts. These instabilities are due to the interaction between flame fronts and transverse waves, including RfS3 and weak pressure waves, as a result of the RMI effects.

6.2 Detonation wave in $M = 2.83$ case

6.2.1 Numerical results

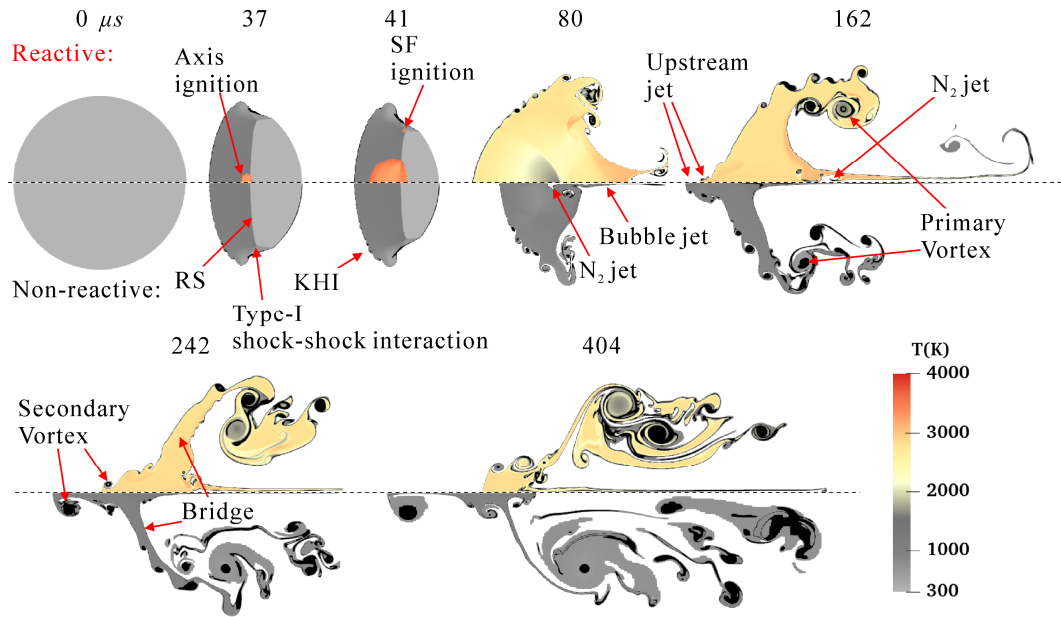


Figure 6-13. Temperature contours for $M = 2.83$ RSBI (upper) and ISBI (lower) with limiting $Y_{Xe} > 0.35$ (for frames other than $404 \mu s$) or $Y_{Xe} > 0.1$ (only for $404 \mu s$).

Figure 6-13 presents the temperature contour of $M = 2.83$ results in both reactive and non-reactive cases. For reference, the hydrodynamical time scale is $\tau_H = 40.4 \mu s$ and these cases cover $10\tau_H$.

Let's first consider the non-reactive case. At $37 \mu s$, the incident shock transmits into the bubble, and a Type-I shock-shock interaction occurs. After shock focusing at $80 \mu s$, a backward N_2 jet travels upstream due to the Mach reflection, and a bubble jet travels downstream. Primary vortex starts developing with bubble mass shedding near the equator. At $162 \mu s$, the backward jet protrudes through the windward bubble interface and forms an upstream jet. The primary vortex grows in both width and length. At $242 \mu s$, the upstream jet develops into the secondary vortex (SV), the bridge gets thinner, and primary vortex becomes more distributed. At $404 \mu s$, the inert SV on the upstream is almost separated from the main bubble material.

In the reactive case, axial ignition is detected on the intersection between the convergent shock and the bubble axis at $37 \mu s$. A simple 1D slap simulation shows that the IDT is more than $100 \mu s$ which is about 3 folds of the IDT in this simulation. Thus, the mildly convergent RS here shortens the IDT. At $41 \mu s$, the flame of axial ignition expands, and another ignition which is marked as SF ignition emerges at the triple point of the Type-I shock-shock interaction. Notice that both these two ignitions are caused by shock-focusing, as the heavy bubble acts as an acoustic lens to deflect the RS once it enters the bubble. Though in previous literatures, such as Ref.[80] and Ref.[88], the shock focusing is more frequently referred to as the shock-converging process near the downstream pole. At this moment, the flame fronts have not perturbed the bubble interface yet. At $80 \mu s$, the backward jet is suppressed by the detonation waves and disappears. The bubble is fully ignited and filled with high-temperature

gas, and the bubble head lies more upstream than the non-reactive one due to thermal expansion. At 162 μs , the upstream jet and primary vortex structures also present. The downstream pole of the reactive case is characterized by the N_2 jet and a long curved thin tail of bubble gas. The head of reactive bubble, once lies more upstream than the inert one, now lies more downstream, and the reactive upstream jet is smaller. At 242 μs , SV is observed near the windward interface. The primary vortex connects with the material on the axis by the bridge, and the reactive bridge structure is thicker than the inert case due to thermal expansion. At 404 μs , the reactive SV is more closely connected to the major bubble structures than the inert case.

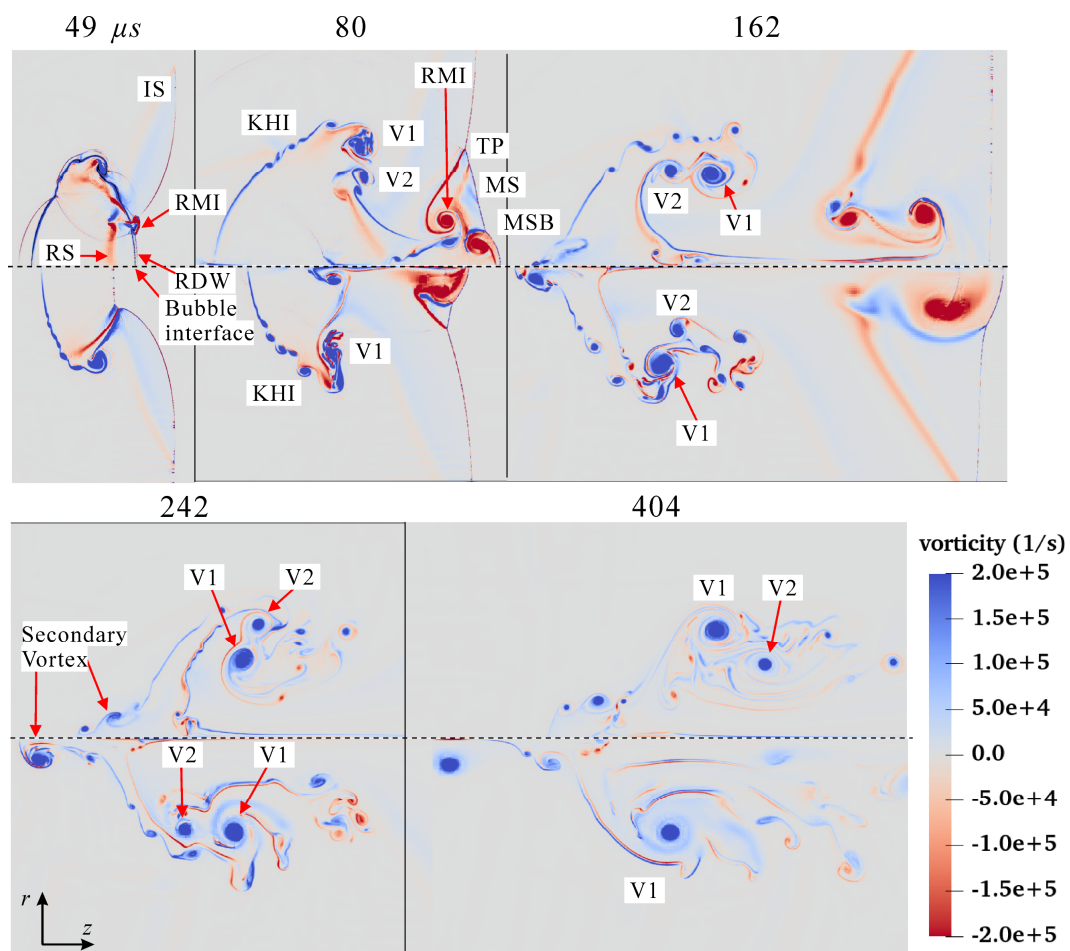


Figure 6-14. Vorticity contours for the RSBI (upper) and ISBI (lower). MSB: Mach stem bulge, V1 and V2: vortex.

Figure 6-14 presents the vorticity contours of the $M = 2.83$ RSBI and ISBI cases. At 49 μs in the reactive case, the detonation fronts of axis ignition and SF ignition interact with the refraction shock wave (RS) and bubble interface. The outcomes are complex wave structures: along the bubble axis, the detonation wave transmits across the leeward side interface. Eventually, the refracted detonation wave (RDW) degenerates into the shock wave. Also, the detonation waves interact with the incident shock (IS) and the bubble interface, the outcome is a pair of

counter-rotating vortex, which is more obvious at $80 \mu\text{s}$, which is a typical RMI phenomenon. At $80 \mu\text{s}$, KHI structures are found on the windward side interface due to the baroclinic gradient. As the detonation wave cancels the previously deposited vorticities, the KHI structures in the reactive case are much smaller than the inert ones. The primary vortex, V1, is found in both cases. Additionally, the shock system in reactive cases induces a secondary vortex, V2, on the leeward side interface. At the downstream region, typical waves of Mach reflection such as Mach stem (MS), Mach stem bulge (MSB), and triple point (TP) are observed in both cases. However, the causes of Mach reflection in the two cases are quite different: in the inert case, the Mach reflection is due to the diffracted incident shock, which is well explained in Section 6.1.3; while in the reactive case, it is caused by the shock system branched from the RDW. At $162 \mu\text{s}$ in the inert case, the secondary vortex, V2, gets born from the primary vortex, which is different from the reactive case. At $242 \mu\text{s}$, the secondary vortex caused by the upstream jet emerges at the upstream pole. From 162 to $404 \mu\text{s}$, in the reactive case, the V1 and V2 are entrained by the primary vortex and are still distinctly observed at the final moment. While in the inert case, V2 gradually merges with V1 and eventually disappears. The different behaviors of V2 in these two cases may be related to their different originations.

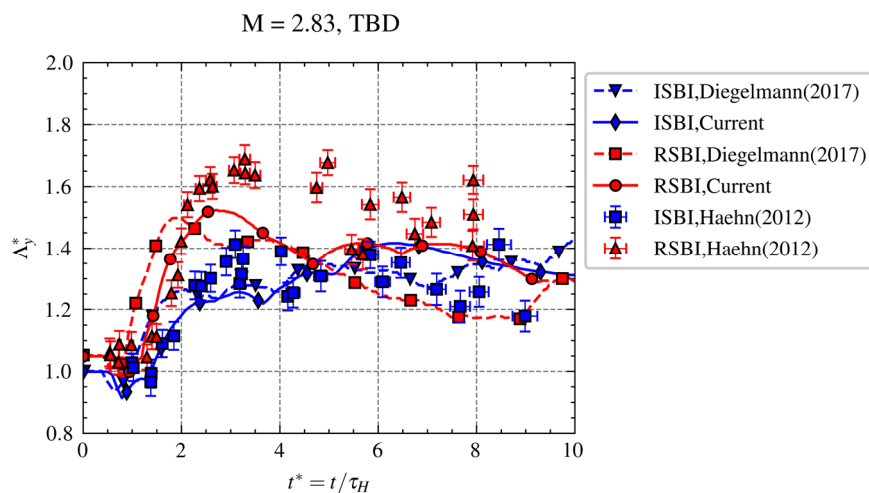


Figure 6-15. The nondimensional TBD values as a function of nondimensional time for $M = 2.83$ cases. The experimental results in Ref.[88], numerical results in Ref.[112] and numerical results in the current thesis are plotted.

Figure 6-15 presents the unscaled TBD value Λ_y^* against the unscaled time t^* of the $M = 2.83$ cases. The results in the current thesis, the experiment by Haehn et al. [88], and the simulation by Diegelmann et al. [112] are plotted. Noted that, the agreements between the simulation and experiment in Fig.18 of Ref.[112] is incorrect as the experimental data are wrongly plotted. For details, please refer to Appendix A.3. For the reactive cases in Figure

6-15, considering the effects of perturbation in initial bubble diameter [112], the data of reactive Case 283-2 are corrected by multiplying 1.05.

For the inert case, when $t^* < 2$ and $4 < t^* < 6$, current numerical results match well with the experiment. When $2 < t^* < 4$, current numerical results can only match with the lower limits of the experimental data. When $t^* > 6$, the experimental history of Λ_y^* are all underestimated by the simulation. Though the agreement only shows for the $t^* < 4$, a large portion of the deviations shall be subjected to the experimental uncertainties which are especially significant at $t^* = 3.2$. Compared with the numerical ISBI results reported in Ref.[112], the performance of the current simulation at the early stage ($t^* < 2.0$) is much better. Also, their simulations underrate Λ_y^* when $2 < t^* < 4$ yet shows better performance when $6 < t^* < 8$.

For the reactive results in Figure 6-15, before $t^* < 2$, the experimental results are well predicted by the numerical results of Case 283-2. When $2 < t^* < 5.5$, both case underpredicts the Λ_y^* values. The experimental peak Λ_y^* is around 1.7 and occurs at $t^* = 3.25$, while the predicted peak value is only 1.52 and is found at $t^* = 2.7$. Experimentally after $t^* = 3.25$, Λ_y^* slowly decreases and equals around 1.60 at $t^* = 4.7$. However, Λ_y^* value decreases much faster in simulation, and at $t^* = 4.7$, $\Lambda_y^* = 1.35$ which is much smaller than the experimental results. The trends of the Λ_y^* history can also be explained by the vortex development, which has been discussed in Section 6.1.1. After $t^* = 5.5$, considerable experimental uncertainties also present in the reactive case: Λ_y^* varies from 1.36 to 1.52 when $t^* \approx 5.7$, and varies from 1.41 to 1.62 when $t^* \approx 7.9$. Except for the experimental uncertainties, another possible explanation is that these data reveal two different combustion behaviors. However, the experimental results are too limited to validate the second explanation. Compared with the numerical results in Ref.[112], the results in the current work match much better with the experiment, particularly when $t^* < 2.0$. Although both numerical results predict low peak values of Λ_y^* , current simulation provides a higher prediction with less deviation from the experiment both in magnitude and temporally. In addition, compared to the valley in experimental occurs at $t^* = 5.7$, the valley in the current results, which occurs at $t^* = 4.6$, agrees much better than the valley predicted by Ref.[112] which occurs at $t^* = 2.7$.

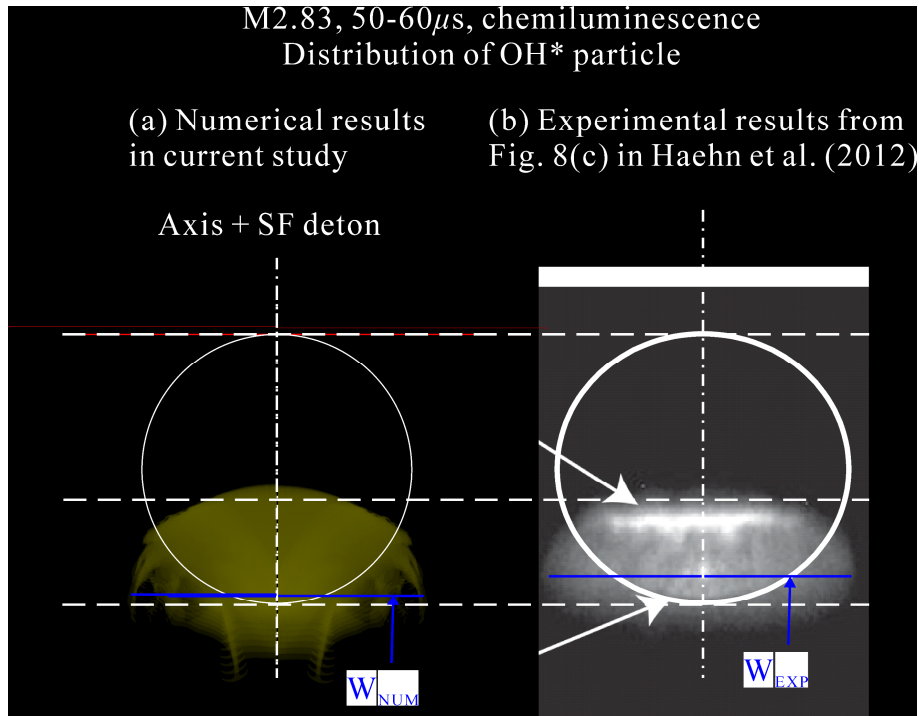


Figure 6-16. Combined images of the bubble morphology and combustion signals in the $M = 2.83$ RSBI case from 50–60 μ s. (a) Our numerical results: the white solid lines represent initial bubble interfaces, and the yellow region is the superposition of the enhanced OH* contour. (b) The experimental result from Ref. [88]. The dash-dotted white lines represent the symmetry axis.

Figure 6-16 shows the composite images of the bubble morphology and flame in $M = 2.83$ RSBI cases from 50 to 60 μ s. In subfigure (a), the numerical chemiluminescence is plotted by the same methods as Figure 6-4 and results are from the double detonation shown in Case 283-2. The numerical combustion signals are roughly in the same shape as the experimental ones, and the latter one is trapezoidal. The ratio of the width of these signals is around $W_{\text{NUM}} / W_{\text{EXP}} = 97.9\%$, which implies excellent agreements between this simulation and the experiment.

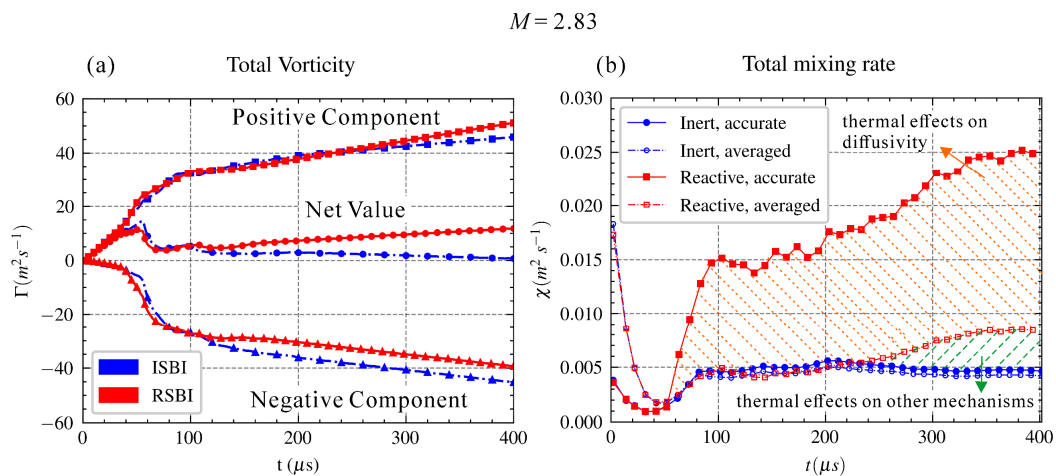


Figure 6-17. The history of (a) the vorticity and (b) the mixing rate in both the $M = 2.83$ ISBI and RSBI cases.

Figure 6-17 compares the vorticity and mixing rate in the $M = 2.83$ ISBI and RSBI cases. These properties are defined in Section 6.1.2. In the ISBI case before $55 \mu\text{s}$, the magnitudes of both Γ^+ and Γ^- increase due to the incident shock and secondary KHI structures, and the net total vorticity is positive. From 58 to $85 \mu\text{s}$, the Γ^+ magnitude changes little, but Γ^- magnitude increases much faster due to shock focusing near the downstream pole and the subsequent Mach reflection, and Γ decreases. After $85 \mu\text{s}$, the positive component keeps increasing and the negative component keeps descending. The value of Γ firstly decreases after $58 \mu\text{s}$, then after $80 \mu\text{s}$, the declining rate decrease and Γ gradually approaches 0 in the end. For the reactive case, the general trend of the vorticity history is similar to the non-reactive case. The main difference lies in the negative vorticity after $120 \mu\text{s}$, as the detonation waves alter the SBI wave systems and vorticity field drastically (see Figure 6-14). After $120 \mu\text{s}$, the magnitude of Γ^- in the reactive case is smaller, but Γ^+ is only mildly different from the inert case. Thus, the Γ for the reactive case is larger than the inert ones. Finally, $\Gamma = 12 \text{ m}^2\text{s}^{-1}$ in the reactive case.

In Figure 6-17 (b), for the inert case, in the beginning, decreases as the interface area decrease due to shock compression. Similar to the analyses in Section 6.1.2, the increment of mixing rate in the reactive case is separated into the contribution of diffusivity and other mechanisms. After around $50 \mu\text{s}$, the detonation waves drastically increase the mixing rate. Comparing with the inert case, the mixing rate in the reactive case increases around 270% from 0 to $10 \tau_{\text{H}}$, and around 94% of the increment is due to the thermal effects on diffusivity, and only 6% is due to the contribution of the gradient of mass fraction and interfacial area.

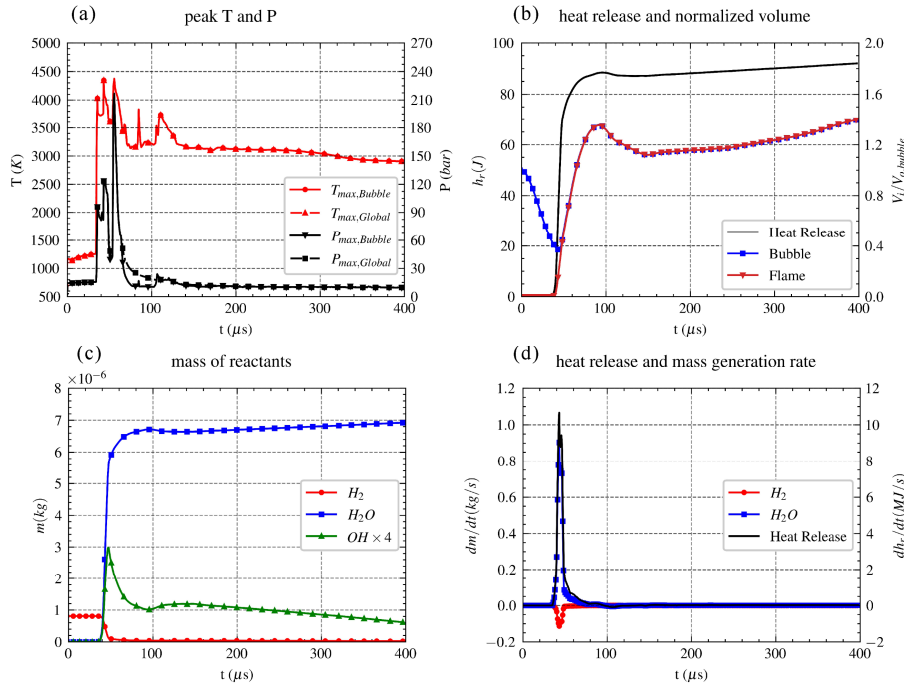


Figure 6-18. Instantaneous properties of the $M = 2.83$ RSBI case from 0 to 400 μ s: (a) peak temperature and pressure in the global flow field and inside the bubble, (b) heat release, normalized volume of the bubble and burnt mixture, (c) mass of some reactants, and (d) rates of heat release and mass generation.

Figure 6-18 presents the history of some reactive properties in the Case 283-2 case from 0 to 400 μ s. In subfigure (a), the peak temperature inside or outside the bubble is always the same. This shows that during the whole simulation, the cell with peak temperature always lies inside the bubble. Figure 6-19 presents the flow field of at 98 μ s. At this moment, the bubble is fully ignited. Figure 6-19 (a) shows that the detonation waves transmit through the windward side interface and degenerate to shock waves interacting upstream of the bubble. This shock wave interaction gives birth to a high-pressure structure evident in Figure 6-19 (a) outside the bubble.

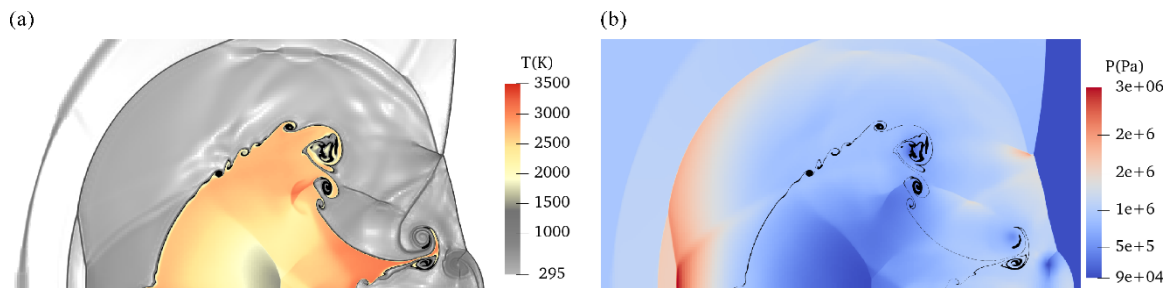


Figure 6-19. The flow field of Case 283-2 at 98 μ s. (a) temperature contour supposed on numerical schlieren image, only cells with $T > 1400$ K are plotted, (b) pressure contour.

Figure 6-18 (b) plots the history of normalized bubble volume, normalized flame volume, and heat release. The bubble volume decreases from the beginning as the windward interface is compressed by the incident shock wave. After ignition at 35 μ s, the detonation wave propagates, and V_{flame} quickly increases and catches up with

V_{bubble} at 46 μs (shown in Figure 6-13) when the bubble is fully ignited. Later the volume of flame and bubble is always the same. The bubble volume reaches a peak value at 97 μs , then decreases to a minimum value at 145 μs , and later keeps increasing to about 1.4 of the initial bubble volume at 400 μs . The heat release history shares the same trend with $m_{\text{H}_2\text{O}}$ in Figure 6-18 (c), and the maximum heat release is detected at the end of this simulation with $h_{r,\text{max}}=95$ J.

Figure 6-18 (c) plots the mass of all reactants. Take H_2O as an example, the mass of H_2O keeps unchanged until 35 μs when the ignition occurs, later H_2O forms due to combustion, and $m_{\text{H}_2\text{O}}$ increases to around 6.6×10^{-6} kg. An interesting descending of $m_{\text{H}_2\text{O}}$ is detected at around 110 μs , and the cause will be analyzed later. Another interesting feature lies in the intermediate reactants such as OH, the m_{OH} increases after ignition, peaks at 44 μs when around 90% of the initial H_2 is consumed, decays after 44 μs , and re-increases again at around 100 μs . At around 130 μs , another peak value of m_{OH} is detected, then m_{OH} decays to the end.

Figure 6-18 (d) presents the instant heat release rate and mass generation rate of some distinct species. The dm/dt values deviate from 0 after ignition at 35 μs and peak at around 42 μs . Details will be presents later. Figure 6-18 (e) presents the instant mass generation rate of two distinct species and heat release rate. Reasonably, peak values of these two properties are detected at the exact moment. The maximum heat release rate is $(dh_r/dt)_{\text{max}}=10.6$ MJ/s.

6.2.2 Ignition and early flame propagation

Figure 6-20 plots the instant mass and mass generation rate of some representative species from 33 to 55 μs . Subfigure (b) shows that the fuel consumption rate deviates from zero at 36 μs which is the exact ignition time. After ignition, H_2 and O_2 are consuming and H_2O and OH are producing. At 40.5 μs , the water generation rate abruptly increases due to the second ignition shown in Figure 6-13. At 44 μs , the fuel consumption rate reaches a peak value, and at this moment, the two detonation fronts meet with each other inside the bubble. The maximum fuel consumption rate is 0.1125 kg/s. After that, the value of $|dm_{\text{H}_2}/dt|$ firstly decreases until 45.5 μs , the reaches the second peak at 46.5 μs , and later decreases to around 0 at 49.5 μs . At this moment, more than 90% of the initial O_2 are consumed.

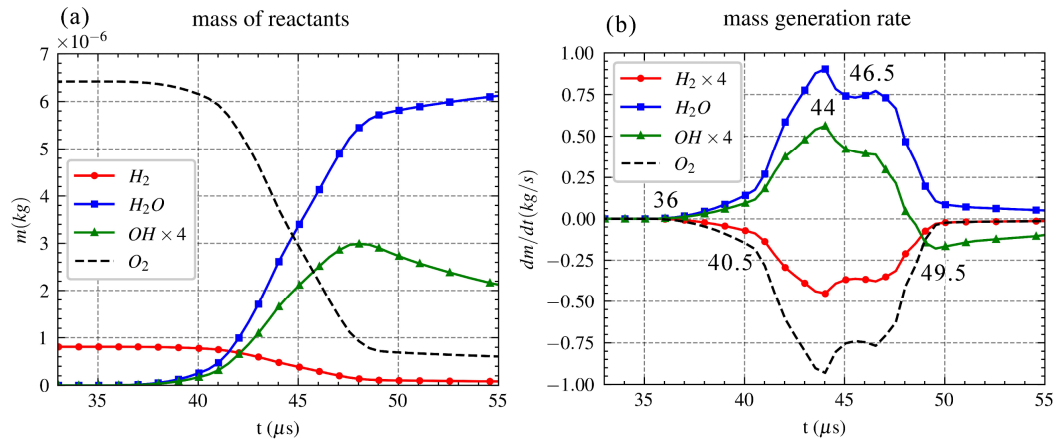


Figure 6-20. Instant reactive properties of the Case 283-2 from 30 to 55 μs . (a) mass of reactant, (b) mass generation rate.

6.2.3 Nonmonotonic behavior of heat release

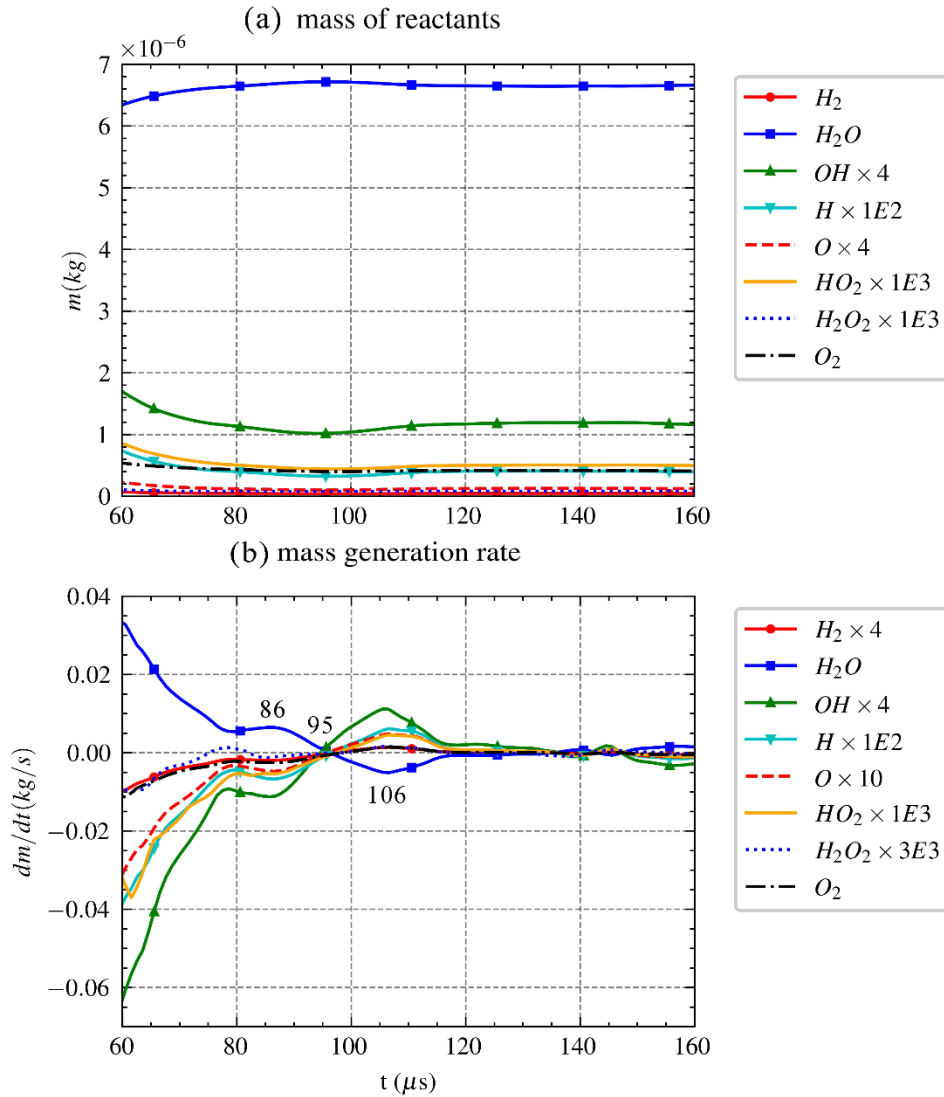


Figure 6-21. Instant reactive properties of Case 283-2 from 60 to 120 μ s: (a) mass of reactants, (b) mass generation rate.

To analyze the nonmonotonic behavior of heat release around 110 μ s, Figure 6-21 plots the mass and mass generation rate of reactant from 60 to 120 μ s in Case 283-2. As the heat release in hydrogen combustion is mostly caused by the chain termination step with H_2O generation, here I will analyze the profile of H_2O instead. In Figure 6-21 (b), dm_{H_2O}/dt is positive and equals 3.3×10^{-2} kg/s at 60 μ s. As around 90% of the fuel is burnt at this moment, the generation rate of H_2O decodes to 5.0×10^{-3} kg/s at 80 μ s. The later trend is not monotonic: dm_{H_2O}/dt increases at 86 μ s then decreases to nearly zero at 95 μ s, and later reaches a minimum value of -5.0×10^{-3} kg/s at 106 μ s. After 106 μ s, the values of dm/dt of all reactants approach zero, and similar nonmonotonic variation is observed again after 140 μ s.

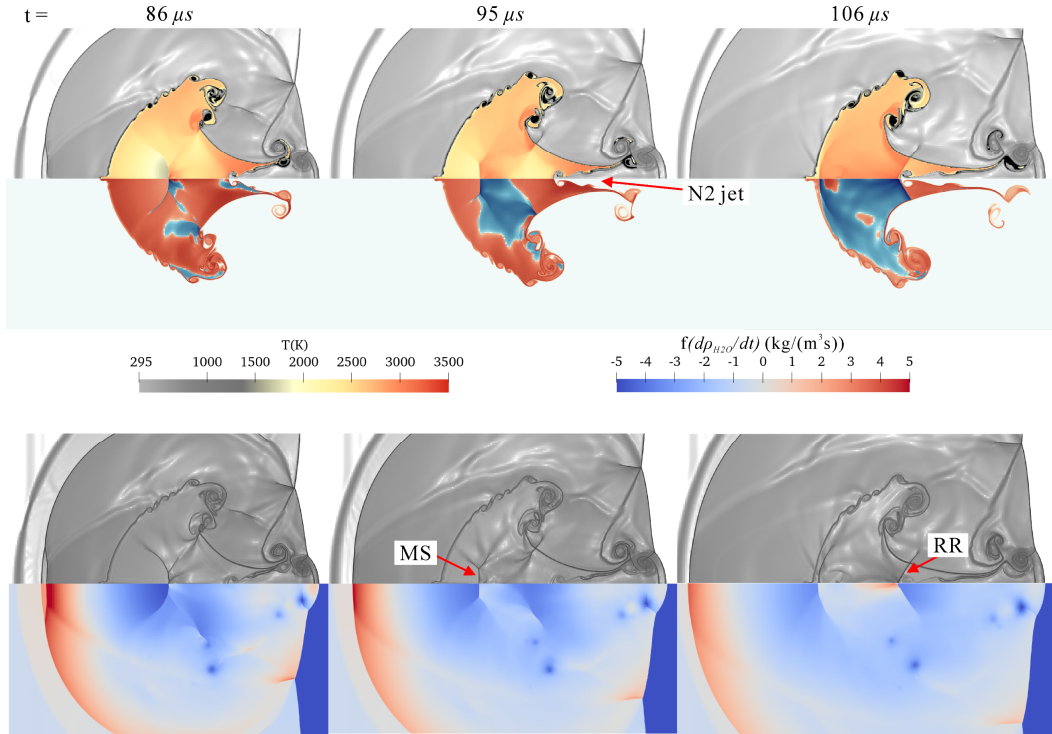


Figure 6-22. The flow field of the Case 283-2 reactive case at 86, 95, 106 μs . (a) Upper parts: temperature contour superposed on numerical schlieren image, only cells with $T > 1400\text{ K}$ are plotted, lower parts: contours of $f(dp_{\text{H}_2\text{O}}/dt)$. (b) Upper parts: the enhanced numerical schlieren images, lower parts: the pressure contour. MS: Mach stem, RR: regular reflection

Figure 6-22 presents the contours of temperature, distribution of H_2O generation, enhanced numerical schlieren, and pressure in Case 283-2 at 86, 95, and 106 μs . To clearly illustrate the distribution of H_2O generation, the value of $dp_{\text{H}_2\text{O}}/dt$ is rescaled to $[-5, 5]$ via Eq. (5.2):

$$f(dp_{\text{H}_2\text{O}}/dt) = \begin{cases} 0 & , \text{if } |dp_{\text{H}_2\text{O}}/dt| \leq 1 \\ \log_{10}(dp_{\text{H}_2\text{O}}/dt) & , \text{if } dp_{\text{H}_2\text{O}}/dt > 1 \\ -\log_{10}(-dp_{\text{H}_2\text{O}}/dt) & , \text{if } dp_{\text{H}_2\text{O}}/dt < -1 \end{cases} \quad (5.2)$$

Additionally, Figure 6-23 presents the combustion properties along the bubble axis for analysis.

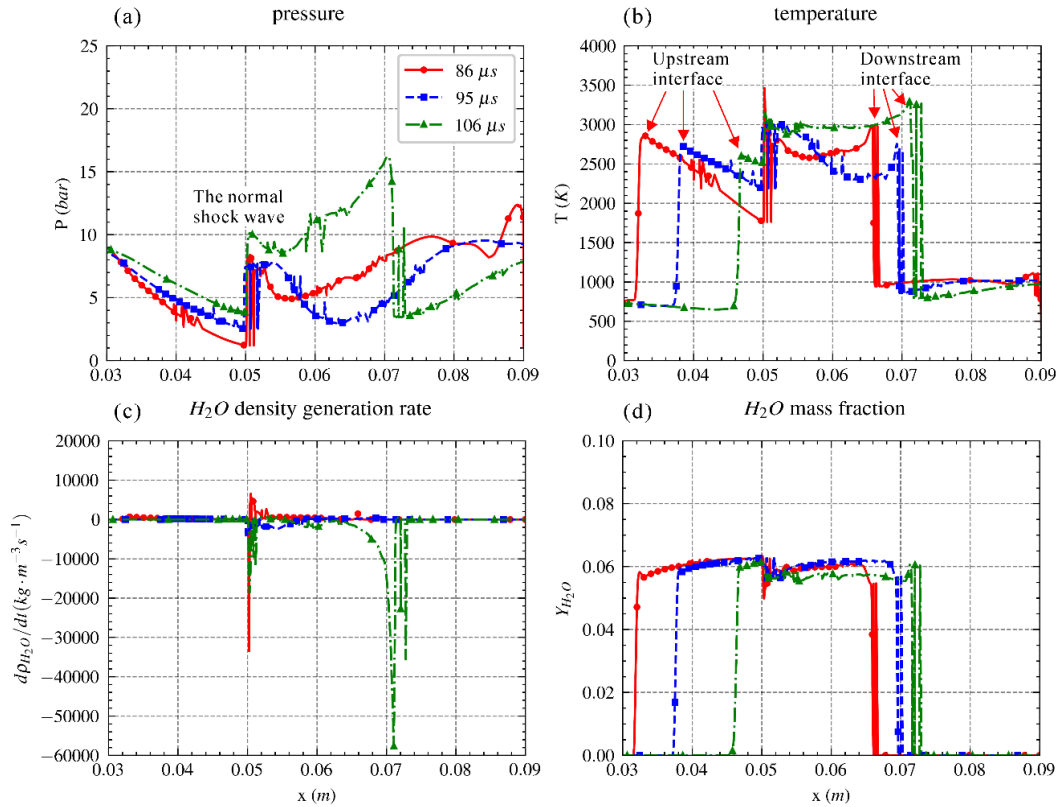


Figure 6-23. The flow properties along the bubble axis for Case 283-2 at 86, 95, and 106 μs . (a) pressure, (b) temperature, (c) ρ_{H_2O} generation rate, (d) Y_{H_2O} . The abscissa is the distance to the initial location of the upstream bubble pole.

Figure 6-22 shows that at 86 μs , a shock-shock interaction and Mach stem are found on the bubble axis and locates nearly at the center of the bubble. Take the coordinate in Figure 6-22 (a), the curvature of this Mach stem is first negative at 86 μs , later nearly zero at 95 μs since the Mach stem is nearly normal, and finally positive at 106 μs . This Mach stem is part of the complex shock system caused by the SBI and detonation waves. Interestingly, as can be observed from Figure 6-23 (a), from 86 to 106 μs , this normal shock wave barely moves and stays near $x = 0.05$ m. When the upstream interface moves to the right, the gap between it and the normal shock wave gradually decreases. The histories of unsteady contours of temperature, pressure, and $f(dp_{H_2O}/dt)$ show that, when the burnt gas crosses the normal shock, its temperature grows from around 2000 to 3000 K, and the water is consumed in the post-shock region. At 106 μs , a regular reflection (RR) is detected on the bubble axis near the N_2 jet. In the post-flow of this RR, the lowest water production rate is found, and $\left(\frac{d\rho_{H_2O}}{dt}\right)_{\min} = -5.8 \times 10^4 \text{ kg/m}^3 \cdot \text{s}$ in Figure 6-23.

This nonmonotonic chemical heat release behavior is definitely related to the re-equilibration of the burnt gas inside the bubble: according to Le Chatelier's principle, the water dissociation is endothermic. Thus, the high-

temperature and high-pressure post-shock region prefers dissociation of water and reduces chemical heat release. Later, the MS and RR shock systems are destructed, and the reactants re-equilibrate to the burnt state with recombination to H₂O which is exothermic.

6.3 Comparison of the lower- and high- Mach limiting cases

Two combustion modes are observed in these two RSBI numerical studies of lower- and high-Mach limit cases.

Table 6-2. Combustion in low and high Mach limit of RSBI simulations

	$M = 1.34$	$M = 2.83$
Combustion type	deflagration	detonation
Averaged fuel consumption rate (g/s)	0.144	11.88
Combustion effects on Γ in $10\tau_H$	Affects mildly and $ \Gamma^+ \uparrow$	Affects mildly and $ \Gamma^- \uparrow$
Combustion effects on χ in $10\tau_H$	36% \uparrow	270% \uparrow

It is of great interest to compare the combustion behaviors in the low and high Mach limit cases of RSBI. Table 6-2 lists the combustion details in these two cases. In the $M = 1.34$ case, the flame is deflagration, while in the $M = 2.83$ case, the flame is detonation. The averaged fuel consumption rates are evaluated after ignition. Comparisons show that the averaged fuel consumption rate for the $M = 2.83$ case is more significant by a factor of roughly 100. In both cases, combustion influences the vorticity mildly. However, the deflagration waves increase $|\Gamma^+|$, while the detonation waves decrease $|\Gamma^-|$. Furthermore, combustion promotes the mixing of SBI in both cases, and the increment caused by the detonation waves is around 7 folds of the one due to the deflagration waves. Analyses in Sections 6.1.2 and 6.2.1 show that the significant strengthening of mixing in the high Mach number case is mostly related to the diffusivity mechanism due to the high temperature and pressure of detonation waves.

7. Conclusions

In this thesis, the RSBI phenomena are numerically investigated using a novel combustion AMR solver Fire developed during my PhD study. The novel RSBI experiments by Haehn et al. [88] are faithfully reproduced by numerical methods for the first time. Two combustion modes, which depend on the incident shock strength, are confirmed by this research. The shock wave systems, ignition and complex SFI, effects of combustion on the waves systems, vorticity, and mixing rate of SBI get analysed in detail.

The Fire solver deals with the compressible combustion problems using the AMR method. Extra AMR strategies based on an empirical threshold of ignition/flame temperature are proposed and effectively refine the hydrodynamic or chemical discontinuities separately. Extensive validations on one-/two-dimensional inert/reactive problems prove that the Fire solver is a reliable and high-efficiency tool for detonation simulations. Later, this solver is used to numerically reproduce the RSBI in Haehn et al.'s experiment [88] using a pressure-dependent comprehensive H₂/O₂ mechanism [60].

For the low-Mach-number ($M = 1.34$) case, the grid-convergence test shows that the convergent result is deflagration, and coarse grids lead to unphysical detonation. RMI dominates the SBI development. For this heavy bubble case, shock focusing occurs at the rear of the bubble and induces ignition. The deflagration waves barely influence the TBD or primary vortex but suppress the secondary interfacial KHI structures and upstream jet. The experimental bubble morphology and chemiluminescence images are successfully reproduced, including the bubble length scale, primary and secondary vortices, flame shape, and speed of the flame fronts. The fuel consumption rate is nonmonotonic and is explained by unsteady flame propagation. Deviations possibly arise from the experimental insufficiency in detecting early ignition and may also be related to the neglect of the soap films in our modeling. The total vorticity is not greatly affected by the combustion until 470 μ s because of the negative vorticities deposited on the flame fronts. In contrast, combustion strongly promotes the mixing of SBI. In this simulation, the thermal effects of combustion increase the overall mixing by approximately 36% in $10\tau_{IH}$, in which 71% of the growth is due to the thermal effects on diffusivity and 29% is related to the species gradient and interfacial area. In addition to the traditional shock-focusing explanation, we consider the influence of secondary refracted shock. Mach reflection occurs during shock focusing and becomes bifurcated because of the strong backward jet. Later, this Mach reflection transits from the bifurcated type to the single type, and this transition is related to wave refraction at the leeward interface. The Mach reflection transition causes two ignitions. The first occurs in the spiral hot spot entrained by the jet vortex, and the flame is deflagrations. The second arises

from the hot spot caused by the triple point collision, and the newborn flame is deflagration in the beginning but tends to transit to detonation after interaction with the Mach reflection wave structures. The shock-flame interactions accelerate the flame fronts once to approximately 1050 m/s. Finally, the flame fronts are decoupled from the preceding shocks, and the stable combustion mode is deflagration. The reflected wave and weak pressure waves deposit vorticities and lead to transverse instabilities on the flame fronts because of the RMI effects.

For the high-Mach-number ($M = 2.83$) case, due to the high incident shock strength, two ignitions occur at the early stage of the SBI, namely the axial and shock-focusing ignitions, and both cause detonation waves. These two detonation waves induce complex wave systems which are significantly different from their inert counterparts. One signature effect of the detonation is the significant increments of TBD value comparing with the inert case. Similar to the low-Mach-number case, the detonation affects the vorticity mildly, but the deflagration increases the magnitude of the negative vorticity, while the influence of detonation is opposite. Also, the detonation increases the mixing rate, and the increment is around 7 folds of one for the deflagration case.

The uncertainties in experimental data by Haehn et al. [88] indicate the initial perturbations on the bubble interface may significantly influence the RSBI developments. Besides, the soap film shall be considered for better agreements. These effects will be considered in the future.

References

1. Geoffrey T (1950) The instability of liquid surfaces when accelerated in a direction perpendicular to their planes. I. Proc R Soc Lond A 201:192–196. doi: 10.1098/rspa.1950.0052
2. Markstein GH (1957) A shock-tube study of flame front-pressure wave interaction. Symposium (International) on Combustion 6:387–398. doi: 10.1016/S0082-0784(57)80054-X
3. Rudinger G (1958) Shock wave and flame interactions. In: Combustion and Propulsion, Third AGARD Colloquium. Pergamon Press London, p 153
4. Rudinger G, Somers LM (1960) Behaviour of small regions of different gases carried in accelerated gas flows. J Fluid Mech 7:161–176. doi: 10.1017/S0022112060001419
5. Richtmyer RD (1960) Taylor instability in shock acceleration of compressible fluids. Communications on Pure and Applied Mathematics 13:297–319. doi: 10.1002/cpa.3160130207
6. Edney B (1968) Anomalous Heat Transfer and Pressure Distributions on Blunt Bodies at Hypersonic Speeds in the Presence of an Impinging Shock. Flygtekniska Forsöksanstalten, Stockholm (Sweden)
7. Meshkov E (1969) Instability of the interface of two gases accelerated by a shock wave. Fluid Dynamics 4:101–104
8. Meyer KA (1972) Numerical Investigation of the Stability of a Shock-Accelerated Interface between Two Fluids. Phys Fluids 15:753. doi: 10.1063/1.1693980
9. Neufeld PD, Janzen A, Aziz R (1972) Empirical equations to calculate 16 of the transport collision integrals $\Omega_{\alpha\beta}(l, s)^*$ for the Lennard-Jones (12–6) potential. The Journal of Chemical Physics 57:1100–1102
10. Van Leer B (1974) Towards the ultimate conservative difference scheme. II. Monotonicity and conservation combined in a second-order scheme. Journal of computational physics 14:361–370
11. Slack M (1977) Rate coefficient for $H^+ O_2 + M = HO_2 + M$ evaluated from shock tube measurements of induction times. Combustion and Flame 28:241–249
12. Van Leer B (1979) Towards the ultimate conservative difference scheme. V. A second-order sequel to Godunov's method. Journal of computational Physics 32:101–136
13. Zeldovich Y (1980) Regime classification of an exothermic reaction with nonuniform initial conditions. Combustion and Flame 39:211–214. doi: 10.1016/0010-2180(80)90017-6
14. Picone J, Oran E, Boris J, Young Jr T (1984) Theory of vorticity generation by shock wave and flame interactions. NAVAL RESEARCH LAB WASHINGTON DC
15. Berger MJ, Olinger J (1984) Adaptive mesh refinement for hyperbolic partial differential equations. Journal of computational Physics 53:484–512
16. Fraley G (1986) Rayleigh–Taylor stability for a normal shock wave–density discontinuity interaction. Phys Fluids 29:376. doi: 10.1063/1.865722
17. Haas J-F, Sturtevant B (1987) Interaction of weak shock waves with cylindrical and spherical gas inhomogeneities. J Fluid Mech 181:41. doi: 10.1017/S0022112087002003
18. Picone J, Boris J (1988) Vorticity generation by shock propagation through bubbles in a gas. Journal of Fluid Mechanics 189:23–51

19. Jachimowski CJ (1988) An analytical study of the hydrogen-air reaction mechanism with application to scramjet combustion
20. Chapman S, Cowling TG, Burnett D (1990) The mathematical theory of non-uniform gases: an account of the kinetic theory of viscosity, thermal conduction and diffusion in gases. Cambridge university press
21. Berger M, Rigoutsos I (1991) An algorithm for point clustering and grid generation. *IEEE Transactions on Systems, Man, and Cybernetics* 21:1278–1286
22. Jacobs JW (1992) Shock-induced mixing of a light-gas cylinder. *J Fluid Mech* 234:629. doi: 10.1017/S0022112092000946
23. Scarinci T, Lee J, Thomas G, Bambrey R, Edwards D (1993) Amplification of a pressure wave by its passage through a flame front. *Progress in Astronautics and Aeronautics* 152:3–3
24. Grove JW, Holmes R, Sharp DH, Yang Y, Zhang Q (1993) Quantitative theory of Richtmyer-Meshkov instability. *Phys Rev Lett* 71:3473–3476. doi: 10.1103/PhysRevLett.71.3473
25. Klein RI, McKee CF, Colella P (1994) On the hydrodynamic interaction of shock waves with interstellar clouds. 1: Nonradiative shocks in small clouds. *The Astrophysical Journal* 420:213–236
26. Mikaelian KO (1994) Freeze-out and the effect of compressibility in the Richtmyer–Meshkov instability. *Physics of Fluids* 6:356–368. doi: 10.1063/1.868091
27. Samtaney R, Zabusky NJ (1994) Circulation deposition on shock-accelerated planar and curved density-stratified interfaces: models and scaling laws. *J Fluid Mech* 269:45–78. doi: 10.1017/S0022112094001485
28. Petersen E, Davidson D, Röhrig M, Hanson R (1996) High-pressure shock-tube measurements of ignition times in stoichiometric H₂/O₂/Ar mixtures. In: *Proceedings of the 20th international symposium on shock waves*. pp 941–946
29. Zhang Q, Sohn S-I (1997) Nonlinear theory of unstable fluid mixing driven by shock wave. *Physics of Fluids* 9:1106–1124. doi: 10.1063/1.869202
30. Zabusky N, Zeng S (1998) Shock cavity implosion morphologies and vortical projectile generation in axisymmetric shock–spherical fast/slow bubble interactions. *Journal of Fluid Mechanics* 362:327–346
31. Ju Y, Shimano A, Inoue O (1998) Vorticity generation and flame distortion induced by shock flame interaction. *Symposium (International) on Combustion* 27:735–741. doi: 10.1016/S0082-0784(98)80467-0
32. Oran ES, Weber JW, Stefaniw EI, Lefebvre MH, Anderson JD (1998) A Numerical Study of a Two-Dimensional H₂-O₂-Ar Detonation Using a Detailed Chemical Reaction Model. *Combustion and Flame* 113:147–163. doi: 10.1016/S0010-2180(97)00218-6
33. Khokhlov AM (1998) Fully Threaded Tree Algorithms for Adaptive Refinement Fluid Dynamics Simulations. *Journal of Computational Physics* 143:519–543. doi: 10.1006/jcph.1998.9998
34. Vandenboomgaerde M, Mügler C, Gauthier S (1998) Impulsive model for the Richtmyer-Meshkov instability. *Phys Rev E* 58:1874–1882. doi: 10.1103/PhysRevE.58.1874
35. Courant R, Friedrichs KO (1999) *Supersonic flow and shock waves*. Springer Science & Business Media
36. Zhang Q, Sohn S-I (1999) Quantitative theory of Richtmyer-Meshkov instability in three dimensions. *Zeitschrift für angewandte Mathematik und Physik* 50:1. doi: 10.1007/s000330050137
37. Khokhlov AM, Oran ES, Chtchelkanova AY, Wheeler JC (1999) Interaction of a shock with a sinusoidally perturbed flame. *Combustion and flame* 117:99–116

38. Whitham GB (1999) *Linear and nonlinear waves*. Wiley, New York Chichester Weinheim
39. Zabusky NJ (1999) VORTEX PARADIGM FOR ACCELERATED INHOMOGENEOUS FLOWS: Visiometrics for the Rayleigh-Taylor and Richtmyer-Meshkov Environments. *Annu Rev Fluid Mech* 31:495–536. doi: 10.1146/annurev.fluid.31.1.495
40. Holmes RL, Dimonte G, Fryxell B, Gittings ML, Grove JW, Schneider M, Sharp DH, Velikovich AL, Weaver RP, Zhang Q (1999) Richtmyer–Meshkov instability growth: experiment, simulation and theory. *Journal of Fluid Mechanics* 389:55–79. doi: 10.1017/S0022112099004838
41. Fryxell B, Olson K, Ricker P, Timmes F, Zingale M, Lamb D, MacNeice P, Rosner R, Truran J, Tufo H (2000) FLASH: An adaptive mesh hydrodynamics code for modeling astrophysical thermonuclear flashes. *The Astrophysical Journal Supplement Series* 131:273
42. MacNeice P, Olson KM, Mobarrry C, de Fainchtein R, Packer C (2000) PARAMESH: A parallel adaptive mesh refinement community toolkit. *Computer Physics Communications* 126:330–354. doi: 10.1016/S0010-4655(99)00501-9
43. Hornung HG (2000) Oblique shock reflection from an axis of symmetry. *J Fluid Mech* 409:1–12. doi: 10.1017/S0022112099007831
44. Sharpe F, Sharpe SAEG (2000) Two-dimensional numerical simulations of idealized detonations. *Proc R Soc Lond A* 456:2081–2100. doi: 10.1098/rspa.2000.0603
45. Wissink AM, Hornung RD, Kohn SR, Smith SS, Elliott N (2001) Large scale parallel structured AMR calculations using the SAMRAI framework. In: *Proceedings of the 2001 ACM/IEEE conference on Supercomputing*. pp 6–6
46. Hughes K, Turányi T, Clague A, Pilling M (2001) Development and testing of a comprehensive chemical mechanism for the oxidation of methane. *International journal of chemical kinetics* 33:513–538
47. Singh S, Rastigejev Y, Paolucci S, Powers JM (2001) Viscous detonation in H_2-O_2-Ar using intrinsic low-dimensional manifolds and wavelet adaptive multilevel representation. *Combustion Theory and Modelling* 5:163–184. doi: 10.1088/1364-7830/5/2/303
48. Gamezo VN, Khokhlov AM, Oran ES (2001) The influence of shock bifurcations on shock-flame interactions and DDT. *Combustion and Flame* 126:1810–1826. doi: 10.1016/S0010-2180(01)00291-7
49. Sharpe GJ (2001) Transverse waves in numerical simulations of cellular detonations. *J Fluid Mech* 447:31–51. doi: 10.1017/S0022112001005535
50. Thomas G, Bambrey R, Brown C (2001) Experimental observations of flame acceleration and transition to detonation following shock-flame interaction. *Combustion Theory and Modelling* 5:573–594. doi: 10.1088/1364-7830/5/4/304
51. McBride BJ, Zehe MJ, Gordon S (2002) NASA Glenn Coefficients for Calculating Thermodynamic Properties of Individual Species. 297
52. Brouillette M (2002) the Richtmyer-Meshkov Instability. *Annual Review of Fluid Mechanics* 34:445–468. doi: 10.1146/annurev.fluid.34.090101.162238
53. Skews BW, Menon N, Bredin M, Timofeev EV (2002) An experiment on imploding conical shock waves. *Shock Waves* 11:323–326. doi: 10.1007/s001930100115
54. Kee RJ, Coltrin ME, Glarborg P (2003) *Chemically reacting flow: theory and practice*. Wiley-Interscience, Hoboken, N.J

55. Mikaelian KO (2003) Explicit expressions for the evolution of single-mode Rayleigh-Taylor and Richtmyer-Meshkov instabilities at arbitrary Atwood numbers. *Physical Review E* 67. doi: 10.1103/PhysRevE.67.026319
56. Henderson LF, Vasilev EI, Ben-Dor G, Elperin T (2003) The wall-jetting effect in Mach reflection: theoretical consideration and numerical investigation. *J Fluid Mech* 479:259–286. doi: 10.1017/S0022112002003518
57. Peng G, Zabusky NJ, Zhang S (2003) Vortex-accelerated secondary baroclinic vorticity deposition and late-intermediate time dynamics of a two-dimensional Richtmyer–Meshkov interface. *Physics of Fluids* 15:3730–3744. doi: 10.1063/1.1621628
58. Billet G, Abgrall R (2003) An adaptive shock-capturing algorithm for solving unsteady reactive flows. *Computers & Fluids* 32:1473–1495. doi: 10.1016/S0045-7930(03)00004-5
59. Billet G, Abgrall R (2003) An adaptive shock-capturing algorithm for solving unsteady reactive flows. *Computers & Fluids* 32:1473–1495. doi: 10.1016/S0045-7930(03)00004-5
60. Ó Conaire M, Curran HJ, Simmie JM, Pitz WJ, Westbrook CK (2004) A comprehensive modeling study of hydrogen oxidation: A Comprehensive Modeling Study of Hydrogen Oxidation. *International Journal of Chemical Kinetics* 36:603–622. doi: 10.1002/kin.20036
61. Poinso T, Denis V (2005) *Theoretical and Numerical Combustion*
62. Jacobs JW, Krivets VV (2005) Experiments on the late-time development of single-mode Richtmyer–Meshkov instability. *Physics of Fluids* 17:034105. doi: 10.1063/1.1852574
63. Ranjan D, Anderson M, Oakley J, Bonazza R (2005) Experimental Investigation of a Strongly Shocked Gas Bubble. *Phys Rev Lett* 94:184507. doi: 10.1103/PhysRevLett.94.184507
64. Jourdan G, Houas L (2005) High-Amplitude Single-Mode Perturbation Evolution at the Richtmyer–Meshkov Instability. *Phys Rev Lett* 95:204502. doi: 10.1103/PhysRevLett.95.204502
65. Oran ES, Gamezo VN (2007) Origins of the deflagration-to-detonation transition in gas-phase combustion. *Combustion and Flame* 148:4–47. doi: 10.1016/j.combustflame.2006.07.010
66. Gamezo VN, Ogawa T, Oran ES (2007) Numerical simulations of flame propagation and DDT in obstructed channels filled with hydrogen–air mixture. *Proceedings of the Combustion Institute* 31:2463–2471. doi: 10.1016/j.proci.2006.07.220
67. Dryer FL, Chaos M, Zhao Z, Stein JN, Alpert JY, Homer CJ (2007) Spontaneous ignition of pressurized releases of hydrogen and natural gas into air. *Combustion Science and Technology* 179:663–694. doi: 10.1080/00102200600713583
68. Niederhaus JHJ, Greenough JA, Oakley JG, Ranjan D, Anderson MH, Bonazza R (2008) A computational parameter study for the three-dimensional shock–bubble interaction. *Journal of Fluid Mechanics* 594:85–124. doi: 10.1017/S0022112007008749
69. Ranjan D, Niederhaus JHJ, Oakley JG, Anderson MH, Bonazza R, Greenough JA (2008) Shock-bubble interactions: Features of divergent shock-refraction geometry observed in experiments and simulations. *Physics of Fluids* 20:036101. doi: 10.1063/1.2840198
70. Billet G, Giovangigli V, de Gassowski G (2008) Impact of volume viscosity on a shock–hydrogen-bubble interaction. *Combustion Theory and Modelling* 12:221–248. doi: 10.1080/13647830701545875
71. Dong G, Fan B, Ye J (2008) Numerical investigation of ethylene flame bubble instability induced by shock waves. *Shock Waves* 17:409–419. doi: 10.1007/s00193-008-0124-3

72. Tomkins C, Kumar S, Orlicz G, Prestridge K (2008) An experimental investigation of mixing mechanisms in shock-accelerated flow. *Journal of Fluid Mechanics* 611:131–150. doi: 10.1017/S0022112008002723
73. Ranjan D, Niederhaus JHJ, Oakley JG, Anderson MH, Greenough JA, Bonazza R (2008) Experimental and numerical investigation of shock-induced distortion of a spherical gas inhomogeneity. *Physica Scripta* T132:014020. doi: 10.1088/0031-8949/2008/T132/014020
74. Toro EF (2009) *Riemann solvers and numerical methods for fluid dynamics: a practical introduction*, 3rd ed. Springer, Dordrecht ; New York
75. Takahashi F (2009) Extinguishment of diffusion flames around a cylinder in a coaxial air stream with dilution or water mist. *Proceedings of the Combustion Institute* 9
76. Gui M, Fan B, Dong G, Ye J (2009) Interaction of a reflected shock from a concave wall with a flame distorted by an incident shock. *Shock Waves* 18:487–494. doi: 10.1007/s00193-008-0177-3
77. Ji H, Lien F-S, Yee E (2010) A new adaptive mesh refinement data structure with an application to detonation. *Journal of Computational Physics* 229:8981–8993. doi: 10.1016/j.jcp.2010.08.023
78. Mahmoudi Y, Mazaheri K (2011) High resolution numerical simulation of the structure of 2-D gaseous detonations. *Proceedings of the Combustion Institute* 33:2187–2194. doi: 10.1016/j.proci.2010.07.083
79. Gowardhan AA, Grinstein FF (2011) Numerical simulation of Richtmyer–Meshkov instabilities in shocked gas curtains. *Journal of Turbulence* 12:N43. doi: 10.1080/14685248.2011.622770
80. Ranjan D, Oakley J, Bonazza R (2011) Shock-Bubble Interactions. *Annual Review of Fluid Mechanics* 43:117–140. doi: 10.1146/annurev-fluid-122109-160744
81. Shankar SK, Kawai S, Lele SK (2011) Two-dimensional viscous flow simulation of a shock accelerated heavy gas cylinder. *Physics of Fluids* 23:024102. doi: 10.1063/1.3553282
82. Liberman MA, Kiverin AD, Ivanov MF (2011) On detonation initiation by a temperature gradient for a detailed chemical reaction models. *Physics Letters A* 375:1803–1808. doi: 10.1016/j.physleta.2011.03.026
83. Kilchyk V, Nalim R, Merkle C (2011) Laminar premixed flame fuel consumption rate modulation by shocks and expansion waves. *Combustion and Flame* 158:1140–1148. doi: 10.1016/j.combustflame.2010.10.026
84. Zhai Z, Si T, Luo X, Yang J (2011) On the evolution of spherical gas interfaces accelerated by a planar shock wave. *Physics of Fluids* 23:084104. doi: 10.1063/1.3623272
85. Haehn N, Weber C, Oakley J, Anderson M, Rothamer D, Ranjan D, Bonazza R (2012) Experimental Shock-Initiated Combustion of a Spherical Density Inhomogeneity. In: Kontis K (ed) *28th International Symposium on Shock Waves*. Springer Berlin Heidelberg, Berlin, Heidelberg, pp 359–364
86. Haehn NS (2012) *Experimental Investigation of the Reactive Shock-bubble Interaction*. PhD Thesis, The University of Wisconsin-Madison
87. Fan M, Zhai Z, Si T, Luo X, Zou L, Tan D (2012) Numerical study on the evolution of the shock-accelerated SF₆ interface: Influence of the interface shape. *Science China Physics, Mechanics and Astronomy* 55:284–296. doi: 10.1007/s11433-011-4604-6
88. Haehn N, Ranjan D, Weber C, Oakley J, Rothamer D, Bonazza R (2012) Reacting shock bubble interaction. *Combustion and Flame* 159:1339–1350. doi: 10.1016/j.combustflame.2011.10.015
89. Si T, Zhai Z, Yang J, Luo X (2012) Experimental investigation of reshocked spherical gas interfaces. *Phys Fluids* 24:054101. doi: 10.1063/1.4711866

90. Massa L, Jha P (2012) Linear analysis of the Richtmyer-Meshkov instability in shock-flame interactions. *Phys Fluids* 24:056101. doi: 10.1063/1.4719153
91. Mazaheri K, Mahmoudi Y, Radulescu MI (2012) Diffusion and hydrodynamic instabilities in gaseous detonations. *Combustion and Flame* 159:2138–2154. doi: 10.1016/j.combustflame.2012.01.024
92. Mahmoudi Y, Mazaheri K (2012) Triple Point Collision and Hot Spots in Detonations with Regular Structure. *Combustion Science and Technology* 184:1135–1151. doi: 10.1080/00102202.2012.664004
93. Wang M, Si T, Luo X (2013) Generation of polygonal gas interfaces by soap film for Richtmyer–Meshkov instability study. *Experiments in Fluids* 54. doi: 10.1007/s00348-012-1427-9
94. Mével R, Pichon S, Catoire L, Chaumeix N, Paillard C-E, Shepherd JE (2013) Dynamics of excited hydroxyl radicals in hydrogen-based mixtures behind reflected shock waves. *Proceedings of the Combustion Institute* 34:677–684. doi: 10.1016/j.proci.2012.06.151
95. Bhattacharjee RR, Lau-Chapdelaine SSM, Maines G, Maley L, Radulescu MI (2013) Detonation re-initiation mechanism following the Mach reflection of a quenched detonation. *Proceedings of the Combustion Institute* 34:1893–1901. doi: 10.1016/j.proci.2012.07.063
96. Zhai Z-G, Si T, Zou L-Y, Luo X-S (2013) Jet formation in shock-heavy gas bubble interaction. *Acta Mechanica Sinica* 29:24–35. doi: 10.1007/s10409-013-0003-8
97. Hu XY, Adams NA, Shu C-W (2013) Positivity-preserving method for high-order conservative schemes solving compressible Euler equations. *Journal of Computational Physics* 242:169–180. doi: 10.1016/j.jcp.2013.01.024
98. Yang Q, Chang J, Bao W (2014) Richtmyer-Meshkov Instability Induced Mixing Enhancement in the Scramjet Combustor with a Central Strut. *Advances in Mechanical Engineering* 6:614189. doi: 10.1155/2014/614189
99. Jasper AW, Miller JA (2014) Lennard–Jones parameters for combustion and chemical kinetics modeling from full-dimensional intermolecular potentials. *Combustion and Flame* 161:101–110. doi: 10.1016/j.combustflame.2013.08.004
100. Tritschler VK, Avdonin A, Hickel S, Hu XY, Adams NA (2014) Quantification of initial-data uncertainty on a shock-accelerated gas cylinder. *Physics of Fluids* 26:026101. doi: 10.1063/1.4865756
101. Hu XY, Tritschler VK, Pirozzoli S, Adams NA (2014) Dispersion-dissipation condition for finite difference schemes. arXiv:12045088 [physics]
102. Paolucci S, Zikoski ZJ, Wirasaet D (2014) WAMR: An adaptive wavelet method for the simulation of compressible reacting flow. Part I. Accuracy and efficiency of algorithm. *Journal of Computational Physics* 272:814–841. doi: 10.1016/j.jcp.2014.01.025
103. Jasper AW, Kamarchik E, Miller JA, Klippenstein SJ (2014) First-principles binary diffusion coefficients for H, H₂, and four normal alkanes + N₂. *The Journal of Chemical Physics* 141:124313. doi: 10.1063/1.4896368
104. Attal N, Ramaprabhu P (2015) Numerical investigation of a single-mode chemically reacting Richtmyer-Meshkov instability. *Shock Waves* 25:307–328. doi: 10.1007/s00193-015-0571-6
105. Wang C, Dong X, Shu C-W (2015) Parallel adaptive mesh refinement method based on WENO finite difference scheme for the simulation of multi-dimensional detonation. *Journal of Computational Physics* 298:161–175. doi: 10.1016/j.jcp.2015.06.001
106. Diego U of C at S (2016) Chemical-Kinetic Mechanisms for Combustion Applications. *Mechanical and Aerospace Engineering (Combustion Research)*

107. Diegelmann F, Tritschler V, Hickel S, Adams N (2016) On the pressure dependence of ignition and mixing in two-dimensional reactive shock-bubble interaction. *Combustion and Flame* 163:414–426. doi: 10.1016/j.combustflame.2015.10.016
108. Diegelmann F, Hickel S, Adams NA (2016) Shock Mach number influence on reaction wave types and mixing in reactive shock-bubble interaction. *Combustion and Flame* 174:85–99. doi: 10.1016/j.combustflame.2016.09.014
109. Gs S, Candler GV (2017) Large eddy simulations of reacting shock-bubble interaction. In: Sonderforschungsbereich/Transregio 40-Summer Program Report 2015. p 14
110. Shen H, Parsani M (2017) The role of multidimensional instabilities in direct initiation of gaseous detonations in free space. *Journal of Fluid Mechanics* 813. doi: 10.1017/jfm.2017.5
111. Chen X, Dong G, Jiang H (2017) A three-dimensional numerical study on instability of sinusoidal flame induced by multiple shock waves. *Acta Mech Sin* 33:316–326. doi: 10.1007/s10409-017-0639-x
112. Diegelmann F, Hickel S, Adams NA (2017) Three-dimensional reacting shock-bubble interaction. *Combustion and Flame* 181:300–314. doi: 10.1016/j.combustflame.2017.03.026
113. Syrakos A, Varchanis S, Dimakopoulos Y, Goulas A, Tsamopoulos J (2017) A critical analysis of some popular methods for the discretisation of the gradient operator in finite volume methods. *Physics of Fluids* 29:127103. doi: 10.1063/1.4997682
114. Ding J, Liang Y, Chen M, Zhai Z, Si T, Luo X (2018) Interaction of planar shock wave with three-dimensional heavy cylindrical bubble. *Physics of Fluids* 30:106109
115. Schive H-Y, ZuHone JA, Goldbaum NJ, Turk MJ, Gaspari M, Cheng C-Y (2018) GAMER-2: a GPU-accelerated adaptive mesh refinement code—accuracy, performance, and scalability. *Monthly Notices of the Royal Astronomical Society* 481:4815–4840
116. Goodwin DG, Speth RL, Moffat HK, Weber BW (2018) Cantera: An Object-oriented Software Toolkit for Chemical Kinetics, Thermodynamics, and Transport Processes
117. Zhai Z, Zou L, Wu Q, Luo X (2018) Review of experimental Richtmyer–Meshkov instability in shock tube: From simple to complex. *Proceedings of the Institution of Mechanical Engineers, Part C: Journal of Mechanical Engineering Science* 232:2830–2849. doi: 10.1177/0954406217727305
118. Liu L, Liang Y, Ding J, Liu N, Luo X (2018) An elaborate experiment on the single-mode Richtmyer–Meshkov instability. *J Fluid Mech* 853:R2. doi: 10.1017/jfm.2018.628
119. Lawson J, Shepherd J (2019) Shock and detonation toolbox installation instructions. California Institute of Technology, Pasadena, CA
120. Schmidmayer K, Petitpas F, Daniel E (2019) Adaptive Mesh Refinement algorithm based on dual trees for cells and faces for multiphase compressible flows. *Journal of Computational Physics* 388:252–278. doi: 10.1016/j.jcp.2019.03.011
121. Zhou Y, Clark TT, Clark DS, Gail Glendinning S, Aaron Skinner M, Huntington CM, Hurricane OA, Dimits AM, Remington BA (2019) Turbulent mixing and transition criteria of flows induced by hydrodynamic instabilities. *Physics of Plasmas* 26:080901. doi: 10.1063/1.5088745
122. Guan B, Wang D, Wang G, Fan E, Wen C-Y (2020) Numerical study of the Richtmyer–Meshkov instability of a three-dimensional minimum-surface featured SF6/air interface. *Physics of Fluids* 32:024108
123. Tyaktev AA, Pavlenko AV, Anikin NB, Bugaenko IL, Piskunov YuA (2020) Richtmyer–Meshkov Instability of Laminar Flame. *J Appl Mech Tech Phy* 61:157–161. doi: 10.1134/S0021894420020017

124. Bambauer M, Hasslberger J, Klein M (2020) Direct Numerical Simulation of the Richtmyer–Meshkov Instability in Reactive and Nonreactive Flows. *Combustion Science and Technology* 1–18. doi: 10.1080/00102202.2020.1763325
125. Schmidmayer K, Petitpas F, Le Martelot S, Daniel É (2020) ECOGEN: An open-source tool for multiphase, compressible, multiphysics flows. *Computer Physics Communications* 251:107093. doi: 10.1016/j.cpc.2019.107093
126. Sarkar S, Mukhopadhyay A, Sen S (2021) The effects of steam and water spray on NO formation in a methane–air counterflow diffusion flame. *Combustion Theory and Modelling* 1–28. doi: 10.1080/13647830.2021.1905880
127. Deiterding R AMROC - Block Structured Adaptive Mesh Refinement in Object-oriented C++
128. Karypis G ParMETIS - Parallel Graph Partitioning and Fill-reducing Matrix Ordering
129. PETSc Team PETSc/Tao: Portable, Extensible Toolkit for Scientific Computation Toolkit for Advanced Optimization
130. Kevin S, Fabien P, Sébastien LM, Éric D ECOGEN-v2.0
131. Schultz E, Shepherd J Detonation analysis using detailed reaction mechanisms. 6

Appendices

A.1 Molecular properties of some species in this thesis

Table A-0-1. Molecular properties of some species in this thesis

Species	$(\varepsilon/k)_i$	σ_i	$MW_i(\text{g/mol})$
H	541.572	1.530	1.00794
H ₂	304.690	2.190	2.01588
H ₂ O	637.056	2.943	18.01528
H ₂ O ₂	1361.148	3.179	34.0147
HO ₂	963.003	3.129	33.00677
N ₂	97.839	3.610	28.0134
O	235.686	2.485	15.9994
O ₂	676.424	3.069	31.9988
OH	514.598	2.582	17.00734
Xe	282.290	3.8924	131.293

All molecular properties in Table A-0-1 can be found in Jasper et al. [103], Jasper and Miller [99], and Chapman et al. [20].

A.2 The H₂ combustion mechanism of Ó Conaire[60]

Table I Revised H₂/O₂ Reaction Mechanism (units: cm³, mol, s, kcal, K)

	Reaction	A	n	E _a	Ref.
H ₂ /O ₂ chain reactions					
1	$\dot{\text{H}} + \text{O}_2 = \dot{\text{O}} + \dot{\text{O}}\text{H}$	1.91×10^{14}	0.00	16.44	[39]
2	$\dot{\text{O}} + \text{H}_2 = \dot{\text{H}} + \dot{\text{O}}\text{H}$	5.08×10^4	2.67	6.292	[40]
3	$\dot{\text{O}}\text{H} + \text{H}_2 = \dot{\text{H}} + \text{H}_2\text{O}$	2.16×10^8	1.51	3.43	[41]
4	$\dot{\text{O}} + \text{H}_2\text{O} = \dot{\text{O}}\text{H} + \dot{\text{O}}\text{H}$	2.97×10^6	2.02	13.4	[42]
H ₂ /O ₂ dissociation/recombination reactions					
5 ^a	$\text{H}_2 + \text{M} = \dot{\text{H}} + \dot{\text{H}} + \text{M}$	4.57×10^{19}	-1.40	105.1	[43]
6 ^b	$\dot{\text{O}} + \dot{\text{O}} + \text{M} = \text{O}_2 + \text{M}$	6.17×10^{15}	-0.50	0.00	[43]
7 ^c	$\dot{\text{O}} + \dot{\text{H}} + \text{M} = \text{OH} + \text{M}$	4.72×10^{18}	-1.00	0.00	[43]
8 ^{d,e}	$\dot{\text{H}} + \dot{\text{O}}\text{H} + \text{M} = \text{H}_2\text{O} + \text{M}$	4.50×10^{22}	-2.00	0.00	[43] × 2.0
Formation and consumption of HO ₂					
9 ^{f,g}	$\dot{\text{H}} + \text{O}_2 + \text{M} = \text{HO}_2 + \text{M}$	3.48×10^{16}	-0.41	-1.12	[44]
	$\dot{\text{H}} + \text{O}_2 = \text{HO}_2$	1.48×10^{12}	0.60	0.00	[45]
10	$\text{HO}_2 + \dot{\text{H}} = \text{H}_2 + \text{O}_2$	1.66×10^{13}	0.00	0.82	[6]
11	$\text{HO}_2 + \dot{\text{H}} = \dot{\text{O}}\text{H} + \dot{\text{O}}\text{H}$	7.08×10^{13}	0.00	0.30	[6]
12	$\text{HO}_2 + \dot{\text{O}} = \dot{\text{O}}\text{H} + \text{O}_2$	3.25×10^{13}	0.00	0.00	[46]
13	$\text{HO}_2 + \dot{\text{O}}\text{H} = \text{H}_2\text{O} + \text{O}_2$	2.89×10^{13}	0.00	-0.50	[46]
Formation and consumption of H ₂ O ₂					
14 ^h	$\text{HO}_2 + \text{HO}_2 = \text{H}_2\text{O}_2 + \text{O}_2$	4.2×10^{14}	0.00	11.98	[47]
	$\text{HO}_2 + \text{HO}_2 = \text{H}_2\text{O}_2 + \text{O}_2$	1.3×10^{11}	0.00	-1.629	[47]
15 ^{i,f}	$\text{H}_2\text{O}_2 + \text{M} = \dot{\text{O}}\text{H} + \text{OH} + \text{M}$	1.27×10^{17}	0.00	45.5	[48]
	$\text{H}_2\text{O}_2 = \dot{\text{O}}\text{H} + \text{OH}$	2.95×10^{14}	0.00	48.4	[49]
16	$\text{H}_2\text{O}_2 + \dot{\text{H}} = \text{H}_2\text{O} + \dot{\text{O}}\text{H}$	2.41×10^{13}	0.00	3.97	[43]
17	$\text{H}_2\text{O}_2 + \dot{\text{H}} = \text{H}_2 + \text{HO}_2$	6.03×10^{13}	0.00	7.95	[43] × 1.25
18	$\text{H}_2\text{O}_2 + \dot{\text{O}} = \dot{\text{O}}\text{H} + \text{HO}_2$	9.55×10^6	2.00	3.97	[43]
19 ^h	$\text{H}_2\text{O}_2 + \dot{\text{O}}\text{H} = \text{H}_2\text{O} + \text{HO}_2$	1.0×10^{12}	0.00	0.00	[50]
	$\text{H}_2\text{O}_2 + \dot{\text{O}}\text{H} = \text{H}_2\text{O} + \text{HO}_2$	5.8×10^{14}	0.00	9.56	[50]

^a Efficiency factors are H₂O = 12.0; H₂ = 2.5.

^b Efficiency factors are H₂O = 12; H₂ = 2.5; Ar = 0.83; He = 0.83.

^c Efficiency factors are H₂O = 12; H₂ = 2.5; Ar = 0.75; He = 0.75.

^d Original pre-exponential A factor is multiplied by 2 here.

^e Efficiency factors are H₂O = 12; H₂ = 0.73; Ar = 0.38; He = 0.38.

^f Troe parameters: reaction 9, $a = 0.5$, $T^{***} = 1.0 \times 10^{-30}$, $T^* = 1.0 \times 10^{+30}$, $T^{**} = 1.0 \times 10^{+100}$; reaction 15, $a = 0.5$, $T^{***} = 1.0 \times 10^{-30}$, $T^* = 1.0 \times 10^{+30}$.

^g Efficiency factors are H₂ = 1.3; H₂O = 14; Ar = 0.67; He = 0.67.

^h Reactions 14 and 19 are expressed as the sum of the two rate expressions.

ⁱ Efficiency factors are H₂O = 12; H₂ = 2.5; Ar = 0.45; He = 0.45;

Figure A-0-1. The comprehensive H₂ combustion mechanism of Ó Conaire[60].

A.3 Definition of instantaneous properties in RSBI study

Table A-0-2. Definition of instantaneous properties in RSBI study

Properties	Comments	Definition
$T_{max,global}$	Global maximum temperature	$\max(T)$ for all cells
$P_{max,global}$	Global maximum pressure	$\max(P)$ for all cells
$T_{max,bubble}$	Maximum temperature inside the bubble	$\max(T)$ for cells with $Y_{Xe} > 0.1$
$P_{max,bubble}$	Maximum pressure inside the bubble	$\max(P)$ for cells with $Y_{Xe} > 0.1$
$V_{bubble}(t)$	Bubble volume	$\sum_k dV_k(t), \text{ if } Y_{Xe} > 0.1$
$V_{flame}(t)$	Flame volume	$\sum_k dV_k(t),$ $\text{if } Y_{H_2O,k} > 0.1 \cdot Y_{H_2O,max}(t)$
$m_i(t)$	Instant mass of i_{th} species	$\sum_k \rho_{i,k}(t) \cdot dV_k(t)$
$\hat{m}_i(t)$	Normalized mass of i_{th} species	$m_i(t)/m_{H_2}(0)$
$dm_i(t)/dt$	Mass generation rate	$\frac{m_i(t + \delta t) - m_i(t)}{\delta t}$
$n_i(t)$	Instant molar number of i_{th} species	$\sum_k \frac{\rho_{i,k}(t)}{MW_i} \cdot dV_k(t)$
$\hat{n}_i(t)$	Normalized molar number of i_{th} species	$n_i/n_{H_2}(0)$
$h_r(t)$	Chemical heat release	$-(h_f(t) - h_{o,f})$
$dh_r(t)/dt$	Chemical heat rate	$\frac{h_r(t + \delta t) - h_r(t)}{\delta t}$
$h_{full}(t)$	The combustion heat when H_2/O_2 are fully consumed and the only product is water vapor	$-(h_{f,H_2O}(vapor) - h_{o,f})$

A.4 The incorrect experimental data referred in Ref.[112]

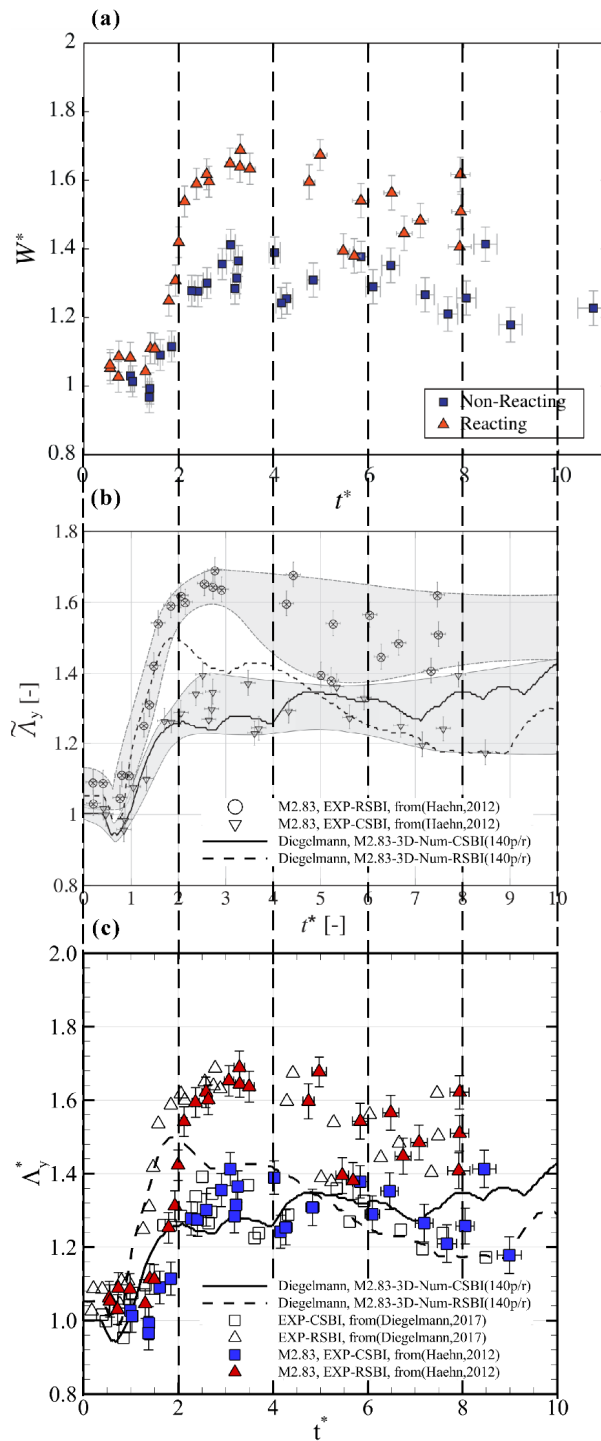


Figure A-0-2. The comparison of the $M = 2.83$ RSBI experimental data in two literatures. (a) the Fig.10(b) of Haehn et al.'s experimental work[88], (b) the Fig.18 of Diegelmann et al.'s numerical work[112], (c) plot of the data digitized from (a) and (b) in the same coordinates for comparison. Vertical dashed lines with the same t^* values across these three subfigures are drawn for reference.

When studying the high-Mach limiting case ($M = 2.83$) in the RSBI study, I find the experimental data of $M = 2.83$ case in Haehn et al.'s experiment[88] is incorrectly referred to by Diegelmann et al.'s numerical work [112]. Figure A-0-2 presents the data of $M = 2.83$ RSBI in these two works in subfigure (a) and (b) and plots them in the same coordinates for comparison in subfigure (c). The abscissas of these three subfigures are horizontally aligned for better comparison. The subfigure (c) clearly shows the differences between the two sets of experimental data: for both inert and reactive results, the data with hollow markers from Ref.[112] lie left to the data with solid markers in Ref.[88]. According to Haehn et al.'s experiment[88], the TBD value of $M = 2.83$ RSBI steeply rises at $t^* = 2$, while in Ref.[112], the moment of this steep increase occurs at around $t^* = 1.5$. Besides, the peak TBD value is found at $t^* = 3.25$ in Ref.[4], but is found at $t^* = 2.75$ in Ref.[4].